UNIVERSITY OF CALIFORNIA
RIVERSIDE

# Physical Properties of Galaxies at Small and Large Scales

A Dissertation submitted in partial satisfaction
of the requirements for the degree of

Doctor of Philosophy

in

Physics

by

Zahra Sattari

June 2024

Dissertation Committee:

Dr. Bahram Mobasher, Chairperson
Dr. Daniel D. Kelson
Dr. Brian D. Siana

The Dissertation of Zahra Sattari is approved:

---

---

---

Committee Chairperson

University of California, Riverside

## Acknowledgments

I would like to extend my sincere thanks to everyone who has helped me throughout my PhD journey and made this possible.

First and foremost, I am profoundly grateful to my Ph.D. advisor at UCR, Professor Bahram Mobasher. His exceptional guidance and support have been pivotal in shaping my research and academic growth. The insights he has provided me have been invaluable to my development as a researcher. I am also thankful to my co-advisor at Carnegie Observatories, Dr. Daniel Kelson, whose mentorship has been instrumental in the completion of this thesis. His constructive feedback, encouragement, and patience have been essential in overcoming the numerous challenges faced during my research.

I would like to extend my sincere appreciation to the department's faculty and members, whose collective support has greatly enriched my academic experience. In particular, I am deeply thankful to Dr. Brian Siana, who graciously agreed to serve on my committee and read my thesis.

I would like to express my deepest gratitude to my parents. Their unwavering support, encouragement, and belief in me have been the foundation of my academic and personal success. I am forever grateful for their guidance. I also extend my heartfelt thanks to my brother and sister, whose love and understanding have been invaluable throughout this journey. Special mention goes to my niece and nephew, Deniz and Araz, who have brought immense joy and inspiration into my life.

To Dr. Nima Chartab, I owe a debt of gratitude for his unwavering support, understanding, and encouragement throughout this journey. His love and belief in me have been a

cornerstone of my perseverance, especially during the most challenging times. His companionship has made this journey more enjoyable and less arduous, and I am deeply appreciative of his presence in my life.

My heartfelt thanks go to my incredible friends and groupmates at UCR: Drs. Nima Chartab, Abtin Shahidi, Hooshang Nayyeri, Shoubaneh Hemmati, Behnam Darvish, and Ali Ahmad Khostovan. Their friendship, collaboration, and intellectual exchange have been a source of motivation and inspiration. I cherish the memories of our shared experiences. I am also deeply appreciative of my friends and colleagues at Carnegie: Drs. Shannon Patel and Allison Matthews. Collaborating with them has been an absolute pleasure.

I am grateful to the CANDELS, UVCANDELS, and COSMOS collaborations for the opportunity to collaborate and contribute to their groundbreaking work. The experiences and knowledge gained through these teams have been invaluable to my research, providing me with insights and perspectives that have enriched my understanding of Astronomy.

Finally, I would like to acknowledge my best friends, Zeynab Madayen and Elham Zargaripour. Their unconditional friendship has been a source of motivation over the years.

There are too many other names that I could not list here, but I am deeply thankful to everyone who has supported me along the way. Your contributions have made a significant impact on my path, and I am forever grateful.

The text of this dissertation, in part, is a reprint of the material as it appears in journal articles entitled *Evidence for gas-phase metal deficiency in massive protocluster galaxies at* $z \sim 2.2$ (2021ApJ...910....57S), and *Fraction of Clumpy Star-forming Galaxies at* $0.5 \leq z \leq 3$ *in UVCANDELS: Dependence on Stellar Mass and Environment* (2023ApJ...951..147S).

To my parents for all the support.

ABSTRACT OF THE DISSERTATION

Physical Properties of Galaxies at Small and Large Scales

by

Zahra Sattari

Doctor of Philosophy, Graduate Program in Physics

University of California, Riverside, June 2024

Dr. Bahram Mobasher, Chairperson

This thesis presents a comprehensive analysis of galaxies spanning a wide range in mass and environment, using deep optical/infrared spectroscopy and high-resolution imaging to understand the physical mechanisms deriving their formation and evolution. The research is structured around three primary studies. 1) I studied the metal enrichment of galaxies in protoclusters and the effect of the environment on the mass-metallicity relation (MZR). I found that massive galaxies residing in protoclusters are metal-deficient compared to galaxies in the field. This implies that primordial cold gas, channeled through cosmic filaments, dilutes the metal con-

tent of the protocluster; 2) I investigated the fraction of clumpy galaxies at $0.5 < z < 3$, using UVCANDELS and CANDELS imaging data to examine clump properties in star-forming galaxies. The results reveal a peak in clumpiness around cosmic noon, with a decline towards the present and a lack of environmental dependence, suggesting that internal processes predominantly drive clump formation; 3) I extended the analyses to dwarf galaxies at $z \sim 0.15$, establishing a robust mass-metallicity relation and confirming the fundamental metallicity relation at low masses, highlighting the nuanced interplay between star formation rate and gas-phase metallicity. I find that the intrinsic scatter in the MZR is larger for dwarf galaxies compared to normal galaxies, indicating more diverse star formation histories and/or stronger environmental effects in these systems. This work advances our understanding of galaxy evolution across cosmic time, offering new insights into the mechanisms influencing star formation and chemical enrichment and finding the complex interplay between internal dynamics and environmental factors in shaping galaxy evolution.

# Contents

# List of Figures

# List of Tables

# Chapter 1

# Introduction

Galaxies, as fundamental building blocks of the universe, undergo a myriad of complex processes that govern their formation and evolution over cosmic time. Various internal and external activities influence these processes, including star formation, gas inflow from the circumgalactic and intergalactic media (CGM/IGM), and gas outflow to the interstellar medium (ISM) due to feedback mechanisms such as stellar winds, active galactic nuclei (AGNs), and supernova explosions (White and Frenk, 1991; Dekel and Birnboim, 2006; Somerville and Davé, 2015). Together, these interactions contribute to the "baryon cycle" within galaxies, shaping their properties and evolution (Lilly et al., 2013; Tumlinson et al., 2017).

Moreover, galaxies often reside within larger structures known as groups/clusters/protoclusters. The environmental context, whether a galaxy is part of a dense group/cluster or an isolated field, significantly impacts its evolutionary trajectory (e.g., Dressler, 1980; Mulchaey and Zabludoff, 1998; Peng et al., 2010).

## 1.1 Environmental Impact on Metal Enrichment

The environment in which a galaxy resides plays a crucial role in its evolution. Galaxies in dense environments, such as clusters and protoclusters, experience different evolutionary paths compared to those in the field. Environmental processes like ram pressure stripping, galaxy harassment, and tidal interactions are postulated to significantly influence the gas content, star formation rates, and morphology of galaxies (Gunn and Gott, 1972; Moore et al., 1996; Boselli and Gavazzi, 2006). For example, ram pressure stripping, caused by the interaction between a galaxy's interstellar medium (ISM) and the intracluster medium (ICM), can remove gas from galaxies, leading to a cessation of star formation (Gunn and Gott, 1972; Abadi et al., 1999). Galaxy harassment involves frequent high-speed encounters between galaxies in a cluster, which can induce morphological transformations and trigger bursts of star formation or, conversely, quench star formation by heating the ISM and driving gas outflows (Moore et al., 1996; Boselli and Gavazzi, 2006).

Observational studies have consistently shown that galaxies in dense environments in the local universe tend to be more quiescent and exhibit higher fractions of early-type morphologies compared to their counterparts in the field (Dressler, 1980; Peng et al., 2010; Woo et al., 2013). Such environmental dependence is also found beyond the local universe out to $z \sim 3$ (Quadri et al., 2007; Patel et al., 2009a,b, 2011; Quadri et al., 2012; Balogh et al., 2016; Darvish et al., 2016; Kawinwanichakij et al., 2017; Fossati et al., 2017; Nantais et al., 2017; Ji et al., 2018; Pintos-Castro et al., 2019; Chartab et al., 2020; Ando et al., 2020; Old et al., 2020). However, at high redshifts beyond $z > 2$, the relationship between environment and galaxy evolution becomes more complex and less clear.

Some studies suggest that galaxies in overdensities at $z \sim 2-3$ have lower star formation rates (SFRs), following the same trend as the local universe (e.g., Patel et al., 2009a,b, 2011; Kawinwanichakij et al., 2017; Chartab et al., 2020). Conversely, other studies find that protoclusters at similar redshifts exhibit elevated SFRs, indicating a reversal of the local trend where dense environments quench star formation (e.g., Elbaz et al., 2007; Cooper et al., 2008; Lemaux et al., 2022). Additionally, some studies show no significant difference in SFRs between galaxies in dense environments and those in the field, suggesting no strong environmental effect (e.g., Darvish et al., 2016). Together, these indicate that the influence of the environment on galaxy evolution at high redshifts is still an open question and may depend on various factors such as the specific properties of the protocluster, the stage of its evolution, and the selection criteria of the galaxies studied (Overzier, 2016).

Beyond star formation rate, gas-phase metallicity is another crucial measurement for understanding galaxy evolution. Metallicity, the abundance of elements heavier than hydrogen and helium, is influenced by star formation and feedback processes such as supernovae and stellar winds (Garnett, 2002; Brooks et al., 2007; Steidel et al., 2010; Martin et al., 2012; Chisholm et al., 2018). These processes can enrich the ISM and affect the metal content of outflows into the IGM (Heckman et al., 1990; Tremonti et al., 2004). A significant correlation has been observed between gas-phase metallicity and stellar mass, known as the Mass-Metallicity Relation (MZR), which holds up to $z \sim 3.5$ (Lequeux et al., 1979; Tremonti et al., 2004; Erb et al., 2006; Mannucci et al., 2009; Finkelstein et al., 2011; Steidel et al., 2014; Sanders et al., 2015, 2020). This relation appears to evolve substantially with redshift, such that galaxies at a given stellar mass have lower metallicities at higher redshifts (Maiolino and Mannucci, 2019).

Star formation rates also appear to be correlated with metallicity. At a given stellar mass, galaxies with lower SFRs tend to have higher metallicities (Mannucci et al., 2010; Sanders et al., 2018). Gas accretion from the IGM introduces chemically poor gas into the ISM, which can lower gas-phase metallicity while also providing additional fuel for star formation (Lilly et al., 2013).

Studies have also shown varying degrees of environmental impact on metallicity. In the local universe, studies have shown that at a given stellar mass, galaxies in overdensities exhibit higher gas-phase metallicity compared to field galaxies (Cooper et al., 2008; Peng and Maiolino, 2014). The accretion of metal-laden gas from recycling due to the outflows can cause this increase in the metal content of the galaxies in overdensities. However, at higher redshifts, the situation is less clear. Some studies report higher metallicities in protocluster galaxies at $z > 2$ (Kulas et al., 2013; Shimakawa et al., 2015), while others find lower (Valentino et al., 2015; Chartab et al., 2021) or no significant difference compared to field galaxies (Kacprzak et al., 2015).

Therefore, understanding the interplay between metallicity, star formation, and environment is crucial for constructing a comprehensive picture of galaxy evolution. Chapter 2 of this thesis investigates these environmental impacts by analyzing the gas-phase metallicities of galaxies within a protocluster at $z = 2.2$ in the COSMOS field, providing insights into how external processes shape galaxy evolution in the key epoch of cosmic noon.

## 1.2 Star-forming Clumps in High-Redshift Galaxies

High-resolution imaging of galaxies in the rest-frame UV has revealed the presence of giant star-forming clumps, particularly in high redshift galaxies. These clumps, which are typically a few hundred parsecs in size, are critical for understanding galaxy formation and evolution as they represent intense regions of star formation. The formation and evolution of clumps provide important information about the internal processes within galaxies and the interaction between galaxies and their environments.

Clumps are believed to form through gravitational instabilities within gas-rich disks and can migrate towards the galactic center, potentially contributing to bulge formation and the growth of supermassive black holes (Dekel et al., 2009b; Bournaud et al., 2014). The migration and eventual coalescence of these sub-structures can lead to the formation of central bulges in galaxies, influencing their overall morphology. Studies have shown that the fraction of clumpy galaxies increases with redshift, peaking around $z \sim 1.5$, which suggests that clump formation was more prevalent in the early universe (Guo et al., 2015; Shibuya et al., 2016). This trend aligns with the observation that galaxies at higher redshifts have higher gas fractions and more turbulent disks, conditions that favor clump formation (Wisnioski et al., 2015).

Previous studies have utilized data from the Hubble Space Telescope (HST) to identify and analyze clumps in star-forming galaxies. For example, Guo et al. (2015) used HST imaging to study the fraction of clumpy galaxies in The Cosmic Assembly Near-IR Deep Extragalactic Legacy Survey (CANDELS; Grogin et al., 2011; Koekemoer et al., 2011) fields and found that the fraction of clumpy galaxies is higher in lower mass galaxies and increases with redshift. Additionally, Shibuya et al. (2016) analyzed a large sample of galaxies from various HST surveys

and confirmed that clumpy galaxies are more common at higher redshifts. These studies provide valuable insights into the processes driving clump formation and their role in galaxy evolution.

Recently, UVCANDELS (Ultraviolet Imaging of the Cosmic Assembly Near-infrared Deep Extragalactic Legacy Survey) has provided unique imaging data covering the far UV for galaxies in a wide redshift range of $z = 0.5 - 2$, enabling a comprehensive analysis of clumpy star-forming regions across a broad span of cosmic time. Chapter 3 of this thesis leverages these datasets, combined with CANDELS, to study clumps across $z \sim 0.5 - 3$, enhancing our understanding of their role in galaxy evolution and their connection with the galaxy environment.

The environment in which these clumpy galaxies reside can also play a role in the formation and evolution of clumps. In dense environments such as clusters and protoclusters, interactions such as mergers and tidal forces can trigger clump formation and influence their subsequent migration and coalescence. Conversely, in less dense field environments, the formation and survival of clumps can be more influenced by internal processes such as disk instabilities and supernova feedback. Therefore, studying the properties of star-forming clumps across different environments can help constrain the mechanisms that drive the formation of clumps. By tracking the dependence of clump formation—and its associated star formation activity—on environment and time, we can test the extent to which the accelerating rise of the large-scale structure itself plays a role in shaping the cosmic star formation rate density (Madau and Dickinson, 2014) at late times or in the evolving variations of galaxy SFR, morphology, and metallicity across time and environment.

With the James Webb Space Telescope (JWST) now operational, this field is set to be revolutionized by its high-resolution imaging and spectroscopy capabilities in the infrared.

Data from JWST will allow for detailed spectral energy distribution (SED) fitting of clumps, offering insights into their stellar populations, star formation histories, and dust content. In the future, such data will enable a more comprehensive understanding of the physical properties of star-forming clumps and their impact on galaxy formation and evolution.

## 1.3 Dwarf Galaxies

Dwarf galaxies, with their low masses ($M_* < 10^9\ M_\odot$), offer unique insights into the processes of galaxy formation and evolution. They are the most numerous type of galaxy and play a vital role in the hierarchical framework of structure formation. Today's larger galaxies have their origins in these low-mass structures from the early universe. Thus, accurately modeling dwarf galaxies in galaxy formation theory is essential. Without a robust understanding and representation of these galaxies at later stages, confidence in the theoretical modeling of earlier galaxy formation remains uncertain.

It is widely believed that dwarf galaxies were pivotal contributors to the ionizing photon budget during the reionization era and also play a significant role in the metal enrichment of the circum-/intergalactic medium (CGM/IGM) (e.g., Robertson et al., 2010; Lin et al., 2023). While dwarf galaxies might be intuitively simpler to study, being predominantly in-situ hubs of star formation and having minimal merger contributions, the current simulation models have struggled to capture the vast diversity observed in their properties – a challenge often referred to as the "dwarf diversity problem" (Sales et al., 2022). There has been an increased focus on the observational study of dwarf galaxies in recent years. However, the primary obstacle has been the scarcity of detailed photometric and spectroscopic data.

Due to their shallow gravitational wells, dwarf galaxies are highly susceptible to feedback processes, such as supernova explosions and stellar winds, which can expel gas and suppress star formation (Dekel and Silk, 1986; Silk, 2003). This makes them excellent laboratories for studying the effects of feedback on galaxy evolution. Additionally, dwarf galaxies provide valuable information about the metal enrichment history of galaxies. The mass-metallicity relation (MZR) for dwarf galaxies shows significant scatter, reflecting their sensitivity to environmental effects and internal processes (Berg et al., 2012; Jimmy et al., 2015). For example, Zahid et al. (2012) found that the scatter in the MZR increases at lower stellar masses, indicating that dwarf galaxies are more affected by stochastic events like bursts of star formation and supernova-driven winds. Additionally, Berg et al. (2012) used spectroscopic data to study the metallicities of a sample of local dwarf galaxies and found that these galaxies exhibit a wide range of metallicities, highlighting the diverse evolutionary paths of low-mass systems. Gallagher et al. (1984) show that galaxies at these masses tend to have rising Star formation histories (SFHs) at late times (see also Kelson, 2014; Kelson et al., 2020), having not yet exhausted their cosmic gas supply on average, unlike massive galaxies that have been studied with far more detail and attention.

Chapter 4 of this thesis is dedicated to the optical spectroscopy of dwarf galaxies at $z \sim 0.15$ in the COSMOS field. By examining a unique spectroscopic sample of more than 300 dwarf galaxies, this work provides detailed measurements of their physical properties, star formation rates, and gas-phase metallicities. We also compare these dwarf galaxies to a sample of $\sim 700$ galaxies at slightly higher masses, observed in a similar fashion, to better understand the subtle differences in galaxy properties with stellar mass. This study significantly enhances

our comprehension of the metal enrichment history in dwarf galaxies, shedding light on their pivotal contributions within the broader framework of galaxy evolution.

# Chapter 2

# Evidence for gas-phase metal deficiency in massive protocluster galaxies at $z \sim 2.2$


## Abstract

We study the mass-metallicity relation for 19 members of a spectroscopically-confirmed protocluster in the COSMOS field at $z = 2.2$ (CC2.2) and compare it with that of 24 similarly selected field galaxies at the same redshift. Both samples are H$\alpha$ emitting sources, chosen from the HiZELS narrow-band survey, with metallicities derived from N2 ($\frac{[\mathrm{NII}]\lambda 6584}{\mathrm{H}\alpha}$) line ratio. For the mass-matched samples of protocluster and field galaxies, we find that protocluster galaxies with $10^{9.9}\mathrm{M}_{\odot} \leq \mathrm{M}_{*} \leq 10^{10.9}\mathrm{M}_{\odot}$ are metal deficient by $0.10 \pm 0.04$ dex ($2.5\sigma$ significance) compared to their coeval field galaxies. This metal deficiency is absent for low mass galaxies, $\mathrm{M}_{*} < 10^{9.9}\mathrm{M}_{\odot}$. Moreover, relying on both SED-derived and H$\alpha$ (corrected for dust extinction

based on $M_*$) SFRs, we find no strong environmental dependence of SFR-$M_*$ relation, however, we are not able to rule out the existence of small dependence due to inherent uncertainties in both SFR estimators. The existence of $2.5\sigma$ significant metal deficiency for massive protocluster galaxies favors a model in which funneling of the primordial cold gas through filaments dilutes the metal content of protoclusters at high redshifts ($z \gtrsim 2$). At these redshifts, gas reservoirs in filaments are dense enough to cool down rapidly and fall into the potential well of the protocluster to lower the gas-phase metallicity of galaxies. Moreover, part of this metal deficiency could be originated from galaxy interactions which are more prevalent in dense environments.

## 2.1 Introduction

In the standard ΛCDM cosmological scenario, structures form from the growth of small fluctuations through gravitational instability. Dark matter structures grow by two main processes: By merging small halos to form the larger ones or by smooth accretion of dark matter from their immediate environment. Baryons fall into the potential well of these dark matter structures and feed galaxies within those structures with cold pristine gas, which allows them to form their stars. Galaxy clusters observed in the present Universe are the largest virialized dark matter halos that are populated with massive and evolved galaxies (e.g., Dressler, 1980; Balogh et al., 2004; Kauffmann et al., 2004; Peng et al., 2010). At high redshifts ($z \gtrsim 2$), most of these clusters have not yet had the time to virialize and consist of subhalos which will then merge and form the massive clusters present in the local Universe. Direct observations of the progenitors of these clusters at high redshifts, known as protoclusters, provide useful information about the processes involved in the early stages of structure formation.

It is now well established that, at a given redshift, the interstellar medium (ISM) of massive galaxies is more metal-enriched than that of low mass galaxies. This correlation, known as mass-metallicity relation (hereafter MZR), is observed out to $z \sim 3.5$ (see review by Maiolino and Mannucci, 2019, and references therein). The infall of cold gas from intergalactic medium (IGM) provides the fuel for galaxies to form their stars, which are the factories responsible for metal production in galaxies. However, galaxies are not very efficient in forming stars as the cold gas accretes into their potential well. Behroozi et al. (2013a) found that the star formation efficiency of galaxies (the star formation rate (SFR) divided by the baryon accretion rate) can reach a maximum of $\sim 55\%$. Therefore, the extra primordial cold gas that could not convert to stars dilutes the metal content of the ISM. This mechanism can explain observations where, at a given stellar mass, galaxies with higher SFR have lower gas-phase metallicity (e.g., Mannucci et al., 2010; Lara-López et al., 2010a; Stott et al., 2013; Sanders et al., 2018). More interestingly, many studies suggest that these two parameters, SFR and gas accretion rate, depend on the environment of galaxies even at high redshift Universe (Darvish et al., 2016; Kawinwanichakij et al., 2017; Chartab et al., 2020). Thus, comparing gas-phase metallicity of galaxies in extreme environments and high redshifts, such as protoclusters, with a similarly selected population of field galaxies at the same redshift can provide valuable insights about galaxy evolution processes and their environmental dependencies.

Although in the local Universe, most of the studies found evidence for environmental imprint on the MZR (e.g., Cooper et al., 2008; Ellison et al., 2009; Peng and Maiolino, 2014; Sobral et al., 2015), environmental dependence of the MZR at high redshift is still controversial. Some studies found an enhancement in the gas-phase metallicity of galaxies in protoclusters

compared to their field counterparts at $z \sim 2$ (Kulas et al., 2013; Shimakawa et al., 2015). However, there is observational evidence of metal deficiency in protocluster galaxies at $z \sim 2$ compared to their field counterparts, according to Valentino et al. (2015). Moreover, Chartab et al. (2021) studied the relation between the local density of MOSFIRE Deep Evolution Field (MOSDEF; Kriek et al., 2015) galaxies and their gas-phase metallicities and found that galaxies in overdensities have $\sim 0.07$ dex lower metallicity than the field galaxies at $z \sim 2.3$. On the other hand, Kacprzak et al. (2015) and Alcorn et al. (2019) found no significant environmental dependence on the MZR of galaxies at $z \sim 2$.

In this paper, we study the MZR for galaxy members of the recently confirmed protocluster, CC2.2, in the Cosmic Evolution Survey (COSMOS; Scoville et al., 2007) at $z \sim 2.2$ (Darvish et al., 2020). We then compare this relation with a control sample of similarly selected field galaxies. Both protocluster and field samples are H$\alpha$ emitting sources, selected from the narrow-band High-Z Emission Line Survey (HiZELS; Geach et al., 2012; Sobral et al., 2013, 2014). The paper is organized as follows: In Section 2.2, we describe the KeckI/MOSFIRE observations and data reduction procedure followed by stellar mass measurements and sample selection. We then explain the stacking process and measurements of gas-phase metallicities in Section 2.3. In Section 2.4, we construct the MZR for both protocluster and field samples and compare them to deduce the role of the environment in MZR at $z \sim 2.2$. We discuss our results in Section 2.5.

Throughout this paper, we assume a flat $\Lambda$CDM cosmology with $H_0 = 70\,\mathrm{kms^{-1}Mpc^{-1}}$, $\Omega_{m_0} = 0.3$ and $\Omega_{\Lambda_0} = 0.7$. All the physical parameters are measured assuming a Chabrier (2003) initial mass function (IMF).

## 2.2 Data

### 2.2.1 MOSFIRE Observation

In this paper, we use near-IR spectroscopy of galaxies in a recently confirmed protocluster, CC2.2, at $z \sim 2.2$ (Darvish et al., 2020), in the COSMOS field (Scoville et al., 2007). The spectroscopic observations were conducted with KeckI/MOSFIRE NIR multi-object spectrograph (McLean et al., 2012) in December 2018 and January 2019 in both $K(\sim 1.92-2.40\mu m)$ and $H(\sim 1.47-1.81\mu m)$ bands, leading to 35 confirmed members. The primary spectroscopic sample comprises the narrow-band H$\alpha$ emitting candidates from the HiZELS survey (Geach et al., 2012; Sobral et al., 2013, 2014). For a full description of the protocluster identification and observation, we refer readers to Darvish et al. (2020).

As a control sample, we use KeckI/MOSFIRE spectroscopic observations of 24 field galaxies in the redshift range $2.22 \leq z \leq 2.24$, located in less-crowded regions of the COSMOS (16 galaxies) and UDS (8 galaxies) fields. All these field galaxies were observed over the observing programs during 2018-2019 (PI: N. Z. Scoville) in $K$ band (a few in $H$ band as well) and are selected similarly from the HiZELS survey to avoid any biases introduced by sample selection.

The observations were performed the same way for both field and protocluster galaxies, minimizing any source of bias. All the observing nights were conducted under clear conditions with the average seeing of $0.5''$, and a typical exposure time of $\sim 90$ minutes per mask.

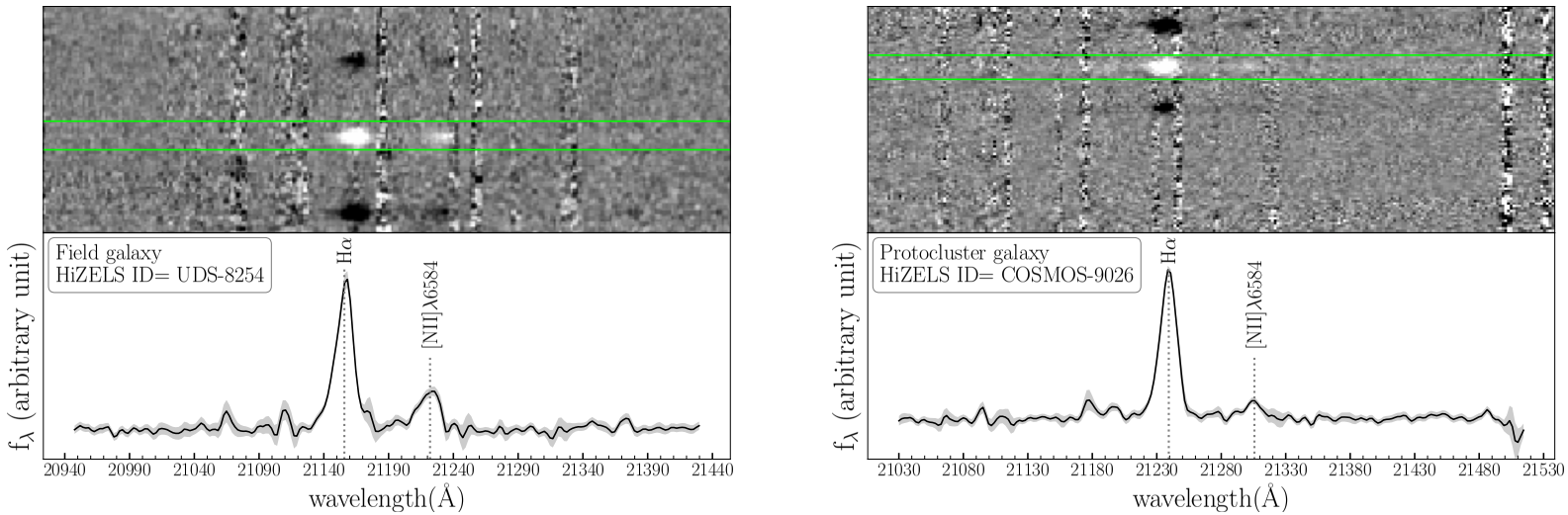


Figure 2.1: The 2D and corresponding optimally extracted 1D spectra for two galaxies selected from our sample. *Left*: Example of a field galaxy. This galaxy is at $z = 2.223$ and has a stellar mass $10^{10.05}\mathrm{M}_{\odot}$. *Right*: A galaxy member of the protocluster at $z = 2.235$. The stellar mass of this galaxy is $10^{9.96}\mathrm{M}_{\odot}$. In both spectra, H$\alpha$ and [NII]$\lambda$6584 emission lines are evident.

### 2.2.2 Data Reduction

The acquired data were reduced using the MOSFIRE data reduction pipeline (DRP). The outputs of the DRP are rectified, sky-subtracted, and wavelength-calibrated 2D spectra and their associated uncertainties. We then extract optimally weighted 1D spectra and their errors using the optimal extraction algorithm (Horne, 1986). We weight the flux of each pixel by the inverse of the flux variance and the spatial extent of the 2D spectrum in an optimized window and then, sum the weighted fluxes along the wavelength axis. The size of the optimized window is determined such that the bright features with the highest signal-to-noise (S/N) in the 2D spectrum are surrounded by the window. The weighted summation within the optimized window produces 1D spectra of the sources along with their errors. Figure 2.1 shows an example of the 2D and optimally extracted 1D spectra for a field galaxy and a protocluster member.

We fit a triple Gaussian function to the reduced 1D spectra to extract [NII]$\lambda$6548, H$\alpha$ and [NII]$\lambda$6584 emission line fluxes. We require a constant value for the continuum and the same width for all three emission lines. The line fluxes are the integration of the best fit Gaussian function to the 1D spectra. For the error calculation, we perturb the 1D spectra 1000 times and remeasure the line fluxes. The standard deviation of these 1000 measurements is assigned as the uncertainty in line fluxes. The redshifts of the sources are measured based on the peak of H$\alpha$ emission lines with S/N $\geq$ 3.

### 2.2.3 Stellar Masses and SFRs

We estimate the stellar masses ($M_*$) and SFRs of galaxies by fitting synthetic spectral energy distributions (SED) to their available photometric data (COSMOS: Laigle et al. (2016);

UDS: Mehta et al. (2018)). To perform the SED fitting, we utilize Bayesian Analysis of Galaxies for Physical Inference and Parameter EStimation (Bagpipes) code (Carnall et al., 2018), which uses 2016 version of a library of Bruzual and Charlot (2003) synthetic spectra. We fix the redshifts of galaxies to their spectroscopic values, considering delayed exponentially declining star formation history, $te^{-t/\tau}$. A range of $0.3-10$ Gyr with a uniform prior is assumed for the star formation e-folding time-scale ($\tau$). The nebular emission models which are constructed based on the methodology of Byler et al. (2017) are added to the SEDs. Also a metallicity range $0 < Z/Z_{\odot} < 2.5$ with a logarithmic prior and a Calzetti et al. (2000) extinction law are adopted.

The SFRs of the galaxies are also estimated using their H$\alpha$ emission line fluxes taken from HiZELS survey (Sobral et al., 2013). Since the $H$ band data are not available for most of the sample, following Sobral et al. (2012) and Koyama et al. (2013), we utilize Garn and Best (2010) calibration to correct the H$\alpha$ luminosity for the dust extinction based on the stellar masses of the galaxies. We then convert the dust-corrected H$\alpha$ luminosity to SFR using the calibration from Kennicutt (1998): $SFR(M_{\odot}yr^{-1}) = 7.9 \times 10^{-42} L_{H\alpha}(erg/s)$. One should note that the SFR derived from this method is highly uncertain due to the existence of a large scatter in dust attenuation calibration based on the stellar mass.

### 2.2.4 Sample Selection

We select galaxies with significant detection in H$\alpha$ emission lines (S/N$\geq$ 3). We exclude galaxies with $M_{*} < 10^{9.5} M_{\odot}$ to construct a mass complete sample. We also remove potential mergers by visual inspection of their spectra and images, as well as the active galactic nuclei (AGNs). The AGNs are identified through their broad emission lines, X-ray flags included in the UDS and COSMOS catalogs, or IR emissions (Donley et al., 2012). Moreover, optical AGNs

are excluded by requiring $\log(\frac{[\mathrm{NII}]\lambda6584}{\mathrm{H}\alpha}) < -0.3$ (Coil et al., 2015). These criteria result in 19 protocluster members at $z = 2.23$ and 24 field galaxies at the same redshift, spanning a narrow redshift range $2.22 \leq z \leq 2.24$.

## 2.3 Composite spectra

### 2.3.1 Stacking Analysis

We measure the gas-phase metallicity of galaxies, using the N2 ($\frac{[\mathrm{NII}]\lambda6584}{\mathrm{H}\alpha}$) line ratio. Due to the prevalence of [NII]$\lambda$6584 undetected galaxies in our low-mass sample (S/N $< 3$), we use stacking technique. To stack the spectra, we divide the sample into three stellar mass bins, with an equal number of objects in each bin, for both the protocluster and field galaxies. We provide the range of stellar mass bins and the number of galaxies residing in each bin for the field and protocluster samples in Table 2.1. We then shift the spectra of galaxies to their rest-frame and normalize them by the total H$\alpha$ luminosity. In each mass-bin, we bin the normalized spectrum with a resolution of 0.5 Å. The stacked spectrum is calculated as the weighted average of the spectra in each 0.5 Å bin:

$$\tilde{f}(\lambda)^{\mathrm{stacked}} = \frac{\sum_i \frac{\tilde{f}_i(\lambda)}{{\sigma_i}^2}}{\sum_i \frac{1}{{\sigma_i}^2}}, \tag{2.1}$$

where $\tilde{f}_i(\lambda)$ is the flux density of each normalized spectrum, $\sigma_i$ is its corresponding standard deviation, and $\tilde{f}(\lambda)^{\mathrm{stacked}}$ is the composite spectrum with the uncertainty of $\sqrt{1/(\sum_i \frac{1}{{\sigma_i}^2})}$ in each mass-bin. The protocluster and field galaxies are also bootstrap resampled 100 times to

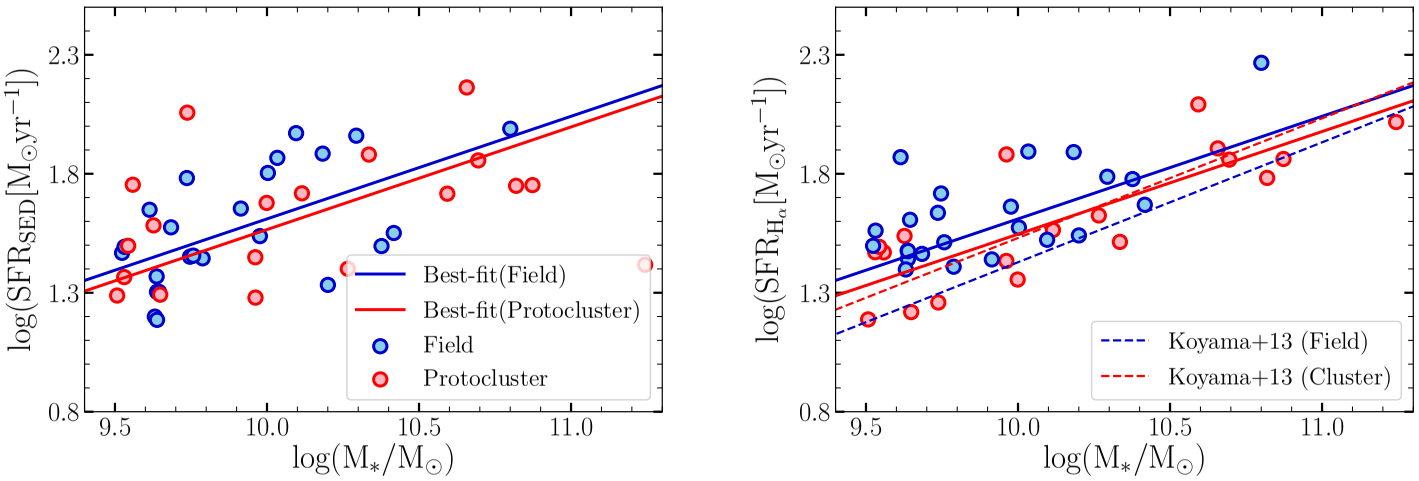


Figure 2.2: SFR of the field (blue circles) and protocluster (red circles) galaxies as a function of their stellar masses. *Left*: The SFRs are calculated from SED fitting. *Right*: The SFRs are determined using the H$\alpha$ luminosity of galaxies corrected for the dust extinction based on their stellar masses. The solid lines in each panel show the best-fit to the data points. The slope of the protocluster best-fit line (solid red lines) is fixed at the slope of the best-fit line for field galaxies (solid blue lines). The dashed blue (red) line shows the best-fit for the field (cluster) galaxies from Koyama et al. (2013).

take into account the sample variance. To perform the bootstrap resampling, we draw a random sample of galaxies from the original sample considering replacement. The replacement allows us to have a random sample that may include some duplicate members from the original sample, or may not contain some of the galaxies from the initial sample. This process is repeated 100 times and each time we end up having new stacked spectra. The sample variance is calculated using the standard deviation of these 100 trials.

Table 2.1: The stellar mass range of each mass bin in the stacking process

| Sample | $\log \frac{M_*}{M_\odot}$ | Number of galaxies |
|---|---|---|
| Field | [9.5,9.7) | 8 |
| | [9.7,10) | 8 |
| | [10,10.8] | 8 |
| Protocluster | [9.5,9.8) | 7 |
| | [9.8,10.5) | 6 |
| | [10.5,11.2] | 6 |

### 2.3.2 Metallicities

Since only a few field galaxies are observed in the $H$ band ($\sim$ 10% of the field galaxies), we utilize rest-frame optical emission line in the observed $K$ band to measure the gas-phase metallicities. This is done by measuring the best-fit [NII]$\lambda$6584 and H$\alpha$ emission line intensities and estimating the gas-phase metallicity using the N2 ($\frac{[\mathrm{NII}]\lambda6584}{\mathrm{H}\alpha}$) line ratio.

To measure the line fluxes and their uncertainties for the stacked spectra, we use the same methodology described in Section 2.2.2 for the individual spectra. Since the stacked spectra are normalized by the H$\alpha$ luminosity, the area underneath the [NII]$\lambda$6584 line in the stacked spectra corresponds to $\langle\frac{[\mathrm{NII}]\lambda6584}{\mathrm{H}\alpha}\rangle$.

In order to measure the gas-phase oxygen abundance ($12 + \log(O/H)$) of galaxies, we employ the empirical calibration from Pettini and Pagel (2004), which is based on electron temperature measurements in the local HII regions, and is given by $8.9 + 0.57 \log(N2)$.

## 2.4 Results

### 2.4.1 SFR-$M_*$ Relation

Different studies have shown that the fundamental metallicity relation (FMR) exists for galaxies at $z \sim 2$ (Mannucci et al., 2010; Sanders et al., 2018). According to this relation, at a given stellar mass, galaxies that have a higher SFR tend to have lower gas-phase metallicities. Thus, before studying the environmental dependence of the MZR in our sample, to investigate any possible dependence between the environment of the galaxies and their SFRs we show the relation between the SFR of the field and protocluster galaxies and their stellar masses in Figure 2.2. The SFR in the left panel is calculated from SED fitting, while the right panel shows the H$\alpha$ SFRs (corrected for extinction as mentioned in section 2.2.3) as a function of stellar mass.

An important issue in the SFR estimation using these two methods is that there are large uncertainties in both measurements. This will not allow us to rule out any small environmental dependence of the main sequence, if exists. For a better comparison, we also add the best-fit line from Koyama et al. (2013) in the right panel of Figure 2.2. Our result is in agreement with theirs, showing no significant environmental dependence of the main sequence galaxies for our star forming sample.

### 2.4.2 Mass-Metallicity Relation

In this section, we study the MZR for the field and protocluster samples to investigate the role of the environment in the gas-phase metallicity of galaxies at fixed $M_*$. As discussed in Section 2.3.1, we divide the sample into three stellar mass bins with equal number of galaxies in each bin. Figure 2.3 shows the MZR for the stacked spectra and individual galaxies. The metallicities of the stacked spectra in three stellar mass bins are shown in blue (red) squares for field (protocluster) galaxies. The stellar mass uncertainty in the stacked data points shows $1\sigma$ scatter in each bin.

As shown in Figure 2.3, in the stellar mass range $10^{9.7}M_\odot \lesssim M_* \lesssim 10^{10.5}M_\odot$, the average protocluster galaxies have a relatively lower metallicity than the average field galaxies by $\sim 0.1$ dex. However, the gas-phase metallicity of low-mass galaxies, $M_* < 10^{9.7}M_\odot$, do not significantly depend on the environment. Moreover, in the massive end of the MZR ($M_* > 10^{10.5}M_\odot$), due to the small number of field galaxies, we cannot draw robust conclusions on the MZR variation between the field and protocluster galaxies. In the following section, we match the stellar mass distributions of protocluster and field samples to properly isolate the effect of stellar mass from galaxy environment.

### 2.4.3 The Mass-Matched Samples

It is known that protoclusters often host more massive galaxies compared to the field. Therefore, to have a reliable comparison between the metallicity of protocluster and field galaxies at fixed stellar mass, the two samples should have similar stellar mass distributions. Otherwise, any change in the MZR may be attributed to the differences in stellar mass distributions.

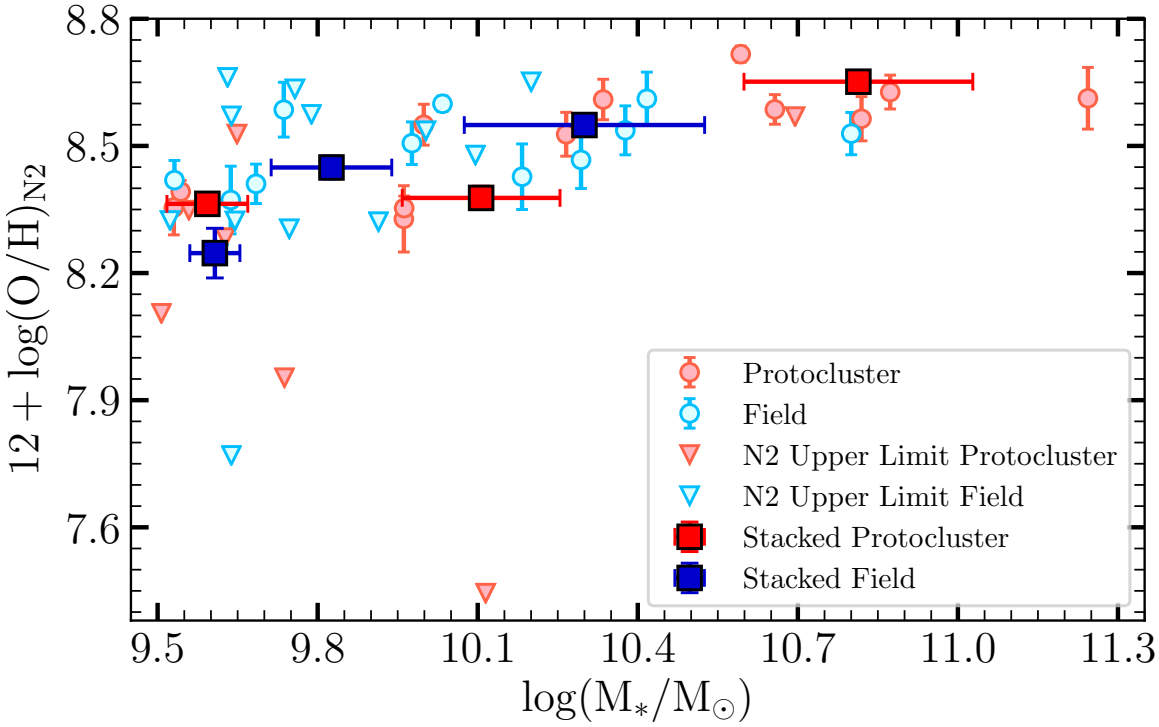


Figure 2.3: MZR for the field (blue circles) and protocluster (red circles) galaxies at $z \sim 2.2$, without controlling for the stellar mass distribution (mass-matching). The $1\sigma$ upper-limits for galaxies with undetected [NII]$\lambda$6584 line are shown with inverted triangles. The solid blue (red) squares indicate the metallicity measurements for stacked spectra of field (protocluster) galaxies in three bins of stellar mass. The error bars are smaller than the square symbols if not shown. Also, the horizontal error bars in the stacked data show the $1\sigma$ scatter in the stellar mass of each bin.

The left panel in Figure 2.4 shows the stellar mass distribution for the field and protocluster galaxies. It is clear that, for protocluster galaxies in the massive end of the distribution, there is no analog of the field galaxy, resulting in a biased comparison between field and protocluster samples. We resolve this by constructing the mass-matched samples. Similar to Chartab et al. (2021), we match the stellar mass distributions of field and protocluster galaxies with the resolution of $\log(M_*/M_\odot) = 0.1$ dex, which is the typical stellar mass uncertainties computed in section 2.2.3. As a result of mass-matched distributions, we have the same number of protocluster and field galaxies in each stellar mass bin of $\log(M_*/M_\odot) = 0.1$ (green hatched region in the left panel of Figure 2.4).

However, there is not a unique way to subsample data and construct mass-matched samples. For instance, four protocluster galaxies are in the mass range $10^{9.5}M_\odot \leq M_* \leq 10^{9.6}M_\odot$, but just two field galaxies are in this range of stellar mass. Thus, to take into account all the galaxies that reside in each mass-matched region, we randomly subsample galaxies 500 times and each time, we construct the stacked spectra and perturb them based on their uncertainties. The stacking process is the same as described in Section 2.3.1, where we consider both measurement errors and sample variance. The average and standard deviation of 500 trials correspond to the composite spectrum and its error, respectively. The right panels in Figure 2.4 show the composite spectra for the mass-matched sample of protocluster and the field galaxies in two stellar mass bins $10^{9.5}M_\odot \leq M_* < 10^{9.9}M_\odot$, and $10^{9.9}M_\odot \leq M_* \leq 10^{10.9}M_\odot$.

We report the gas-phase metallicities of the field and protocluster galaxies for the mass-matched samples in Table 2.2. Red (blue) squares in Figure 2.5 (top panel) show the MZR for the stacked protocluster (field) sample in two stellar mass bins $10^{9.5}M_\odot \leq M_* < 10^{9.9}M_\odot$, and

$10^{9.9}M_\odot \leq M_* \leq 10^{10.9}M_\odot$. The metallicity estimates for all the galaxies in the mass-matched samples are also included in the figure. At $z \sim 2.2$, the protocluster galaxies in the massive end of the MZR are metal deficient by $0.10 \pm 0.04$ ($2.5\sigma$ significance) dex compared to those residing in the field. However, this deficiency is not significant ($< 1\ \sigma$) in the lower mass bin ($0.03 \pm 0.06$ dex), possibly due to the prevalence of non-detections and/or small sample size.

Table 2.2: Gas-phase metallicities of the stacked spectra for the mass-matched samples. The second and third columns show stellar mass ranges and the mean value of mass in each range, respectively.

| Environment | $\log \frac{M_*}{M_\odot}$ | $\langle \log \frac{M_*}{M_\odot} \rangle$ | $\langle 12 + \log(O/H) \rangle$ |
|---|---|---|---|
| Field | [9.5,9.9) | $9.62 \pm 0.04$ | $8.38 \pm 0.04$ |
| | [9.9,10.9] | $10.25 \pm 0.12$ | $8.50 \pm 0.03$ |
| Protocluster | [9.5,9.9) | $9.62 \pm 0.03$ | $8.35 \pm 0.05$ |
| | [9.9,10.9] | $10.25 \pm 0.12$ | $8.40 \pm 0.03$ |

### 2.4.4 Comparison with Literature

To compare our results with those in the literature, we show the offset between the average gas-phase metallicity of the protocluster (galaxies in overdense regions) and the field galaxies from different studies (including the present work) as a function of stellar mass in Figure 2.5 (bottom panel).

We emphasize that gas-phase metallicity is calibrated locally and its absolute value at high redshift could be uncertain (Steidel et al., 2014; Shapley et al., 2019). However, when we study relative metallicity and estimate the difference of metallicities between field and protocluster galaxies, the calibration effect is not a concern.

Moreover, consideration of selection biases is essential in measuring the MZR (Stott et al., 2013). Different selection criteria for protocluster and field samples result in an unreliable

comparison between their respective metallicities. As both protocluster and field samples in the present work are H$\alpha$-selected, the metallicity offset does not suffer from such selection biases.

Kulas et al. (2013) studied the MZR of a protocluster sample at $z = 2.3$ and compared it with field galaxies at the same redshift. Both samples are selected based on their rest-frame UV emission. The gas-phase metallicity of their sources is calculated using N2 indicator. In the lower stellar mass bin ($M_* \sim 10^{10} M_\odot$), they found an offset of 0.15 dex between the metallicity of protocluster and field galaxies, i.e., their field sample is more metal deficient than the protocluster. Our result is in contrast with their findings, possibly due to the fact that they did not employ mass-matched samples.

Also, in the stellar mass range covered in this paper, Shimakawa et al. (2015) found metallicity enhancement ($\sim 0.15$ dex) for two protoclusters at $z = 2.2$ and $z = 2.5$ compared to the field sample of Erb et al. (2006) at $z = 2.2$. A part of this enhancement can be caused by different selection criteria they used for protocluster and field samples (Their protoclusters are narrow-band selected, but the field sample from Erb et al. (2006) is UV-selected). Comparing our field sample with the UV-selected sample of Erb et al. (2006), we notice that in the low-mass end of the MZR, the narrow-band selected sample has systematically higher metallicity compared to the UV-selected sample. Thus, the disagreement between the present work and Shimakawa et al. (2015) can be originated from selection biases.

Kacprzak et al. (2015) found no significant difference between the MZR of a protocluster at $z = 2$ and a field sample at the same redshift. On the other hand, Valentino et al. (2015) found that a protocluster sample at $z \sim 2$ with $M_* \sim 10^{10.5} M_\odot$ is 0.25 dex metal deficient compared to field galaxies at the same redshift. Their results are in qualitative agreement

with the results in this study; however, we find $\sim 0.1$ dex metal deficiency for protocluster galaxies compared to the field sample in the massive end of the MZR at $z \sim 2.2$. Moreover, Chartab et al. (2021) recently studied the environmental dependence of the MZR for a sample of H-band selected galaxies in the MOSDEF survey at $1.37 \leq z \leq 2.61$. For a mass-matched sample in the redshift range $2.09 \leq z \leq 2.61$, they found $\sim 0.07$ dex metal deficiency for galaxies in overdense regions compared to field galaxies. As shown in the bottom panel of Figure 2.5, our results are in agreement with their findings. Additionally, they found that this metal deficiency increases by the stellar mass, which is also seen in our result in Figure 2.5 (top panel).

## 2.5 Summary and Discussion

In this paper, we studied the mass-metallicity relation for 19 galaxies in a spectroscopically confirmed protocluster at $z \sim 2.2$ in the COSMOS field and compared it with the MZR of a field sample with 24 galaxies at the same redshift. We used $\frac{[\mathrm{NII}]\lambda 6584}{\mathrm{H}\alpha}$ ratio to measure the gas-phase metallicity of these galaxies. After matching the stellar mass distributions of field and protocluster samples, we found that the protocluster galaxies with $10^{9.9}\mathrm{M}_{\odot} \leq \mathrm{M}_{*} \leq 10^{10.9}\mathrm{M}_{\odot}$ are $0.10 \pm 0.04$ dex ($2.5\sigma$ significance) metal deficient in comparison to field galaxies at the same redshift. However, this metal deficiency is not significant for low-mass galaxies.

Darvish et al. (2020) predicted that this protocluster will grow to a Coma-type cluster with $\sim 9 \times 10^{14}\mathrm{M}_{\odot}$ at $z = 0$. Dekel and Birnboim (2006) found that at $z \lesssim 2$, halos with $\mathrm{M}_{\mathrm{halo}} \gtrsim 10^{12}\mathrm{M}_{\odot}$ will be dominated with hot-mode accretion. However, as we go to higher redshifts, cold streams can penetrate massive halos from filaments hosting dense pristine gas (Kereš

et al., 2005). Based on halo mass evolution trajectories of Behroozi et al. (2013b), we estimate that the progenitor of this protocluster at $z \gtrsim 2.5$ has $M_{halo} \lesssim 10^{13.5} M_{\odot}$, where the protocluster is in a phase that hosts cold streams in hot media (Dekel and Birnboim, 2006). Therefore, the observed protocluster at $z = 2.2$ was experiencing cold streams until $\sim 0.5$ Gyr ago ($z \geq 2.5$), which dilutes the gas-phase metallicity of galaxies residing in the protocluster. After the termination of cold streams, the protocluster galaxies continue to process their gas reservoirs until their star formation fully shuts down. However, 0.5 Gyr is a short time for the protocluster galaxies to significantly enrich their ISM metal content due to star formation. As a result, we are still witnessing metal deficiency for the members of this protocluster at $z = 2.2$ compared to field galaxies. We also expect that the SFRs of the protocluster galaxies increase due to a higher fraction of cold gas, but we are not able to confirm this effect, possibly due to the small sample size and inherent uncertainties in SED-derived and H$\alpha$ (mass-dependant extinction corrected) SFRs, which prevent us from detecting weak environmental dependence of SFR at a given $M_*$. Future *H*-band spectroscopies of our sample can properly constrain the environmental dependence of SFR given the dust-corrected H$\alpha$ luminosities, where the attenuation is derived from Balmer decrements.

In addition, the prevalence of minor/major mergers in dense environments at high redshifts (Hine et al., 2016; Watson et al., 2019) can explain a part of the metal deficiency observed in the present work. Although we exclude potential ongoing mergers in our sample, our protocluster galaxies could be descendants of recently-merged galaxies at higher redshifts. Minor and major mergers could provide a higher fraction of cold pristine gas for galaxies, increasing their SFR and lowering their metallicities (Horstman et al., 2020).

Moreover, the stellar mass dependence of metal deficiency (i.e., the absence of significant metal deficiency for low mass galaxies) can be explained by: 1) Massive galaxies located in deeper potential wells, being fed by metal-poor cold streams from the cosmic web (Dekel et al., 2009b), 2) Scaling of the merger fraction with the stellar mass of the galaxies. Duncan et al. (2019) showed that the major merger fraction for massive galaxies ($M_* > 10^{10.3} M_\odot$) is 3 times higher than low mass galaxies with $10^{9.7} M_\odot < M_* < 10^{10.3} M_\odot$ at $z = 2$.

We speculate that the metal content of the protocluster members will rapidly increase at lower redshift as all the remaining cold gas reservoirs will be processed through star formation activity. In addition, the IGM gas within the protocluster will be enriched due to strong outflows, which will then reaccrete into galaxies and enhance their gas-phase metallicity. This metal enhancement at lower redshifts in dense environments compared to field galaxies is observed in previous studies (e.g., Cooper et al., 2008; Ellison et al., 2009; Darvish et al., 2015).

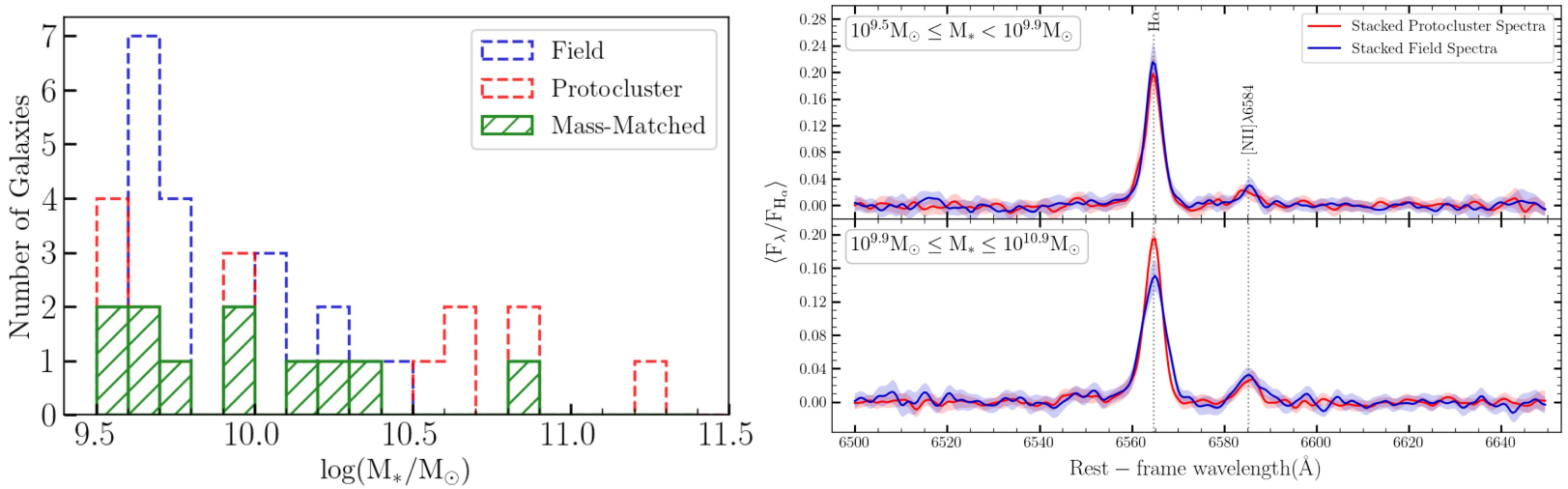


Figure 2.4: *Left*: The stellar mass distributions for the field (blue) and protocluster (red) galaxies. The green hatched region shows the matched stellar mass distributions of protocluster and field galaxies. *Right*: Composite spectra for the mass-matched samples in two bins of stellar mass ($10^{9.5}M_\odot \leq M_* < 10^{9.9}M_\odot$, and $10^{9.9}M_\odot \leq M_* \leq 10^{10.9}M_\odot$). The stacked spectra of protocluster galaxies are shown in red and the stacked spectra of field galaxies are shown in blue.

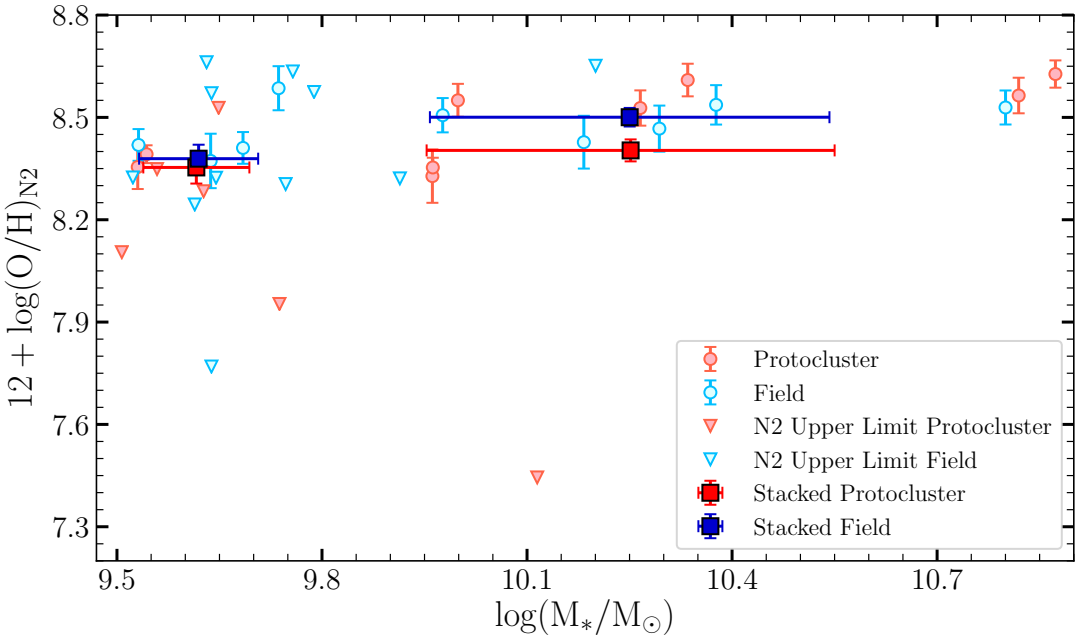


Figure 2.5: The MZR for the mass-matched samples at $z \sim 2.2$ for protocluster galaxies (red) and field galaxies (blue). Inverted triangles show [NII]$\lambda$6584 non-detections. The gas-phase metallicities for stacked spectra of protocluster and field samples in two stellar mass bins of $10^{9.5}M_\odot \leq M_* < 10^{9.9}M_\odot$, and $10^{9.9}M_\odot \leq M_* \leq 10^{10.9}M_\odot$ are also shown in red and blue squares, respectively. The horizontal error bars in the stacked data show $1\sigma$ scatter in stellar mass of each bin.

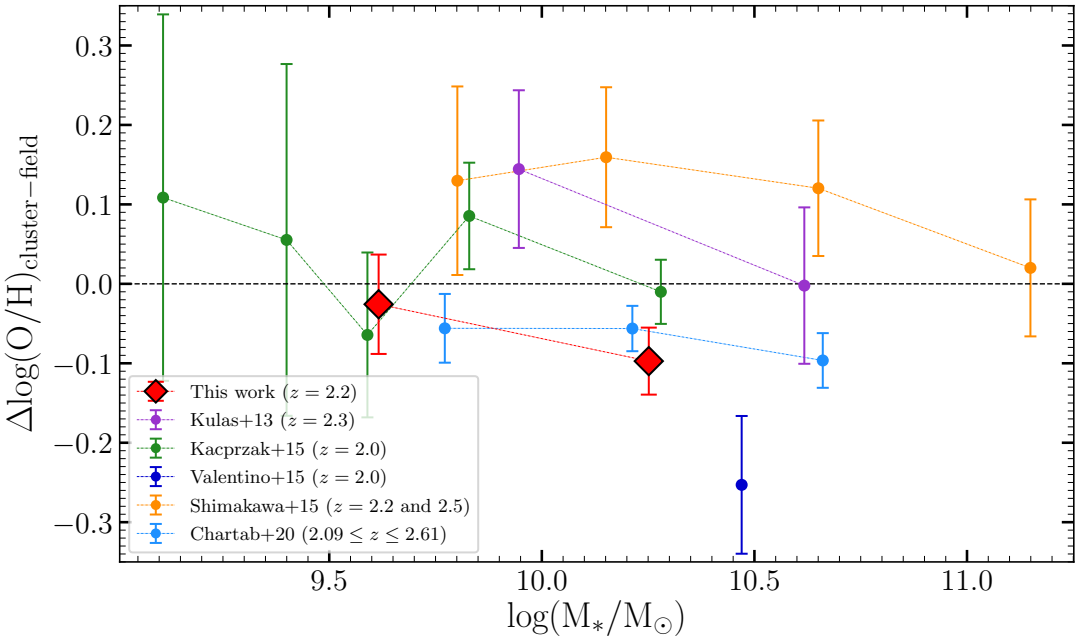


Figure 2.5: Continued - The compilation of the difference (offset) between gas-phase metallicity of protocluster and field galaxies as a function of stellar mass from literature. The red data points show the offset for the mass-matched samples used in this work in two stellar mass bins. The uncertainties in the offsets include errors from gas-phase metallicities of both protocluster and field samples.

# Chapter 3

# Fraction of Clumpy Star-forming Galaxies at $0.5 \leq z \leq 3$ in UVCANDELS: Dependence on Stellar Mass and Environment


## Abstract

High-resolution imaging of galaxies in rest-frame UV has revealed the existence of giant star-forming clumps prevalent in high redshift galaxies. Studying these sub-structures provides important information about their formation and evolution and informs theoretical galaxy evolution models. We present a new method to identify clumps in galaxies' high-resolution rest-frame UV images. Using imaging data from CANDELS and UVCANDELS, we identify star-forming clumps in an HST/F160W$\leq$ 25 AB mag sample of 6767 galaxies at $0.5 \leq z \leq 3$ in four fields,

GOODS-N, GOODS-S, EGS, and COSMOS. We use a low-pass band filter in Fourier space to reconstruct the background image of a galaxy and detect small-scale features (clumps) on the background-subtracted image. Clumpy galaxies are defined as those having at least one off-center clump that contributes a minimum of 10% of the galaxy's total rest-frame UV flux. We measure the fraction of clumpy galaxies ($f_{clumpy}$) as a function of stellar mass, redshift, and galaxy environment. Our results indicate that $f_{clumpy}$ increases with redshift, reaching $\sim 65\%$ at $z \sim 1.5$. We also find that $f_{clumpy}$ in low-mass galaxies ($9.5 \leq \log(M_*/M_\odot) \leq 10$) is 10% higher compared to that of their high-mass counterparts ($\log(M_*/M_\odot) > 10.5$). Moreover, we find no evidence of significant environmental dependence of $f_{clumpy}$ for galaxies at the redshift range of this study. Our results suggest that the fragmentation of gas clouds under violent disk instability remains the primary driving mechanism for clump formation, and incidents common in dense environments, such as mergers, are not the dominant processes.

## 3.1 Introduction

High-redshift star-forming galaxies (SFGs) frequently harbor compact regions of star formation, known as "clumps", which are abundant in cool gas (e.g., Conselice et al., 2004; Elmegreen and Elmegreen, 2005; Elmegreen et al., 2007; Bournaud et al., 2008; Förster Schreiber et al., 2011). These regions are fed by cold gas inflow from intergalactic medium (IGM) into the galaxy (Dekel and Birnboim, 2006; Dekel et al., 2009a), and their co-evolution with their host galaxy is affected by various processes within the galaxy or by incidents in the local environment (e.g., Dekel et al., 2009b; Mandelker et al., 2014, 2017). Several observational studies and simulations have suggested two commonly accepted scenarios for the formation of

these clouds: either they are formed through the fragmentation of gas clouds under gravitational instability of the violent disk (*in-situ*), or gas-rich minor mergers (*ex-situ*). The formation of clumps via violent disk instability (VDI) is supported by different simulations (e.g., Noguchi, 1999; Immeli et al., 2004a,b; Bournaud et al., 2007, 2009; Elmegreen et al., 2008; Genzel et al., 2008, 2011; Dekel et al., 2009b; Agertz et al., 2009; Ceverino et al., 2010, 2012; Inoue et al., 2016) and observations (e.g., Elmegreen et al., 2007; Guo et al., 2012, 2015; Shibuya et al., 2016; Hinojosa-Goñi et al., 2016; Mieda et al., 2016; Soto et al., 2017; Fisher et al., 2017; Zanella et al., 2019; Adams et al., 2022; Sok et al., 2022). However, there are also studies that indicate mergers as the origin of clump formation (e.g., Robertson and Bullock, 2008; Puech, 2010; Hopkins et al., 2013; Straughn et al., 2015).

Clumps are reported as regions exhibiting elevated specific star formation rates (sSFR; defined as star formation rate (SFR) per stellar mass) compared to their surrounding areas (Guo et al., 2012; Wuyts et al., 2012; Hemmati et al., 2014; Mieda et al., 2016; Mehta et al., 2021; Iani et al., 2021), with majority of them in the mass range $10^7 - 10^9$ $M_\odot$ (Elmegreen et al., 2007; Guo et al., 2012, 2015; Soto et al., 2017; Dessauges-Zavadsky et al., 2017; Huertas-Company et al., 2020; Ambachew et al., 2022). However, studies of high-redshift lensed systems revealed smaller stellar masses ($10^6$ $M_\odot$) and sizes ($\leq$ 100 pc) for clumps (Livermore et al., 2015; Johnson et al., 2017; Rigby et al., 2017; Cava et al., 2018; Dessauges-Zavadsky and Adamo, 2018; Dessauges-Zavadsky et al., 2019; Zick et al., 2020; Vanzella et al., 2021, 2022; Meštrić et al., 2022; Messa et al., 2022; Claeyssens et al., 2023) since, by utilizing these systems, we are able to achieve a significant increase in resolution, which allows for the investigation of much smaller scales than what is possible with field galaxies (Livermore et al., 2012; Adamo

et al., 2013; Johnson et al., 2017; Vanzella et al., 2019; Sharma et al., 2021; Meštrić et al., 2022; Welch et al., 2023).

Rest-frame ultraviolet (UV) images of galaxies trace their SFR over timescale of $\sim 100$ Myr associated with continuum from massive, short-lived O- and B-type stars (Calzetti, 2013). Thus, clumps can be detected in high-resolution imaging of field or lensed galaxies in rest-frame UV or optical (e.g., Conselice et al., 2004; Elmegreen and Elmegreen, 2005; Elmegreen et al., 2007; Taylor-Mager et al., 2007; Elmegreen et al., 2009; Förster Schreiber et al., 2011; Guo et al., 2012; Murata et al., 2014; Tadaki et al., 2014; Guo et al., 2015; Shibuya et al., 2016; Soto et al., 2017; Cava et al., 2018; Mager et al., 2018; Guo et al., 2018; Dessauges-Zavadsky and Adamo, 2018; Messa et al., 2019; Vanzella et al., 2021; Sok et al., 2022; Meštrić et al., 2022). There are, however, other studies that have identified clumps in H$\alpha$ emission line maps of galaxies (e.g., Genzel et al., 2008, 2011; Livermore et al., 2012; Mieda et al., 2016; Fisher et al., 2017; Zanella et al., 2019; Sharma et al., 2021) or in CO observations of lensed galaxies (e.g., Jones et al., 2010; Swinbank et al., 2010). In this work, we define clumps as off-center star-forming regions that can be detected in the rest-frame UV images of galaxies.

Clumps can also evolve within galaxies and contribute to their morphology. The evolution of the clumps within their host galaxies has been the subject of debate. Different observations and simulations support various scenarios, such as the migration of clumps towards the center of the galaxy and forming the progenitor of the galaxy's present bulge due to dynamical friction or clump-clump interaction (e.g., Dekel et al., 2009b; Ceverino et al., 2012; Mandelker et al., 2014; Shibuya et al., 2016; Soto et al., 2017; Mandelker et al., 2017; Mehta et al., 2021; Dekel et al., 2022). However, other simulations found that stellar feedback can disturb these

clumps and even destroy them before migrating to the center and thus, they have a short lifetime. In this scenario, disrupted clumps contribute to the formation of thick disks in their host galaxies (e.g., Murray et al., 2010; Genel et al., 2012; Hopkins et al., 2012; Moody et al., 2014).

Despite our current understanding, the formation and evolution of clumps in galaxies remains poorly understood and requires further study to help refine and constrain theoretical models. By examining clumps in galaxies, we can gain valuable insights into the history of their host galaxies. Moreover, their study has the benefit of testing the validity of feedback models in simulations. However, observations of clumps are challenging due to the limited spatial resolution specially of high redshift galaxies. With the advent of sensitive detectors on space telescopes, we can obtain multi-waveband imaging data with much higher spatial resolution for high-redshift galaxies.

In this paper, we identify star-forming clumpy regions in the rest-frame 1600 Å images of galaxies using data from The Cosmic Assembly Near-IR Deep Extragalactic Legacy Survey (CANDELS; Grogin et al., 2011; Koekemoer et al., 2011) and Ultraviolet Imaging of the Cosmic Assembly Near-infrared Deep Extragalactic Legacy Survey (UVCANDELS; Wang et al. in preparation) in the redshift range of $0.5 \leq z \leq 3$. We introduce a new method to subtract the smooth component of galaxy images and detect clumps in the residual images. We then investigate how the fraction of clumpy galaxies changes as a function of galaxy properties, such as stellar mass and environment. Studying such scaling relations can inform us about the details of clump formation within galaxies. Mainly, the environmental dependence of the clumpy fraction is studied for the first time, providing an opportunity to test scenarios concerning the formation history of clumps through mergers. Moreover, we study the redshift evolution of clumpy galaxies and

compare our results with previous studies. We discuss the evolutionary path of clumpy galaxies and address discrepancies between our work and previous studies.

The paper is structured as follows. In Section 3.2, we provide a description of the dataset used, including the criteria for sample selection. The methodology for identifying clumps within galaxies is explained in Section 3.3, where we also assess the completeness and reliability of our identification technique. In Section 3.4, we explore the measurements of the clumpy fraction in galaxies and analyze how these fractions evolve across different global properties of galaxies. Additionally, this section delves into the relationship between the clumpy fraction and redshift and includes a comparative analysis with findings from previous studies in the literature. We discuss the physical implications of our results and provide a summary in Section 3.5.

Throughout this paper, we assume a flat ΛCDM cosmology with $H_0 = 70$ kms$^{-1}$Mpc$^{-1}$, $\Omega_{m_0} = 0.3$ and $\Omega_{\Lambda_0} = 0.7$. All the physical parameters are measured assuming a Chabrier (2003) initial mass function (IMF) and magnitudes are represented in the AB system.

## 3.2 Data

### 3.2.1 Catalogs and Mosaics

We conduct a detailed analysis of rest-frame UV images of galaxies to identify star-forming clumps. We select galaxies from multi-wavelength catalogs in four CANDELS fields: GOODS-S (Guo et al., 2013), GOODS-N (Barro et al., 2019), COSMOS (Nayyeri et al., 2017), and EGS (Stefanon et al., 2017). Each of GOODS-S and GOODS-N fields covers an area of 170 arcmin$^2$ with $5\sigma$ limiting AB magnitude depth of 27.36 (GOODS-S) and 27.8 (GOODS-N)

in the F160W band. Also, the areal coverage of COSMOS and EGS fields is 216 and 206 arcmin$^2$ with 5$\sigma$ limiting AB magnitude depth (in F160W band) of 27.56 and 27.6, respectively.

Recently, UVCANDELS survey with the Hubble Space Telescope (PI: H. Teplitz, Cycle 26 GO 15647) conducted UV observations of these four fields in WFC3/UVIS F275W and ACS/WFC F435W bands. For the redshift range of this study ($0.5 \leq z \leq 3$), F275W, F435W, and F606W bands probe the rest-frame UV 1600 Å at $0.5 \leq z < 1$, $1 \leq z < 2$, and $2 \leq z \leq 3$, respectively (Figure 3.1). We use 60-mas mosaics of aforementioned bands to identify clumps. Although 30-mas mosaics can also be used due to the smaller pixel scale of the ACS instrument, 60-mas images provide sufficient resolution to probe our desired clumps with the size of ∼kpc, which contribute significantly to the total SFR of galaxies (Section 3.3). The CANDELS/UDS field is not included in this study since it does not have observations in two of these bands (F275W and F435W).

To calculate the physical properties of galaxies such as their stellar mass ($M_*$) and SFR, the spectral energy distribution (SED) fitting is performed using Code Investigating GALaxy Emission (CIGALE; Boquien et al., 2019). In the SED fitting procedure, the new observations of F275W and F435W bands obtained by UVCANDELS are also added to the existing data. Moreover, photometric redshifts of the galaxies are taken from the UVCANDELS catalog that includes F275W and F435W photometry. The catalog combines the redshift probability distributions of three different codes to compute robust values for the photometric redshifts (Sunnquist et al. in preparation).

A detailed description of the SED fitting procedure will be published in a future paper (Mehta et al. in preparation). In brief, the synthetic spectral library of Bruzual and Charlot

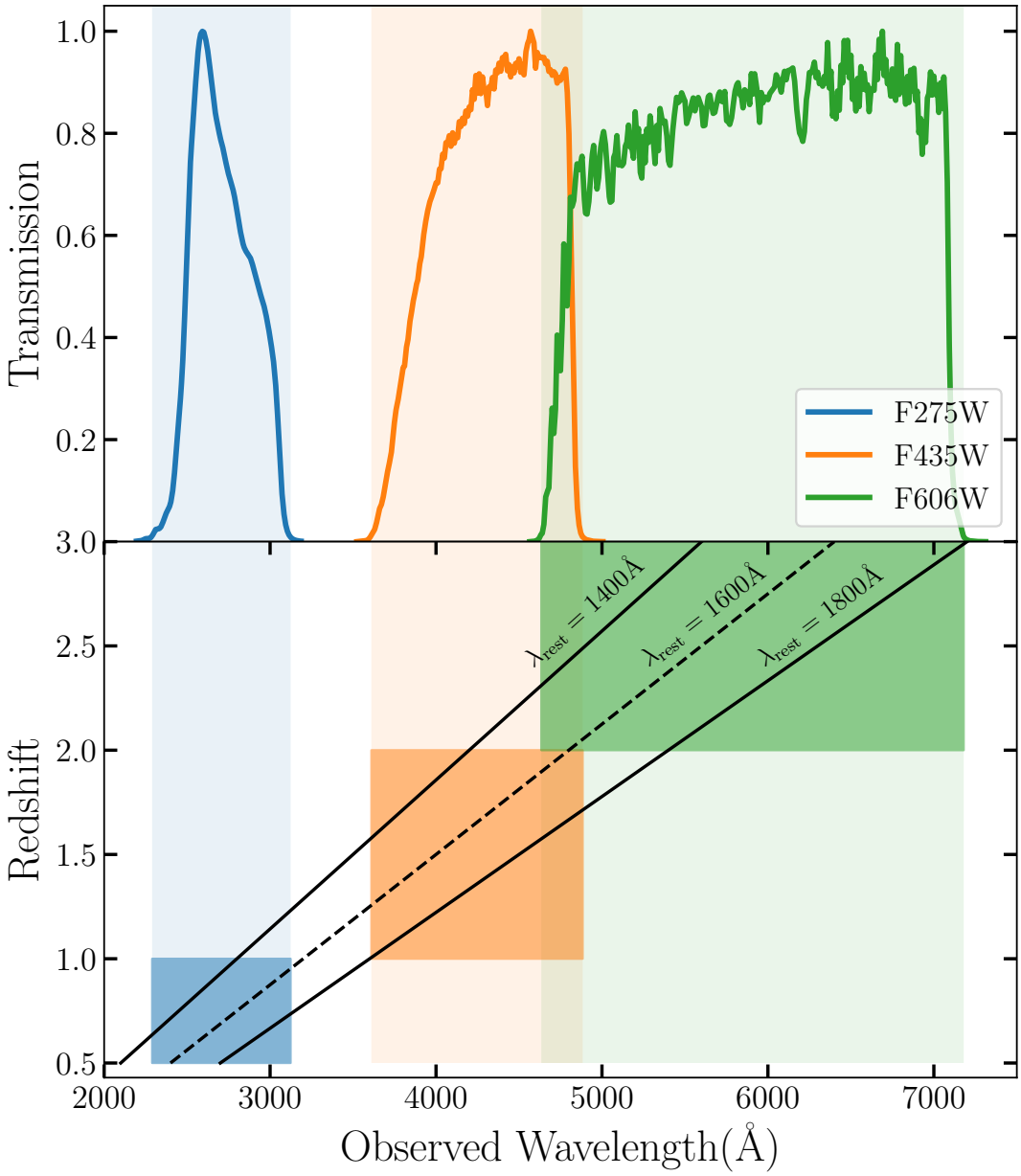


Figure 3.1: *Top*: Filter throughput (normalized to the peak transmission) for three wavebands that are utilized in this work. The shaded regions in the figure show the filter width with at least 1% of maximum transmission. *Bottom*: The observed wavelength of rest-frame 1400, 1600 and 1800 Å lines as a function of redshift. Blue, orange and green boxes correspond to rest-frame UV coverage for galaxies at the redshift range of $0.5-1, 1-2$, and $2-3$, respectively.

(2003) with the following assumptions is used to perform the SED fitting: A delayed exponentially declining star formation history ($te^{-t/\tau}$) with a range of 30 Myr to 30 Gyr e-folding time-scales ($\tau$) is considered. Additionally, we allow for the possibility of an episode of recent star-burst as a 10 Myr old burst with an exponential e-folding time of 50 Myr and the contribution of the burst is parameterized by the fraction of total mass generated in the burst. The code also includes the contribution of nebular emission lines. The stellar metallicities of Z = 0.0001, 0.0004, 0.004, 0.008, 0.02, 0.05, and a Calzetti et al. (2000) extinction law are adopted to generate the template SEDs and perform the fitting.

### 3.2.2 Sample Selection

The galaxy sample in this paper comprises HST/F160W (H band)-selected sources in four CANDELS fields: GOODS-S, GOODS-N, COSMOS, and EGS. Target galaxies are all covered by the desired HST/ACS and HST/WFC3 imaging data, i.e., galaxies with $0.5 \leq z < 1$, $1 \leq z < 2$ and $2 \leq z \leq 3$ have coverage in F275W, F435W and F606W bands, respectively.

SED-derived SFRs are well-constrained when rest-frame UV data are available. We, therefore, utilize a threshold defined by Pacifici et al. (2016) on the sSFR of galaxies to select a sample of star-forming galaxies. Based on this threshold, galaxies with sSFR$> 0.2/t_U(z)$ are identified as star-forming galaxies, where $t_U(z)$ is the age of the Universe at redshift $z$. We investigated the alternative UVJ color-color selection and obtained a similar sample. We also require all galaxies to have F160W $\leq$ 25 mag and $M_* \geq 10^{9.5} M_\odot$ over the redshift range of $0.5 \leq z \leq 3$. The stellar mass limit ensures a mass-complete sample within this study's redshift range.

Table 3.1: Summary of data utilized in this study.

| Field | Area (arcmin$^2$) | 5$\sigma$ Depth (AB) | N [1] |
|---|---|---|---|
| GOODS-S | 170 | 27.36 | 1572 |
| GOODS-N | 170 | 27.8 | 1870 |
| COSMOS | 216 | 27.56 | 1304 |
| EGS | 206 | 27.6 | 2021 |

Active galactic nuclei (AGNs) as well as stars (stellarity parameter of `SExtractor` (Bertin and Arnouts, 1996), CLASS_STAR $> 0.9$) are excluded from our sample. Also, to allow measurements of resolved images and identification of clumps, we select face-on galaxies with axial ratio (q) $> 0.5$ in their F160W images (the ratio of the major and minor axes). Furthermore, we require the size of the semi-major axis (SMA) of the galaxies to be $> 0.2$". All the above criteria lead us to a sample of 1572, 1870, 2021, and 1304 galaxies in the GOODS-S and GOODS-N, EGS, and COSMOS fields, respectively. Table 3.1 summarizes detailed information about the data and sample size.

## 3.3 Clump Identification

We detect clumpy regions in the rest-frame UV 1600 Å images of galaxies. The sample is divided into three redshift bins and we inspect images of galaxies in a filter that corresponds to the rest-frame UV wavelength in each redshift bin. Thus, we detect the clumps in F275W, F435W and F606W bands at the redshift ranges $0.5 \leq z < 1$, $1 \leq z < 2$, and $2 \leq z \leq 3$, respectively. We PSF-match all mosaics to the F160W band to achieve three goals. Firstly, to accurately distinguish clumps from bulges of host galaxies, it is beneficial to have a consistent definition of their centers, which are defined in the F160W band. Secondly, to minimize noise and ensure consistent clump detection throughout the redshift range, matching the PSF of the

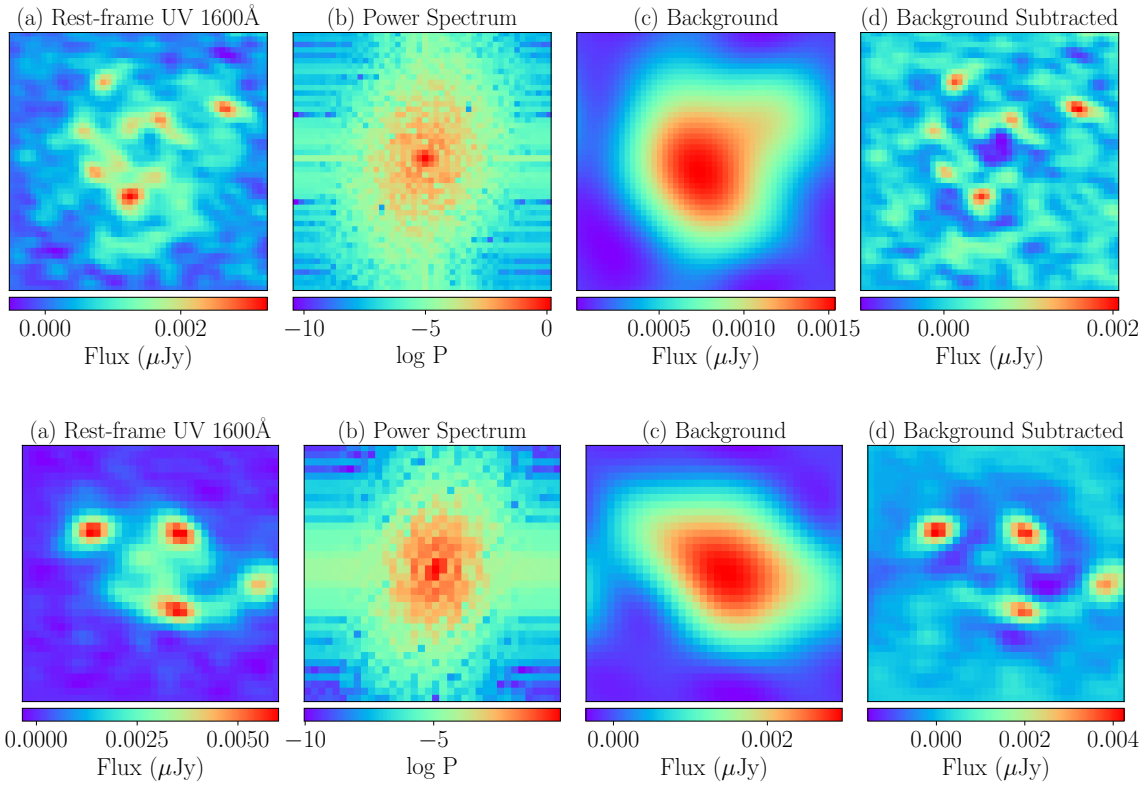


Figure 3.2: Two examples demonstrating the process of subtracting background from rest-frame UV images of galaxies. Panel (a) shows the galaxy image in the rest-frame UV filter. We calculate the power spectrum of this image in the Fourier space. Panel (b) shows log(power spectrum) in the frequency domain. After constructing the background map of the clump (Panel (c)), we remove it from the original image and the residual is an image which is ready to identify its clumps (Panel (d)).

other filters with that of the F160W band is advantageous. The FWHM of the F160W PSF is 0.17 arcseconds ($< 3$ pixels), which is less than the minimum number of pixels required to define a clump. Lastly, detection of clumps in PSF-matched images are necessary for future work that involves measuring SED of individual clumps.

### 3.3.1 Method

We first construct and subtract the local background of clumps in galaxy images. There are various ways to define and remove the background which involve subtracting the smooth background of the image that corresponds to large-scale variations compared to typical clump size. In this work, we use Fourier transformation to decompose small-scale features (i.e., clumps) from the smooth image of a galaxy.

One approach to construct the background of the clumps is to smooth the galaxy image with a custom kernel function (e.g., Gaussian function). This method usually has an underlying assumption about the symmetrical shape of galaxies and involves a hyper-parameter (i.e., the width of a kernel function) which controls the background construction and hence the clump identification. However, the diverse shape of galaxies, especially at high redshifts, needs to be modeled non-parametrically and asymmetrically to develop an effective clump identification technique.

In order to make an adaptive method to take into account the irregular morphology of the galaxies properly while constructing the background, we use a method based on Fast Fourier Transform (FFT) (SciPy; Virtanen et al., 2020). The steps involved in background subtraction are demonstrated in Figure 3.2. We first transfer the rest-frame UV image of the galaxy to Fourier (frequency) space. We then make the power spectrum map of the galaxy in this space (Panel

(b)). This map shows the power distribution coming from various scales (large-scale or small frequencies, and small-scale or high frequencies). The struggle to eliminate the background of the clumps now reduces to masking low frequencies in the FFT image since these frequencies represent the large-scale background features.

As previously stated, making a high-pass filter to mask the lower frequencies in the image is challenging because of the variety in the morphology of different galaxies. To effectively remove lower frequencies in an image of a galaxy, we first fit a 2-dimensional asymmetric Gaussian function to the power spectrum image of the galaxy to determine the values of standard deviation in the $x$ and $y$ directions ($\sigma_x$ and $\sigma_y$). Based on these values, we then employ a box high-pass filter (with the size of $2\sigma_x \times 2\sigma_y$) that is tailored to the specific galaxy. The filter is then convolved with the FFT image of the galaxy to construct the background-subtracted image where we identify clumps (Panel (d) in Figure 3.2). The background image is shown in panel (c) of Figure 3.2. Compared to the original image of the galaxy (Panel (a)), we can see most of the features corresponding to large-scale variations are removed in this image.

A similar background subtraction method has been used by Wang et al. (2015), who investigated the filamentary structures in Milky Way spiral arms. They considered a threshold of 90% of the maximum of the power spectrum and selected pixels above this cut as representatives of the low spatial frequencies (large-scale features of background). As described above, we avoid a constant threshold and compute it based on the power distribution of a galaxy in the frequency space.

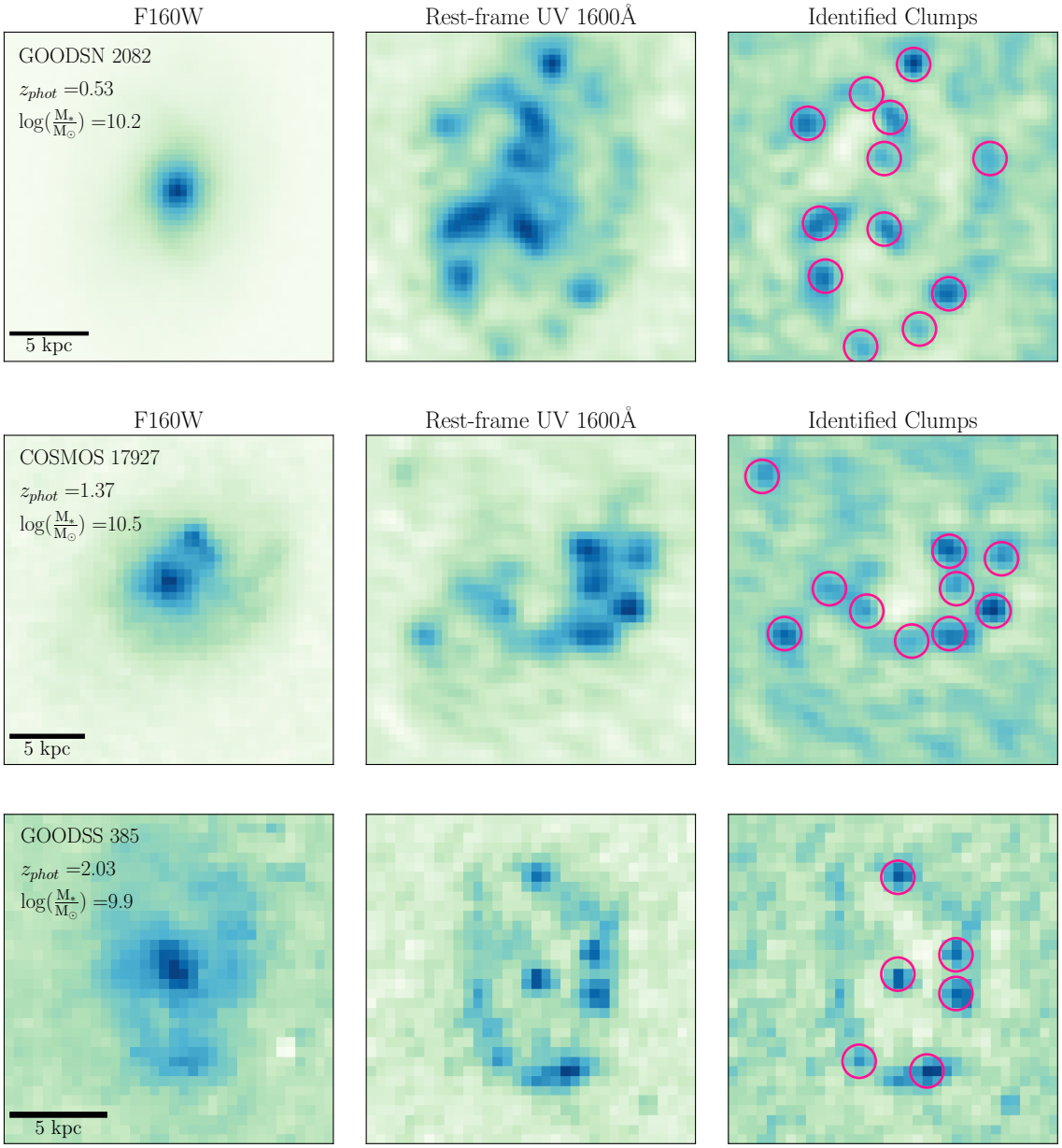


Figure 3.3: Eight examples of clumpy galaxies after identifying their clumps with magenta circles on their background-subtracted images in the right panels. Also, the left and middle panels show F160W and rest-frame UV 1600 Å images of these galaxies, respectively. In Section 3.3.2, we eliminate clumps that account for less than 10% of the total rest-frame UV flux of their host galaxies, resulting in a complete sample of clumpy galaxies. However, in this figure, we do not apply this requirement.

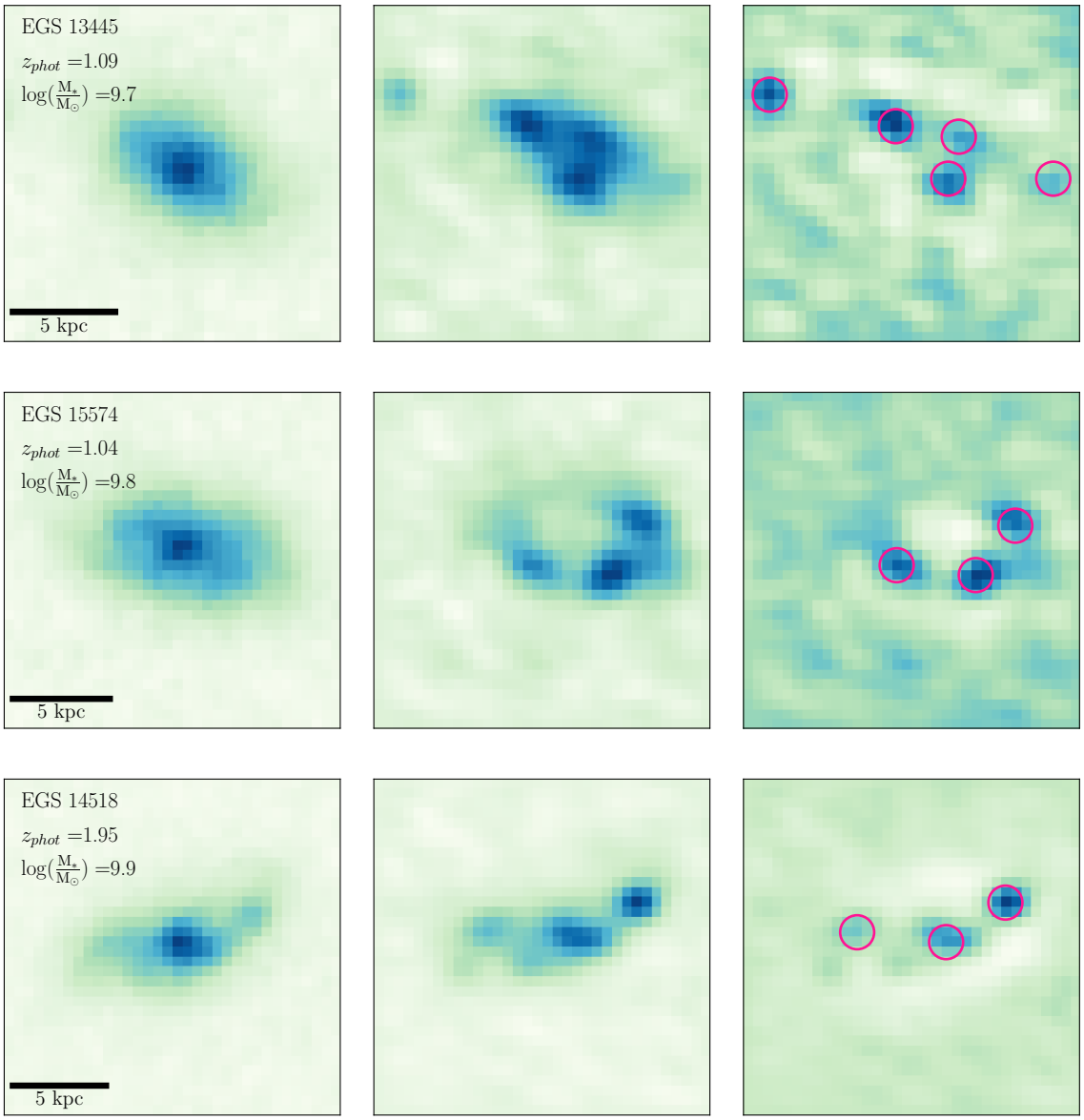


Figure 3.3: (Continued.)

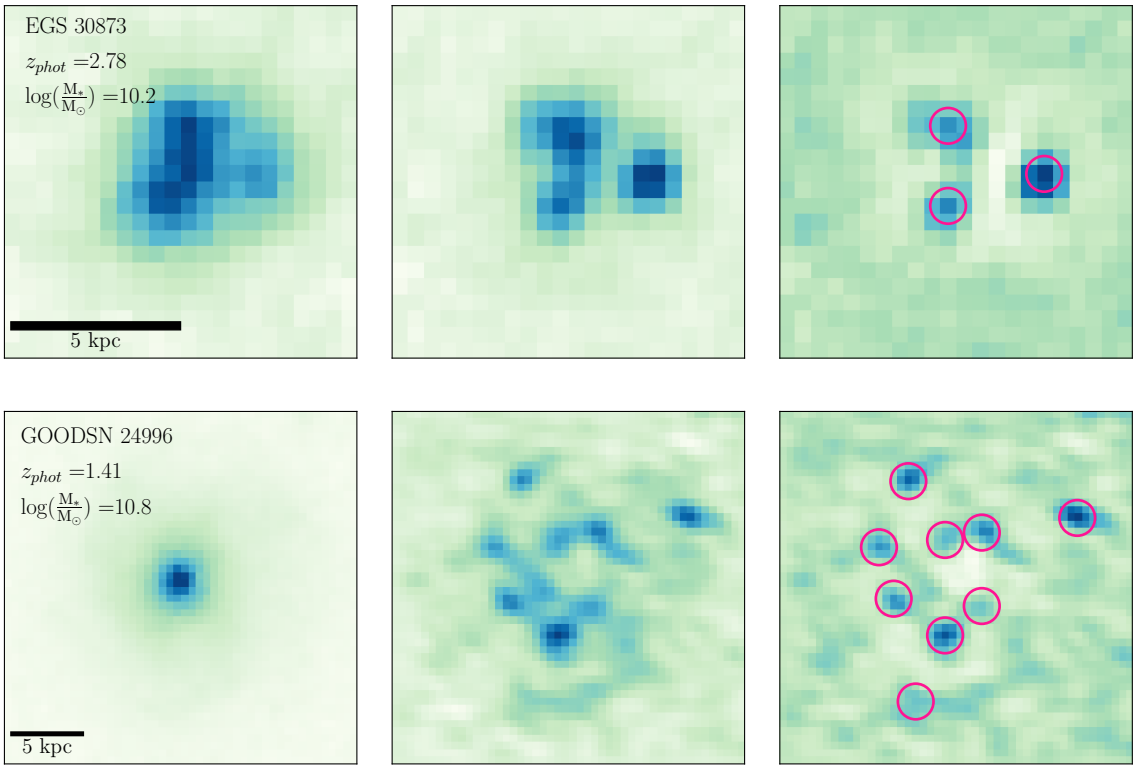


Figure 3.3: (Continued.)

After making a background-subtracted image for each galaxy, we use an image segmentation method to identify and isolate the clumpy structures within these galaxies. To perform the image segmentation, we utilize `Photutils` package (Bradley et al., 2020) and define a threshold to choose contiguous pixels ($\geq$ 4 pixels) that are $\sim 1.5\sigma$ above the background-subtracted image. The result of this procedure is an image of the clumps of the galaxy. To avoid the pixels that are in the noise level of the galaxy image, we only consider bright, robust clumps by requiring their signal-to-noise to be greater than 3 (S/N $\geq$ 3).

We also note that in the process of clump detection, the central bulge of the galaxy and possible contamination from other bright sources can be falsely detected as clumps. To avoid this, we exclude these objects by requiring a clump to be between $0''.1$ (to remove bulge) and 1.5×SMA from the center of the galaxy (to remove nearby sources) defined in the F160W band.

Figure 3.3 shows eight examples of clumpy galaxies with detected clumps after implementing the clump identification method (magenta circles in each image). This figure also shows the F160W images of these clumpy galaxies in the left panels. As we can see, most of these clumps in rest-frame UV images disappeared in the H-band filter. An H-band image primarily reveals the stellar mass distribution of a galaxy, while a rest-frame UV image traces its dust-unobscured SFR.

### 3.3.2 Success Rate of Clump Identification Method

To uniformly define which clumpy galaxies can be detected at all redshifts, we need to determine down to what flux limit we can detect clumps. To effectively evaluate the performance of our clump identification algorithm, we add one fake clump to the image of the galaxy

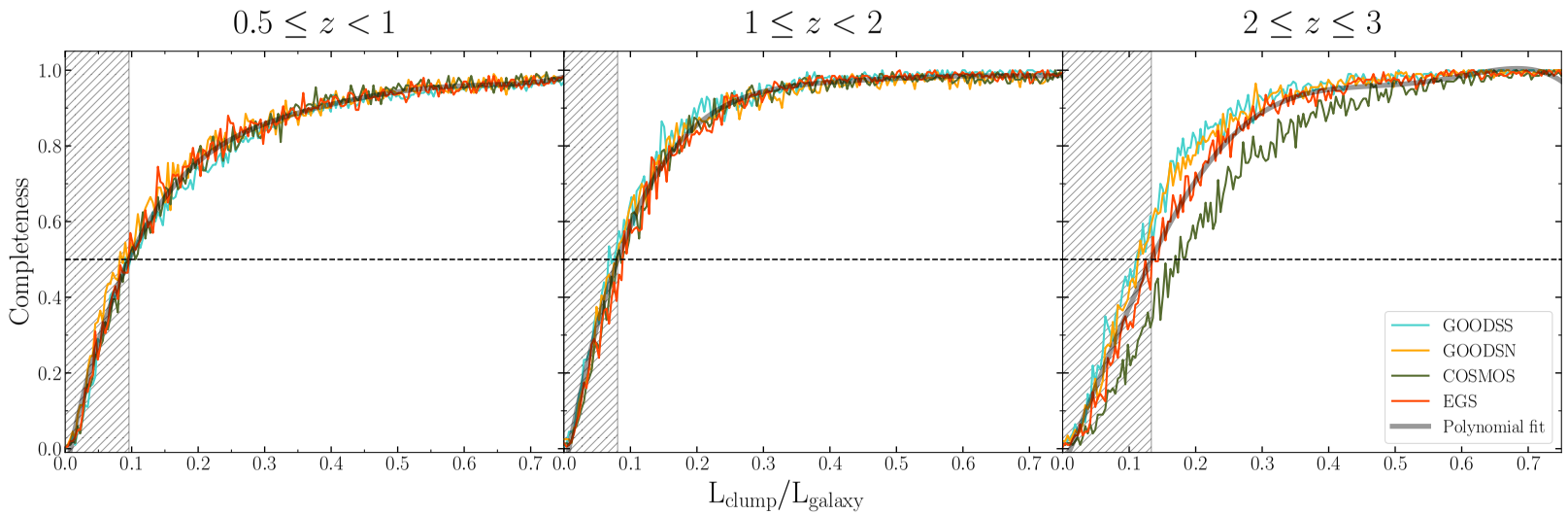


Figure 3.4: To estimate the completeness of our clump identification algorithm, we add one fake clump to each of 800 randomly-selected images of galaxies in four fields at each redshift bin, regardless of being clumpy or non-clumpy, and apply the clump identifier on them to see what percentage of fake clumps are recovered. The luminosity of the pseudo clumps are varied from 0.01% to 75% of the total rest-frame UV luminosity of the host galaxy. The horizontal dashed lines show the success rate of 50% in recovering fake clumps, which corresponds to the clumps that contribute at least $\sim 8-13\%$ to the rest-frame UV light of their host galaxy.

(whether it is clumpy or not) and test whether our algorithm can accurately detect and recover the inserted pseudo clump.

Following Guo et al. (2015), we add the pseudo clump to the rest-frame UV image of the galaxy in the desired band using the PSF image of the F160W (H band) band as a point source. The reason to use the H band PSF as a fake clump is that all galaxy images are PSF-matched to this band, and thus, the resolution of the rest-frame UV images is similar to that of the H band.

The position of the artificial clump is selected randomly within the size of the galaxy. We vary the flux of the fake clump from 0.01% to 75% of the total rest-frame UV flux of the host galaxy. To test the completeness of the clump finder, we randomly select 200 galaxies in each of the four fields at each redshift bin and perform the process of adding fake clumps. We then feed these galaxy images with fake clumps to our clump identification algorithm to estimate how successful we are in recovering the artificial clumps. Figure 3.4 shows the success rate of clump identifier as a function of the ratio of the clump luminosity to the host galaxy for four fields of GOODS-S, GOODS-N, COSMOS, and EGS in three different redshift bins defined in this work. The horizontal dashed lines show the success rate of 50% which corresponds to the clumps that include at least $\sim 8-13\%$ of the galaxy's rest-frame UV flux.

Based on the simulations of clump recovery, we define a galaxy as clumpy if it has at least one off-center clump that is brighter than 10% of the rest-frame UV flux of the galaxy. We conduct experiments with varying threshold values from 8% to 15% and find that our results in this study remain consistent, regardless of the chosen 10% threshold for the clump-to-galaxy flux ratio. Furthermore, we explore using variable thresholds at each redshift to maintain a

50% completeness rate, yet still observe no significant impact on our findings. In the following section, we perform aperture photometry on the clumps of each galaxy and calculate their rest-frame UV fluxes.

### 3.3.3 Aperture Photometry of Clumps

We perform fixed aperture photometry on each clump using `Photutils` package (Bradley et al., 2020). The radius of the aperture is fixed to be 3 pixels ($0''.18$) for each clump. To estimate the background of an individual clump, we consider two annuli with radii of 6 and 10 pixels around the clump and calculate the mean value of the pixels in between the two annuli. Since there might be contamination from other clumps in the background of each one, we mask all other clumps in a galaxy image while measuring the average background of the clump. We then subtract the average background from the total flux within the aperture radius. Using the PSF in F160W, we calculate that only $\sim$ 56% of the light from a point source is encompassed in a 3-pixel aperture radius. Thus, to measure the total flux of the clump, we scale the background-subtracted aperture by this value.

Using the total flux of individual clumps in the rest-frame UV band, we select those clumps that independently contribute $\geq$ 10% to the rest-frame UV luminosity of their host galaxy. This value is set based on Figure 3.4 that shows our clump identification method recovers $\sim$ 50% of the fake clumps with a flux ratio of $\geq$ 10% compared to the total flux of the host galaxy. The following section presents our results.

## 3.4 Results

In this section, we investigate the fraction of clumpy galaxies ($f_{clumpy}$) as a function of redshift and also the physical properties of galaxies, such as stellar mass and environment. In order for a galaxy to be considered clumpy, it must have $\geq 1$ off-center clump in its rest-frame UV 1600 Å image. The clumps of galaxies are identified using the methodology described in Section 3.3. Furthermore, we set a limit on the relative flux of clumps to their host galaxy such that the samples of clumps are $\geq$ 50% complete when identifying them (Section 3.3.2). We calculate the fraction of clumpy galaxies, which is the number of clumpy galaxies divided by the total number of galaxies in a given $M_*$, redshift or environment bin. The uncertainty in measuring $f_{clumpy}$ is also calculated using Poisson statistics from the galaxy number count.

### 3.4.1 Redshift Evolution

Figure 3.5 illustrates the clump distribution of galaxies in the bins of redshift and stellar mass for all the SFGs selected based on criteria mentioned in Section 3.2.2, in four fields of GOODS-S, GOODS-N, COSMOS, and EGS. We find that over the redshift range of our study $0.5 \leq z \leq 3$, clumpy galaxies have at most four off-center clumps that contribute more than 10% to the host galaxy's SFR. Moreover, galaxies with a higher number of clumps are mostly found at high redshifts ($z \gtrsim 1$).

Figure 3.6 shows the redshift evolution of $f_{clumpy}$ in three bins of stellar mass. The bins of redshift are considered such that in each bin, we have the same number of galaxies. As seen in Figure 3.6, the fraction of clumpy galaxies as a function of redshift follows almost

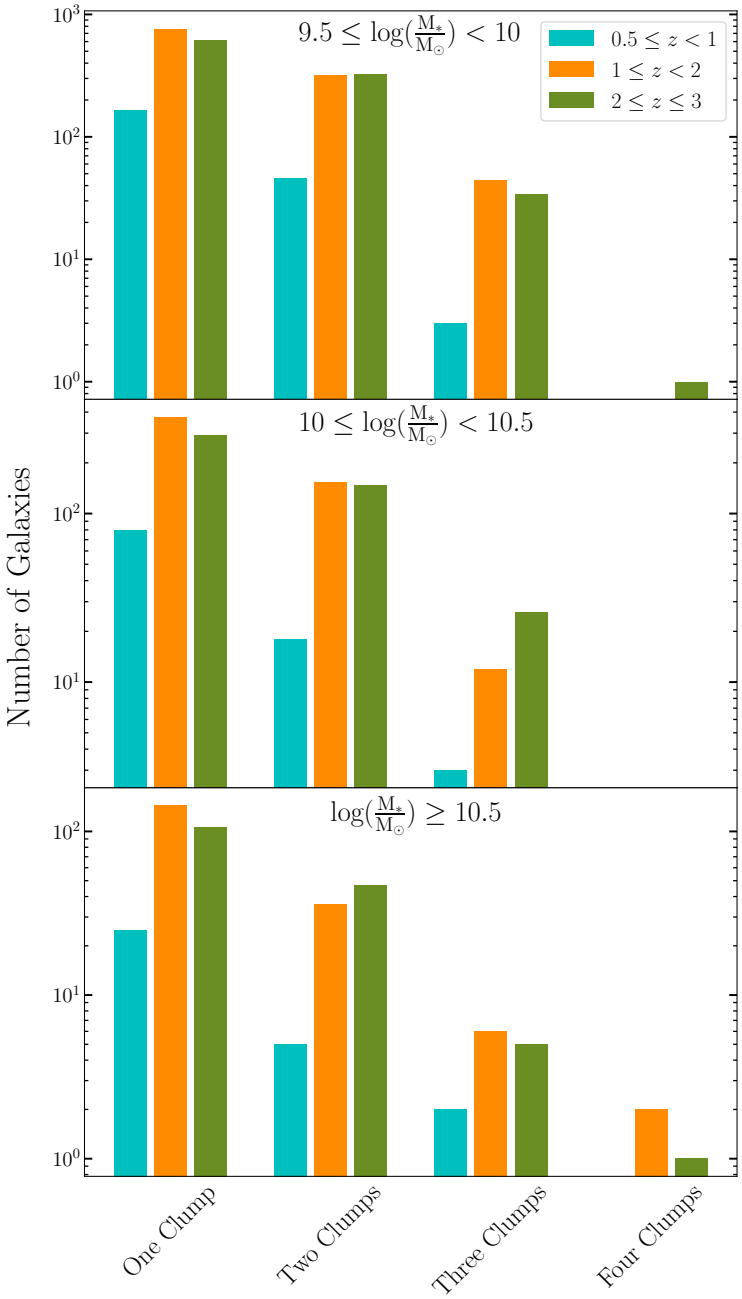


Figure 3.5: From top to bottom, each panel demonstrates the distribution of galaxies with one, two, three and four clumps that contribute > 10% to the rest-frame UV light of their host galaxies in the bins of redshift for three stellar mass ranges $9.5 \leq \log(\frac{M_*}{M_\odot}) < 10$, $10 \leq \log(\frac{M_*}{M_\odot}) < 10.5$ and $\log(\frac{M_*}{M_\odot}) \geq 10.5$, respectively.

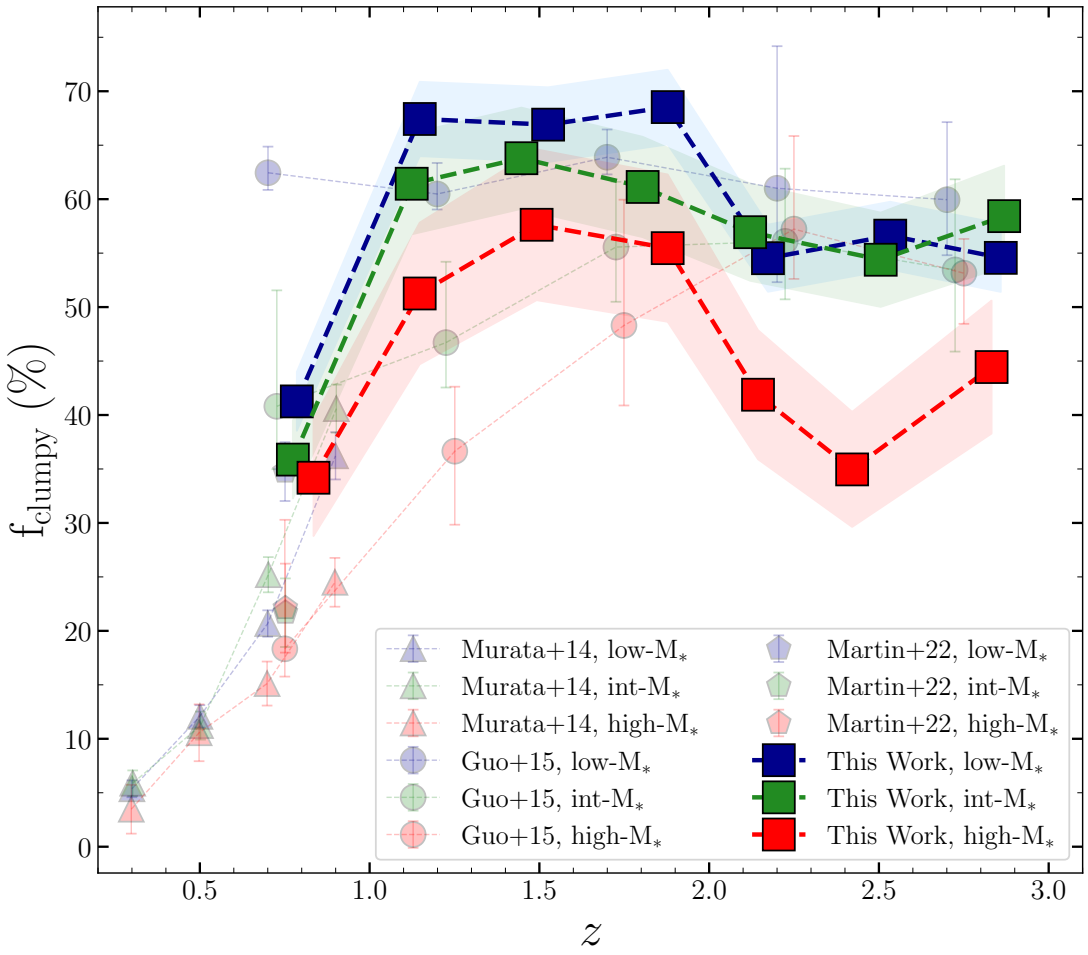


Figure 3.6: Fraction of clumpy galaxies as a function of redshift in three stellar mass bins (squares). Clumpy galaxies are those that have at least one off-center clump in their rest-frame UV images. Shaded regions correspond to $1\sigma$ uncertainty estimated from Poisson statistics. For comparison, measurements from Murata et al. (2014) (triangles), Guo et al. (2015) (circles) and Martin et al. (in preparation) (pentagons) are also added. The stellar mass bins in this works are the same as those of Murata et al. (2014) and Martin et al. (in preparation) (low-$M_*$: $9.5 \leq \log(\frac{M_*}{M_\odot}) < 10$, int-$M_*$: $10 \leq \log(\frac{M_*}{M_\odot}) < 10.5$, and high-$M_*$: $\log(\frac{M_*}{M_\odot}) \geq 10.5$). But Guo et al. (2015) binned the stellar mass of galaxies slightly different (low-$M_*$: $9 \leq \log(\frac{M_*}{M_\odot}) < 9.8$, int-$M_*$: $9.8 \leq \log(\frac{M_*}{M_\odot}) < 10.6$, and high-$M_*$: $10.6 \leq \log(\frac{M_*}{M_\odot}) < 11.4$).

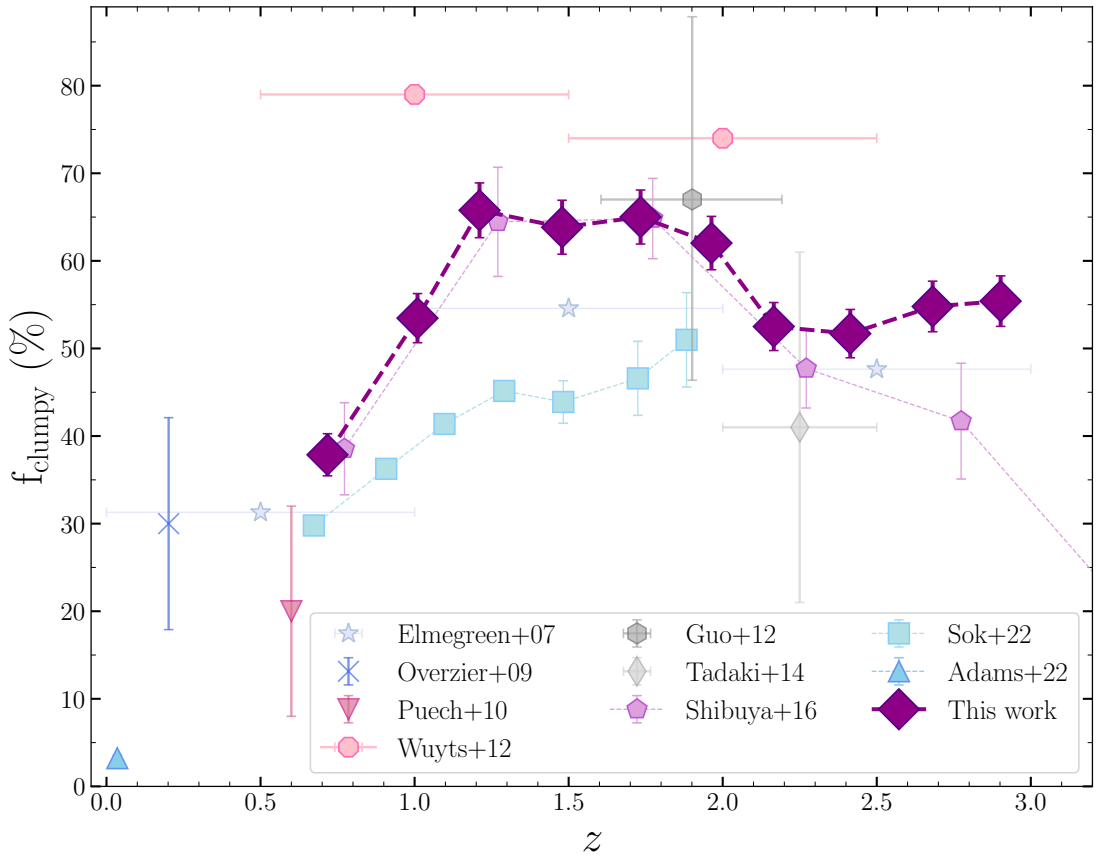


Figure 3.7: Same as Figure 3.6, but the fraction of clumpy galaxies is not binned by stellar masses. Also, more studies of clumpy fraction are added to the figure for comparison. Summary of previous studies on clumpy galaxies is presented in Table 3.2.

the same trend for all three stellar mass bins of low-mass, intermediate-mass and high-mass galaxies (blue, green, and red squares for galaxies with the stellar mass of $9.5 \leq \log(\frac{M_*}{M_\odot}) < 10$, $10 \leq \log(\frac{M_*}{M_\odot}) < 10.5$, and $\log(\frac{M_*}{M_\odot}) \geq 10.5$, respectively), with $f_{clumpy} \sim 35\% - 60\%$ at $z \sim 2.5$ increasing to $\sim 55\%$—$70\%$ at $z \sim 1.5$, and decreasing to $\sim 35\%$—$40\%$ at lower redshifts ($z < 1$). Furthermore, galaxies in higher stellar mass bin tend to have lower clumpy fraction compared to those with intermediate and lower stellar masses, especially at $z \sim 2.5$, where this fraction is $\sim 25\%$ lower for massive galaxies.

Additionally, we present $f_{clumpy}$ as a function of redshift for the entire sample regardless of their stellar masses in Figure 3.7. We find that the fraction of clumpy galaxies (shown with purple diamonds) is at its highest ($\sim 65\%$) in the redshift range $\sim 1-2$ and decreases to $\sim 40\%$ towards lower redshifts. Also, the trend is almost constant beyond $z \gtrsim 2$ with $f_{clumpy} \sim 50\%$.

As can be seen in Figure 3.6 — and repeated in Figure 3.7 with the average for the whole sample — there is a steep decline in the clumpiness of SFGs at late times, in a manner that appears to reflect the decline in star formation rate density (SFRD) (e.g., Madau and Dickinson, 2014). At early times, the data do not simply reflect the early rise in SFRD and there may be a number of issues that complicate the measurement and interpretations of clumpiness at those epochs.

To compare our clumpy fraction measurements with previous works, we show measurements of $f_{clumpy}$ in different redshifts from other studies in Figure 3.6 and 3.7 and summarize some of them in Table 3.2. Nevertheless, the definition of clumps varies across different studies, and various wavelengths can be used to identify them, so the comparison between different studies is qualitative.

Murata et al. (2014) studied the evolution of $f_{clumpy}$ as a function of redshift and reported an increase of clumpy galaxies with increasing redshift for galaxies at $0.2 < z < 1$. Our result is in general agreement with them in the low- and intermediate-mass bins. However, in the high-mass bin, we find a higher fraction of clumpy galaxies. Part of the discrepancy between our measurements and their values can be due to the detection band of clumps and the definition of clumpy galaxies. While Murata et al. (2014) considered at least three clumps as the criteria to select a clumpy galaxy in optical (HST/ACS F814W) images of galaxies, we

identify clumps in the rest-frame UV maps and determine clumpy galaxies with at least one off-center clump.

Another comprehensive study on the fraction of clumpy galaxies is done by Guo et al. (2015) with a sample of SFGs at $0.5 < z < 3$ in the two CANDELS/GOODS-S and UDS fields. They utilized rest-frame UV 2500 Å HST/ACS images of galaxies and detected clumps through an algorithm that identifies high-intensity pixels. A threshold of 8% is employed on the luminosity of the individual clumps relative to the host galaxy. Moreover, Shibuya et al. (2016) took a sample of SFGs, and Lyman break galaxies (LBGs) in five CANDELS fields, Hubble Ultra Deep Field and eXtreme Deep Field (HUDF and XDF; Beckwith et al., 2006; Bouwens et al., 2011; Illingworth et al., 2013; Ellis et al., 2013; Koekemoer et al., 2013) and the parallel fields of Abell 2744 and MACS0416 in the Hubble Frontier Fields (HFF; Coe et al., 2015; Atek et al., 2015; Oesch et al., 2015; Ishigaki et al., 2015) with a similar sample selection to Guo et al. (2015) and investigated the fraction of clumpy galaxies at $0 < z < 8$. They used the same definition of clumps and the detection algorithm as Guo et al. (2015).

Although our mass bins are slightly different from the ones employed by Guo et al. (2015), our result on the evolution of $f_{clumpy}$ for intermediate-mass galaxies is in qualitative agreement with theirs (green circles in Figure 3.6), which shows an increase of $f_{clumpy}$ with increase in redshift and then flattening around $z \sim 1.5$. However, this fraction in their low-mass bin is almost independent of redshift at all redshift bins (blue circles). In contrast, our result for this mass bin follows the same trend as our intermediate-mass bin. In the high-mass bin, Guo et al. (2015) reported a monotonically increasing $f_{clumpy}$ with redshift (red circles), while our measurement agrees on the increase out to $z \sim 1.5$ and then shows a sign of decrease at

Table 3.2: Summary of previous studies on clumpy galaxies in field.

| Reference | Sample ($N_{galaxy}$) | $\log(\frac{M_*}{M_\odot})$ [a] | Redshift | Method | Detection Band |
|---|---|---|---|---|---|
| Elmegreen et al. (2007) | Starbursts (1003) | N/A | 0-5 | Visual | F775W |
| Overzier et al. (2009) | LBAs (20) | 9-10 | ∼0.2 | Visual | $UV_{rest}$ |
| Puech (2010) | Emission-line galaxies (63) | $> 10$ | ∼0.6 | Visual | F435W |
| Guo et al. (2012) | SFGs (10) | $> 10$ | 1.5-2.5 | Algorithm | F850LP |
| Wuyts et al. (2012) | SFGs (649) | $> 10$ | 0.5-2.5 | Algorithm | rest-frame 2800 Å |
| Tadaki et al. (2014) | HAEs (100) | 9-11.5 | 2-2.5 | Algorithm | F606W & F160W |
| Murata et al. (2014) | $I_{F814W} < 22.5$ galaxies (24027) | >9.5 | 0.2-1 | Algorithm | F814W |
| Guo et al. (2015) | SFGs (3239) | 9-11.5 | 0.5-3 | Algorithm | $UV_{rest}$ 2500 Å |
| Shibuya et al. (2016) | Photo-z galaxies & LBGs (16910) | 9-12 | 0-8 | Algorithm | $UV_{rest}$ & $opt_{rest}$ |
| Huertas-Company et al. (2020) | SFGs (1500) | 9-11.5 | 1-3 | Algorithm | $UV_{rest}$ & $opt_{rest}$ |
| Adams et al. (2022) | SFGs (58550) | $> 9$ | 0.02-0.15 | Visual | $ugriz$ |
| Sok et al. (2022) | SFGs (20185) | $> 9.8$ | 0.5-2 | Algorithm | $U_{rest}$, $V_{rest}$ & $opt_{rest}$ |
| Martin et al. (in preparation) | SFGs (695) | $> 9.5$ | 0.5-1 | Algorithm | $UV_{rest}$ 1600 Å |
| This work | SFGs (6767) | $> 9.5$ | 0.5-3 | Algorithm | $UV_{rest}$ 1600 Å |

[a] Stellar mass range of sample used in each study.

higher redshifts. We speculate that part of this discrepancy, at least in the low-mass bin at low redshifts, is due to the fact that Guo et al. (2015) detected clumps in rest-frame Near-UV (NUV) images, while our study is conducted on the Far-UV (FUV) images. Recently, a study by Martin et al. (in preparation) is using UVCANDELS data to study demographics of clumpy galaxies at $0.5 \leq z \leq 1$ with a similar clump identification method to Guo et al. (2015) on the FUV images of galaxies. Their measurements of $f_{clumpy}$ are demonstrated by pentagons in Figure 3.6. At the redshift range of their study, our low-mass bin measurements are in agreement with theirs within the uncertainties.

Moreover, reported measurements of $f_{clumpy}$ as a function redshift by Shibuya et al. (2016) are shown in Figure 3.7 with pentagons. Our estimates agree well with theirs out to $z \sim 2$. However, with increasing redshift, their fraction of clumpy galaxies decreases while ours flattens. Other studies of clumpy galaxies have also investigated the evolution of clumpy galaxy fraction with redshift. For instance, a recent study by Sok et al. (2022) detected clumpy galaxies at $0.5 < z < 2$ by deconvolving ground-based images of galaxies in the COSMOS field to increase their resolution, and measured the fraction of clumpy galaxies (blue squares in Figure 3.7). Similar to ours, their $f_{clumpy}$ is increasing with redshift below $z \sim 2$.

In conclusion, the decline in clumpiness from cosmic noon to today is very well measured, regardless of technique. It is, therefore, possible that part of the decline in cosmic SFRD can be attributed to the decline in the prevalence of clumps, which are sites of star formation. The formation and evolution of clumps can be affected by various physical mechanisms, including both internal processes (e.g., stellar feedback, AGN activity) and/or external processes (e.g., galaxy interactions, strangulation). To constrain the dominant process responsible for

clump formation and evolution, in the following sections, we study $f_{clumpy}$ as a function of stellar mass and environment. Feedback processes scale with stellar mass of galaxies, therefore, any relationship between stellar mass and clumpy fraction indicates that internal processes are responsible for clump evolution, while any correlation with the environment indicates that external processes play a role.

### 3.4.2 Stellar Mass Dependence

We present the fraction of clumpy galaxies in redshift bins as a function of stellar mass in Figure 3.8. At all three redshift bins of $0.5 \leq z < 1$ (cyan squares), $1 \leq z < 2$ (orange squares), and $2 \leq z \leq 3$ (green squares) the fraction of clumpy galaxies decreases monotonically with increase in stellar mass. At low redshifts, $f_{clumpy}$ decreases from $\sim 40\%$ for galaxies with stellar masses in the range $9.5 \leq \log(\frac{M_*}{M_\odot}) < 10$ to $\sim 30\%$ for massive galaxies ($\log(\frac{M_*}{M_\odot}) \geq 10.5$). The slope of this decrease is steeper for galaxies at $z > 1$. At $1 \leq z < 2$, the fraction of clumpy galaxies decreases from $\sim 70\%$ to $\sim 55\%$ for galaxies with $9.5 \leq \log(\frac{M_*}{M_\odot}) < 10$ and $\log(\frac{M_*}{M_\odot}) \geq 10.5$, respectively. At the highest redshift bin, $f_{clumpy}$ is almost independent of stellar mass ($\sim 55\%$) for low-mass galaxies, but drops quickly to $\sim 40\%$ in massive galaxies.

For comparison, two other studies which have demonstrated the fraction of clumpy galaxies as a function of stellar mass are shown in Figure 3.8 as well. Guo et al. (2015) found that $f_{clumpy}$ is decreasing with the increase of stellar mass (cyan, orange and green circles), which is in agreement with our results. Moreover, Huertas-Company et al. (2020) used neural networks to detect clumps in the rest-frame optical and UV images of galaxies in the CANDELS fields and hydrodynamic zoom-in simulations of VELA (Ceverino et al., 2014) at $1 < z < 3$.

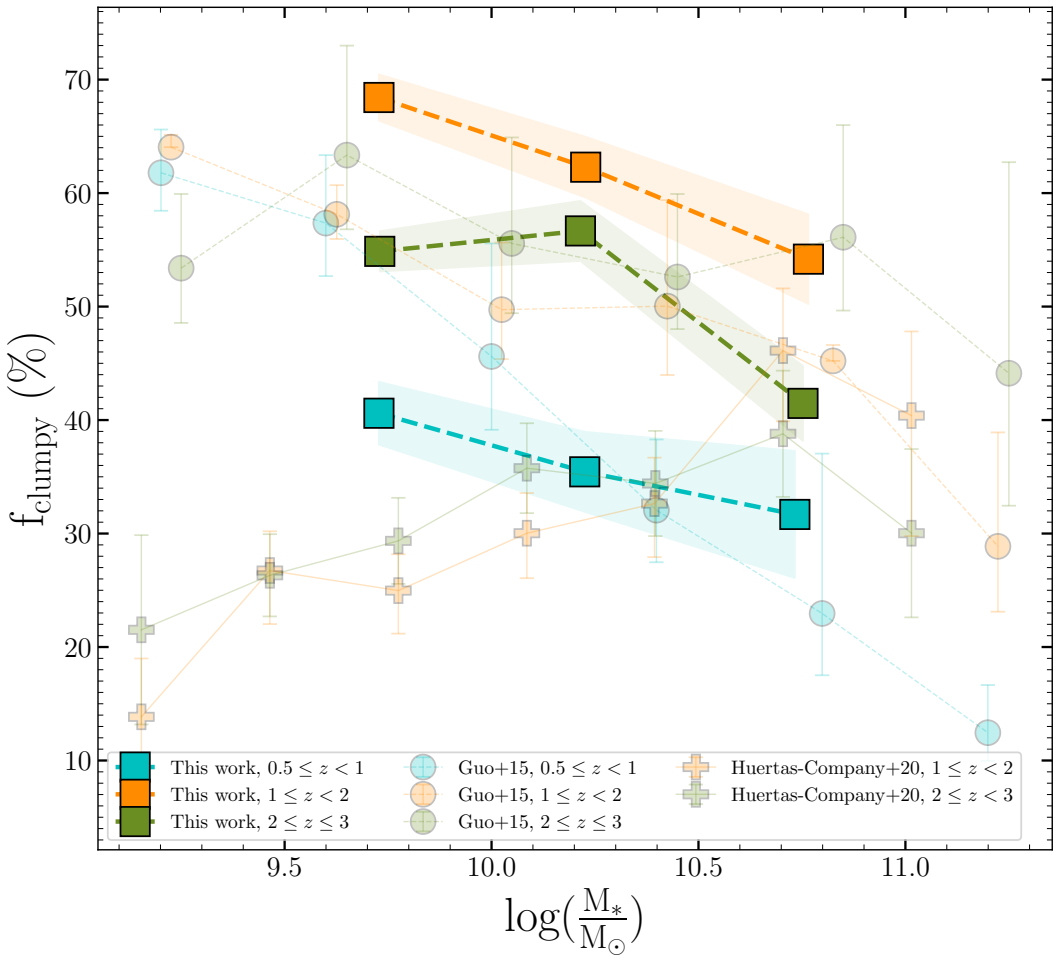


Figure 3.8: Fraction of clumpy galaxies as a function of stellar mass in different redshift bins. $1\sigma$ uncertainties of $f_{clumpy}$ measurements are shown with shaded regions that are calculated by Poisson statistics. Circle and plus data points show reported measurements from Guo et al. (2015) and Huertas-Company et al. (2020), respectively.

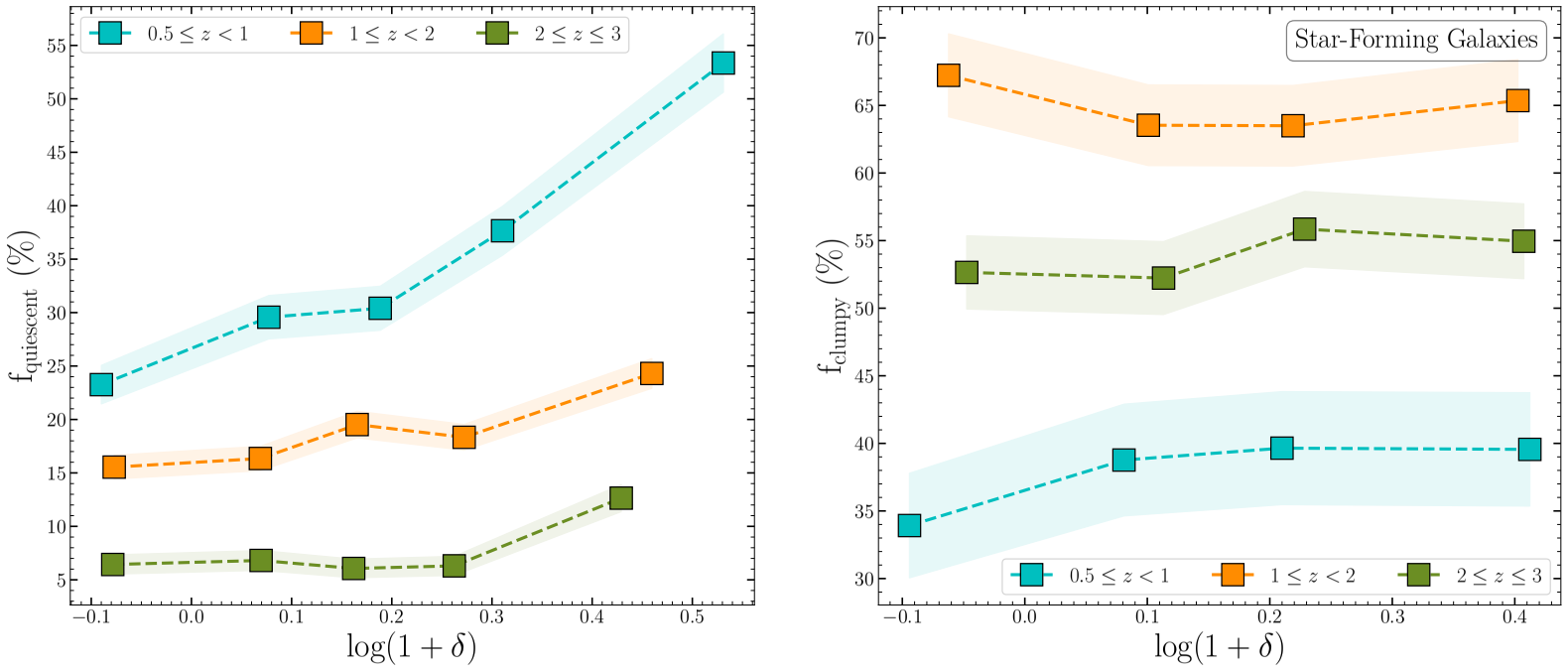


Figure 3.9: *Left*: Fraction of quiescent galaxies in different bins of redshift and environment. *Right*: Fraction of clumpy galaxies in SFGs as a function of environment in different redshift bins. Error bars (shaded regions) for both panels are estimated by Poisson statistics from the number count of galaxies.

They measured the fraction of clumpy galaxies as a function of stellar mass and redshift and found that $\sim$ 40% of galaxies with $\log(\frac{M_*}{M_\odot}) > 10$ are clumpy, and this fraction drops to $\sim$ 20% for low-mass ($\log(\frac{M_*}{M_\odot}) < 10$) galaxies (orange and green pluses). This result is in contrast with our clumpy fraction and those reported in Guo et al. (2015).

### 3.4.3 Environmental Dependence

It has been shown, at least at low redshifts ($z \lesssim 1$), that star formation activity of galaxies is strongly correlated with their surrounding environments (Patel et al., 2009a; Peng et al., 2010; Darvish et al., 2016; Chartab et al., 2020). Thus, clumps, which are sites of star formation in galaxies, may be linked to the local environment of their host galaxies, and by studying the environmental dependence of $f_{clumpy}$, one can gain insights into clump formation and evolution.

Several simulations and observational studies suggest that clumps join the disk of galaxies through minor mergers, and their formation is *ex-situ* (Hopkins et al., 2013; Straughn et al., 2015). As minor/major mergers are more prevalent in dense environments (Hine et al., 2016; Watson et al., 2019), examining the correlation between clumps and their host galaxies' local environment would constrain the clump formation mechanisms. It is possible that *ex-situ* formation is the dominant process of clump formation in galaxies if the clumpy fraction is correlated with the local environment.

Our sample of galaxies, located in four CANDELS fields, has local environmental measurements available from the catalog of Chartab et al. (2020), which includes measurements of local density for galaxies with HST/F160W $\leq$ 26 AB mag in all the CANDELS fields. They recon-

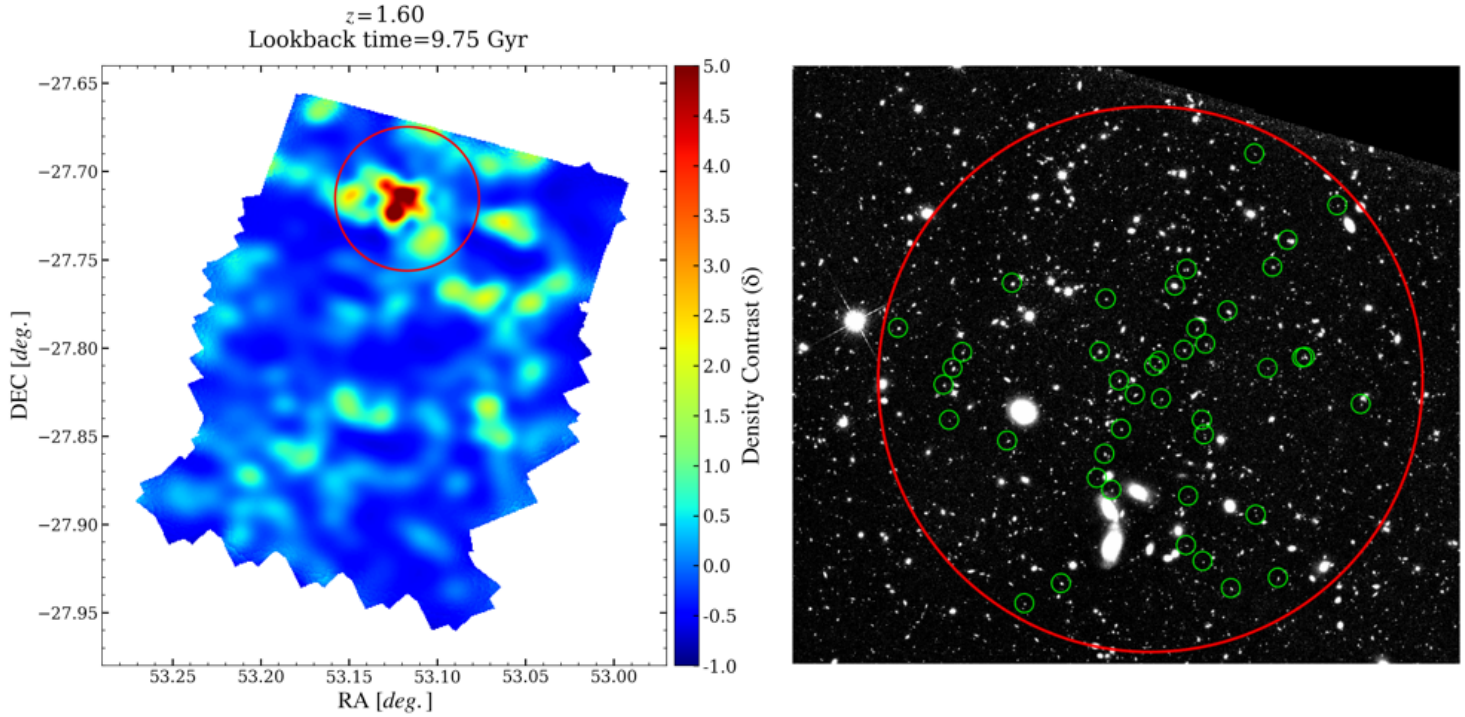


Figure 3.10: *Left*: Density map of the GOODS-S field at the redshift of the spectroscopically-confirmed cluster adopted from Chartab et al. (2020), which is color-coded by density contrast. The density map confirms the existence of this over-density at $z = 1.61$ in the red clustered region. The red circle with the radius of 1 Mpc (physical) indicates the boundary of this cluster which encloses the cluster members. *Right*: The footprint of this cluster at $z = 1.61$ in the sky. Green circles show the members of the cluster, while the red one is the same as the red circle in the left panel.

structed density maps of galaxies probabilistically using the weighted kernel density estimation method in a wide redshift range ($0.4 < z < 5$). Their density measurements are based on uniformly calculated photometric redshifts with well-calibrated probability distributions across the CANDELS fields (Kodra et al., 2022). In this work, we utilize the local density catalog of Chartab et al. (2020) to study the fraction of clumpy galaxies in different environments. For a full description of environment measurements, we refer readers to Chartab et al. (2020, 2021). We note that due to the limited size of CANDELS fields, these density measurements only probe the galaxy groups and cores of the structures rather than extended structures such as protoclusters (Chartab et al., 2021).

It is well-known that the fraction of quiescent galaxies is positively correlated with the local density contrast ($\delta$), especially at $z \lesssim 1$ (Patel et al., 2009a; Peng et al., 2010; Balogh et al., 2016; Kawinwanichakij et al., 2017; Darvish et al., 2017; Chartab et al., 2020). The left panel in Figure 3.9 demonstrates the fraction of quiescent galaxies as a function of local environment $(1 + \delta)$ for a sample of galaxies with F160W $\leq$ 25 mag and $M_* \geq 10^{9.5} M_\odot$ in three redshift bins used in the present work. We define quiescent galaxies with a cut on sSFR as described in Section 3.2.2. Across all redshift bins, we find a positive correlation, which is stronger at the lowest redshift bin ($0.5 \leq z < 1$). We also estimate the fraction of clumpy galaxies in three redshift bins as a function of their local environment for a sample of SFGs described in Section 3.2.2. The right panel of Figure 3.9 shows that the fraction of clumpy galaxies is almost independent of the environment in all three redshift bins of $0.5 \leq z < 1$ (cyan squares), $1 \leq z < 2$ (orange squares), and $2 \leq z \leq 3$ (green squares). $f_{clumpy}$ is constant around $\sim 35\%-40\%$, $\sim 50\%-55\%$, and $\sim 65\%$ from lower to higher redshift bin, respectively.

It suggests that in dense environments, there are rapid processes that quench galaxies before interfering with their clumps.

Moreover, the lack of a significant relationship between the clumpy fraction and the environment of galaxies may indicate that clumps are rather formed *in-situ* than *ex-situ*. It is possible, however, that measurements of clumpy fractions or the environments of galaxies are subject to large uncertainties, and any existing correlations might be too weak or subtle to be reliably detected by these measurement methods.

To assess this issue, we study the fraction of clumpy galaxies within a spectroscopically-confirmed cluster in the GOODS-S field around the redshift where the fraction of clumpy galaxies reaches its maximum ($z \sim 1.5$). This cluster has 42 spectroscopically-confirmed members at $z_{\rm med} = 1.61$ within $\Delta z = 0.01$, which is a virialized structure with X-ray detection (Kurk et al., 2009). Figure 3.10 shows the footprint of this cluster and its confirmed members in the sky (right panel), as well as the density map of GOODS-S field at $z = 1.6$ reconstructed by environment measurements of Chartab et al. (2020) color-coded by the density contrast (right panel). The red region in the left panel shows this over-density with $> 4\sigma$ significance. On the right panel, confirmed members of the cluster are identified by green circles, while the red circle indicates the boundary of the cluster, which has a radius of 1 Mpc (physical).

Out of 42 members of this cluster, 25 were in the stellar mass range of our study ($\log(\frac{M_*}{M_\odot}) \geq 9.5$). We perform clump detection analysis on the cluster members and found that 15 out of 25 of them are classified as clumpy, corresponding to an $f_{\rm clumpy}$ of 60% for this structure. We overlaid the measurement of $f_{\rm clumpy}$ for this cluster in the figure showing the fraction of clumpy galaxies as a function of redshift for our entire sample (Figure 3.11). We find

less than 5% discrepancy in the clumpy fraction of this structure compared to our total sample, which is insignificant and within the measurement uncertainties.

Our assessment of the environmental measurements by studying a spectroscopically-confirmed cluster confirms the lack of trend in Figure 3.9, implying that $f_{clumpy}$ is independent of the environment of galaxies. However, further studies are needed to confirm this for a statistically large sample of structures. The availability of future wide surveys with deep and high-resolution images will facilitate such studies as they will enable reliable measurements of the environment and deep-resolved images of galaxies.

## 3.5 Summary

In this paper, we identify star-forming clumpy sub-structures in the rest-frame UV 1600 Å images of SFGs selected from four CANDELS fields. The rest-frame UV at the redshift range of our study ($0.5 \leq z \leq 3$) is probed by F275W, F435W and F606W filters for which the observations are conducted by Hubble Space Telescope via UVCANDELS and CANDELS surveys. We utilize low-pass band filter in Fourier space to reconstruct the background image of the galaxies and subtract them from the galaxy images to detect clumps. We study the fraction of clumpy galaxies (the number of galaxies with at least one detected off-center clump in their images divided by the total number of galaxies) as a function of their host galaxies' physical properties, such as stellar mass and local environment. We also investigate the clumpy fraction evolution with redshift and compare our results with that of previous works. Moreover, clump statistics of a spectroscopically-confirmed cluster at $z = 1.61$ is calculated for 25 members. Our findings can be summarized as follows:

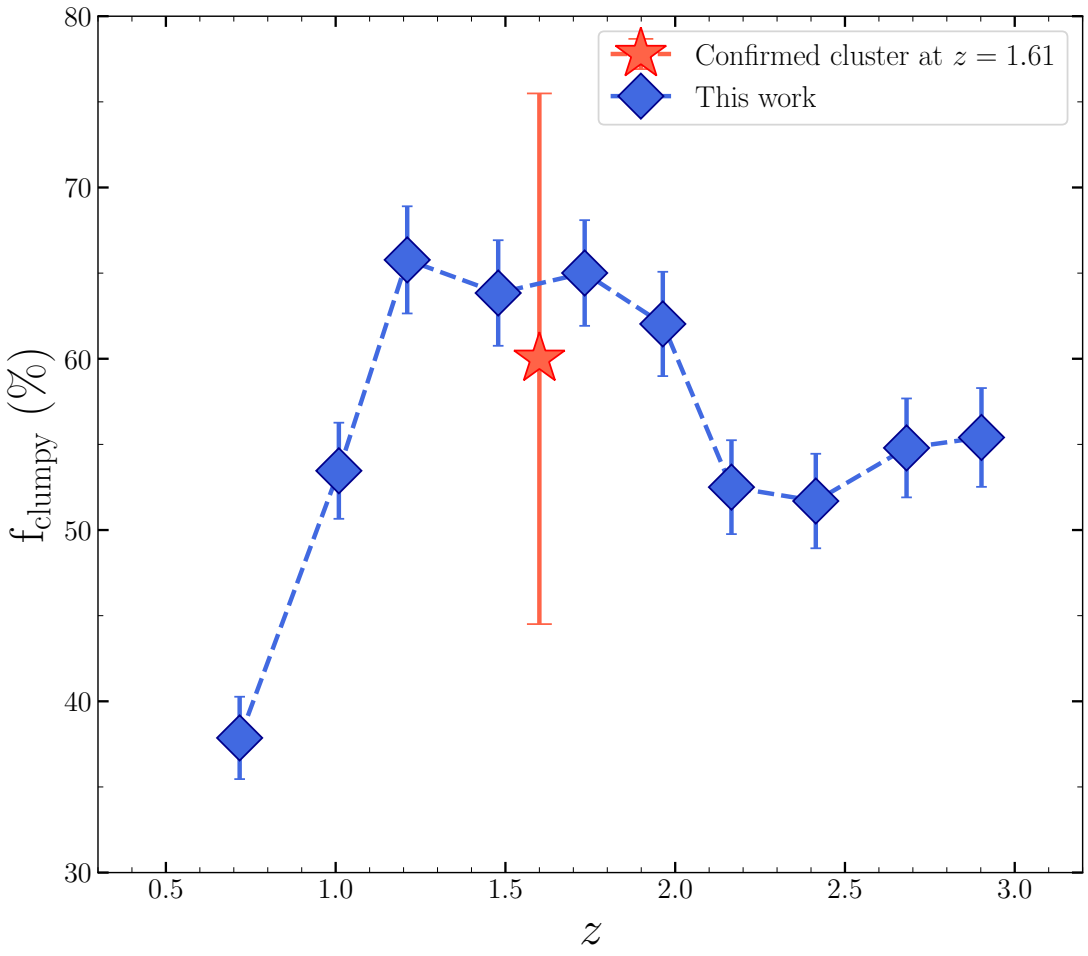


Figure 3.11: Same as Figure 3.7, but the fraction of clumpy galaxies for a confirmed cluster at $z = 1.61$ is also shown with a red star. The error bars are measured using Poisson statistics from the number counts of galaxies.

- We find that the fraction of clumpy galaxies peaks at redshifts $\sim 1-2$ ($f_{clumpy} \sim 65\%$), and decreases to $\sim 40\%$ at lower redshifts. Furthermore, the fraction of clumpy galaxies is almost redshift independent beyond $z \gtrsim 2$ with $f_{clumpy} \sim 50\%$.

- The fraction of clumpy galaxies decreases monotonically with an increase in stellar mass. The slope of this decline is steeper for galaxies at higher redshifts ($z > 1$).

- For the first time, we study the fraction of clumpy galaxies as a function of their local environment derived from accurate photometric redshifts out to $z = 3$. We find that $f_{clumpy}$ is independent of local environment of galaxies across the redshift range of this study ($0.5 \leq z \leq 3$). We also investigate the clumpy fraction for the members of a spectroscopically-confirmed cluster at $z = 1.61$. Out of 25 selected members of this cluster in the stellar mass range of our study, 15 are labeled as clumpy, resulting in the $f_{clumpy} = 60\%$ for this cluster. This result is consistent with our measurements of clumpy fraction in the field at the same redshift.

- Due to the lack of a significant correlation between the clumpy fraction and the local environment of galaxies, it appears that clump formation is facilitated by the fragmentation of gas clouds under VDI rather than being caused by incidents in the local environment of galaxies (e.g., mergers).

# Chapter 4

# Optical Spectroscopy of Dwarf Galaxies at $z \sim 0.15$ in the COSMOS Field: Insights into Metal Enrichment


## Abstract

We present a detailed analysis of the physical properties of low-mass galaxies (LMGs; $10^8 \leq M_*/M_\odot \leq 10^9$) at $z \sim 0.15$ in the COSMOS field, utilizing deep optical spectroscopy from the IMACS/Magellan telescope. We compare the properties of these LMGs with those of a similarly observed sample of intermediate-mass galaxies (IMGs; $10^9 \leq M_*/M_\odot \leq 10^{10}$). We find a consistent SFR-$M_*$ relation for both LMGs and IMGs, with slopes of 0.90±0.12 and 1.06±0.07, respectively. The Balmer decrement-based nebular attenuation increases with stellar mass, consistent across both samples. We also observe higher nebular-to-stellar attenuation ratios in LMGs compared to IMGs, suggesting different dust geometry within LMGs. Moreover, gas-phase metal-

licities are derived using N2 and O3N2 indicators, showing shallower MZR slopes for LMGs compared to IMGs. The existence of the FMR is also validated for both samples, revealing that higher gas-phase metallicity correlates with lower SFR at fixed stellar mass. Our measurements suggest that the intrinsic scatter in the MZR is larger for LMGs ($\sim$0.22 dex) than for IMGs ($\sim$0.15 dex), indicating more diverse star formation histories or environmental effects in LMGs. These findings provide insights into the chemical enrichment processes in dwarf galaxies, emphasizing the need for further studies on their star formation histories and environmental impacts.

## 4.1 Introduction

The hierarchical model of structure formation suggests that low-mass galaxies, also known as dwarfs (with stellar mass $M_* \lesssim 10^9 M_\odot$), are the fundamental building blocks of the universe and can provide important information about the formation history of the massive structures (White and Rees, 1978; Dekel and Silk, 1986). They are the most common type of galaxies in the universe, as evidenced by the low-mass end of the stellar mass function (e.g., Baldry et al., 2012). Despite their importance, dwarf galaxies have not been studied as extensively as their massive counterparts, mostly due to observational challenges. While the scaling relations between the physical parameters of massive galaxies are reasonably well understood, the situation is less clear for the dwarfs.

Investigating interconnected parameters in galaxies, such as the star formation rate (SFR), gas inflow and outflow, and metal enrichment of the interstellar medium (ISM), offers essential information about understanding the baryon recycling in galaxies. Dwarf galaxies are excellent laboratories for such studies, and analyzing those relations in low-mass galaxies pro-

vides crucial insights into the universality and evolution of different scaling relations. Due to their shallow potential wells, dwarf galaxies are more susceptible to feedback processes within their ISM, such as supernova explosions and stellar winds. These mechanisms can expel metal-enriched gas from the galaxies into the circumgalactic medium (CGM) and intergalactic medium (IGM). Because these processes are more prevalent in dwarf galaxies, they contribute significantly to metal enrichment in the CGM and IGM (Tremonti et al., 2004; Robertson et al., 2010; Peeples and Shankar, 2011; Lin et al., 2023).

One of the key scaling relations in galaxies that encapsulates the cumulative effects of star formation, metal production, and gas flows is the mass-metallicity relation (MZR). The MZR demonstrates that more massive galaxies have higher gas-phase metallicities (Tremonti et al., 2004; Kewley and Ellison, 2008; Mannucci et al., 2009; Sanders et al., 2015; Maiolino and Mannucci, 2019). Some studies have reported the existence of the MZR for low-mass galaxies with increased scatter in this mass range (Zahid et al., 2012; Guo et al., 2016). This large scatter, compared to their massive counterparts, can be attributed to several factors, including variations in star formation activity, enhanced sensitivity to environmental effects, and the efficiency of feedback processes in these galaxies (Berg et al., 2012; Jimmy et al., 2015).

For intermediate-mass ($10^9$ $M_\odot \lesssim M_* \lesssim 10^{10}$ $M_\odot$) and massive ($M_* > 10^{10} M_\odot$) galaxies, the fundamental metallicity relation (FMR, a relation between the stellar mass, metallicity, and SFR) further refines our understanding by incorporating the SFR as a third parameter, showing that at a fixed stellar mass, galaxies with higher SFRs tend to have lower gas-phase metallicities (Mannucci et al., 2010; Lara-López et al., 2010b; Yates et al., 2012; Sanders et al., 2018). FMR suggests that the inflow of pristine gas into the ISM, which fuels star

formation, increases the SFR in galaxies while simultaneously diluting the metal abundance in the ISM. Several studies have also validated the existence of FMR at the low-mass end, demonstrating its existence in dwarf galaxies (Bulichi et al., 2023; Gburek et al., 2023; Li et al., 2023; Curti et al., 2024).

The dust properties of galaxies offer additional insights into their evolutionary processes and ISM characteristics. The correlation between nebular and stellar dust attenuation reveals insights into the dust geometry within galaxies. Previous studies have demonstrated that nebular regions experience greater reddening compared to the stellar continuum in star-forming galaxies (Calzetti et al., 2000; Garn and Best, 2010; Kreckel et al., 2013; Kashino et al., 2013; Reddy et al., 2015; Qin et al., 2019; Chartab et al., 2024), confirming the two-component dust-star model, wherein all stars undergo moderate attenuation by diffuse ISM dust, while nebular lines from young, massive stars in HII regions are further attenuated by dusty birth clouds (Calzetti et al., 1994; Charlot and Fall, 2000). Furthermore, the correlation between nebular to stellar reddening and various galaxy properties such as stellar mass, SFR, specific star formation rate (sSFR; defined as SFR per stellar mass), and gas-phase metallicity has been explored in previous studies (Garn and Best, 2010; Reddy et al., 2015; Hemmati et al., 2015; Shivaei et al., 2020). However, these studies predominantly focus on massive galaxies, leaving the relationships between dust content and other galaxy properties less explored in low-mass systems.

In this paper, we analyze the physical properties obtained from rest-frame optical emission lines for a large sample of low-mass galaxies (hereafter LMGs) and compare them with those of a similarly observed sample of intermediate-mass galaxies (hereafter IMGs; Patel et al.,

2023). The paper is structured as follows. Section 4.2 describes the sample selection and observations for LMGs and IMGs. In Section 4.3, we detail the spectral energy distribution (SED) fitting procedure and the measurements of emission line fluxes for our spectra. In Section 4.4, we study the SFR and stellar mass relation for both samples, investigate their stellar and nebular dust content, examine the AGN contamination in our samples to have robust measurements of gas-phase metallicity, and construct the MZR for LMGs and IMGs. We discuss our results and summarize them in Section 4.5.

Throughout this paper, we assume a flat ΛCDM cosmology with $H_0 = 70\ \mathrm{kms^{-1}Mpc^{-1}}$, $\Omega_{m_0} = 0.3$, and $\Omega_{\Lambda_0} = 0.7$. All the physical parameters are measured assuming a Kroupa (2001) initial mass function (IMF).

## 4.2 Data

In this paper, we study a sample of LMGs in the Cosmic Evolution Survey (COSMOS; Scoville et al., 2007) field. Our galaxies are initially selected based on two criteria on their stellar mass and photometric redshift ($z_{phot}$):

1. $10^8 \leq \mathrm{M_*/M_\odot} \leq 10^9$;
2. $0.1 \leq z_{phot} \leq 0.2$.

Spectroscopy of these galaxies was acquired in 2019, 2023, and 2024. We discuss details of the observations in the next section. The galaxies observed in 2019 were selected from Muzzin et al. (2013c), with their $z_{phot}$ calculated using the EAZY code (Brammer et al., 2008) and their stellar

masses determined through the SED fitting code of FAST (Kriek et al., 2009). However, the more recent sample was selected from the CLASSIC catalog of COSMOS2020 (Weaver et al., 2022). The stellar mass and $z_{phot}$ of these sources are selected from a combination of EAZY (Brammer et al., 2008) and LePhare (Arnouts et al., 2002; Ilbert et al., 2006) solutions of SED fitting.

For all the sources initially selected from the two catalogs of Muzzin et al. (2013c) and Weaver et al. (2022) based on their stellar mass and $z_{phot}$, we then perform SED fitting by fixing their redshifts to the spectroscopic values to recalculate their physical properties (Section 4.3.1).

### 4.2.1 IMACS Observation

Deep optical spectroscopic observation of our galaxies is obtained using the Inamori-Magellan Areal Camera and Spectrograph (IMACS; Dressler et al., 2011) at the Magellan Baade telescope over the observing programs during 2019, 2023, and 2024. All 12 masks were observed under clear conditions with an average seeing of $\sim 0.6''$. The typical exposure time for each mask was $\sim$ 210 minutes.

$f/2$ spectroscopy with 300 mm$^{-1}$ grism dispenser and the spectroscopic filter is conducted for observing runs. The slit widths were $1'$, and the wide range of wavelength coverage (3700-9500 Å) allows the detection of strong emission lines, such as H$\alpha$ and H$\beta$, simultaneously.

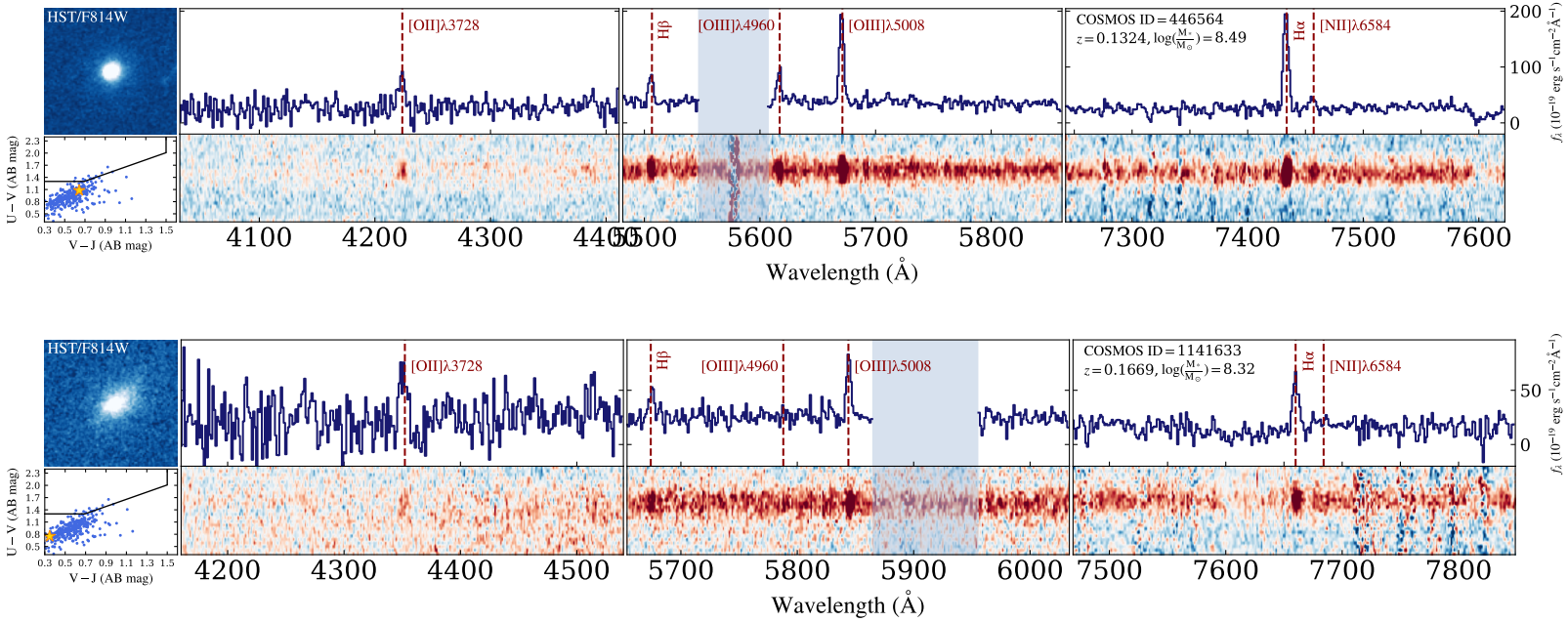


Figure 4.1: 1D and 2D spectra of four example LMGs observed with a ∼3-hour exposure using IMACS/Magellan. In each row, the UVJ diagram (bottom left) displays the entire sample of LMGs with the example galaxy marked (yellow star). The F814W/HST cutout of the galaxy is also shown in the top left.

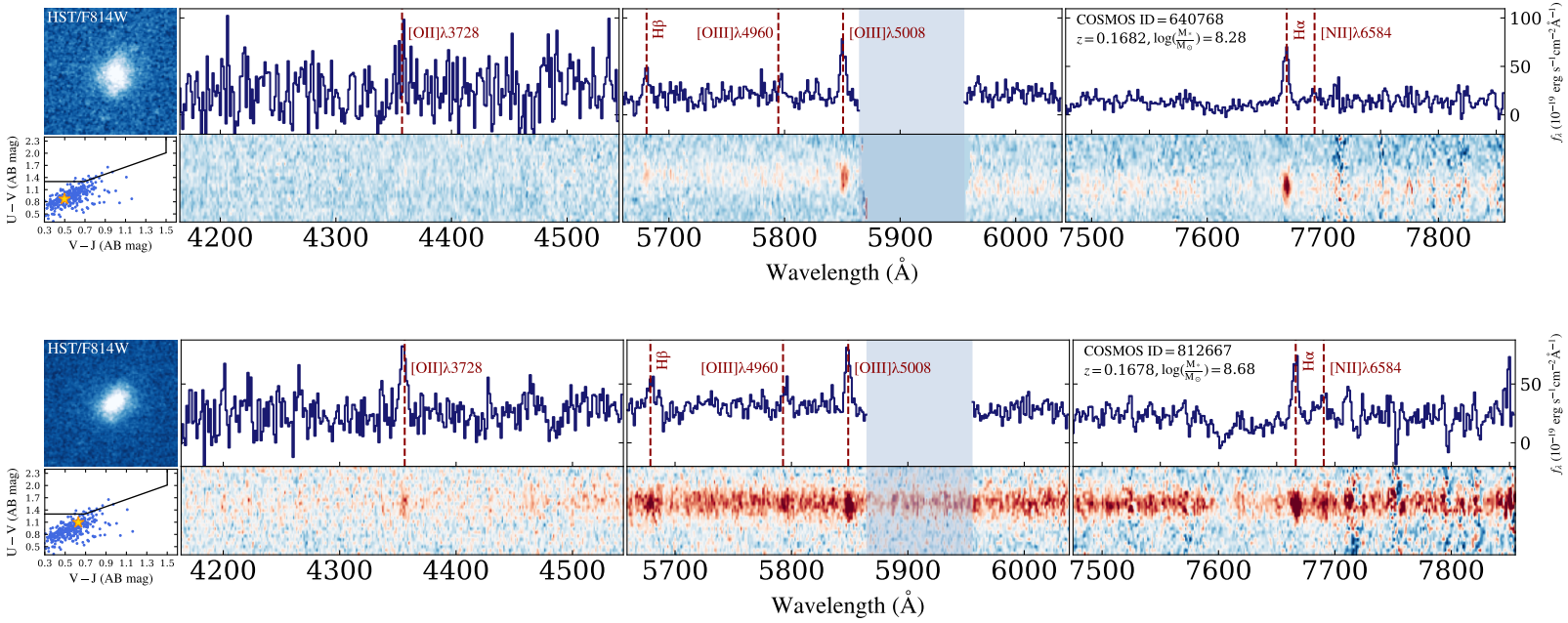


Figure 4.1: (Continued.)

### 4.2.2 Data Reduction

To reduce the spectroscopic data, we utilize the Carnegie Python Distribution (CarPy[1]), which is a powerful tool tailored for IMACS observations (see e.g., Kelson et al., 2000; Kelson, 2003). The pipeline stacks individual frames, subtracts the sky background, rectifies and extracts 2D spectra. Following this, we apply the optimal extraction algorithm to obtain 1D spectra of galaxies and associated errors (Horne, 1986). Spectroscopic redshifts of galaxies are determined based on strong emission lines in the galaxy spectra, such as H$\alpha$, [OIII]$\lambda$5008, and [OII]$\lambda$3727. Figure 4.1 displays both 2D and 1D spectra for selected LMGs, along with their positions on the UVJ diagram and their F814W/HST postage stamps.

### 4.2.3 Intermediate-Mass Control Sample

As a comparison, a similarly observed sample of IMGs is also added to our LMG sample. The details of the observation and sample selection of these galaxies are discussed extensively in Patel et al. (2023), but we provide a brief summary here. IMGs are initially selected from Muzzin et al. (2013c) based on their $z_{phot}$ and stellar mass, such that $10^9 \leq M_*/M_\odot \leq 10^{10}$, and $0.3 \leq z_{phot} \leq 0.4$. The stellar masses are the product of `FAST` SED fitting code (Kriek et al., 2009), and the photometric redshifts are measured with the `EAZY` code (Brammer et al., 2008). Magellan IMACS spectroscopy, along with the measurement of spectroscopic redshifts and emission line fluxes, is detailed in Patel et al. (2023). For a full description, we refer the reader to this work.

Figure 4.2 shows the spectroscopic redshift distribution for both LMG and IMG samples. Our main sample consists of 336 LMGs, represented by the green histogram, and 743 IMGs,

[1] `https://code.obs.carnegiescience.edu/`

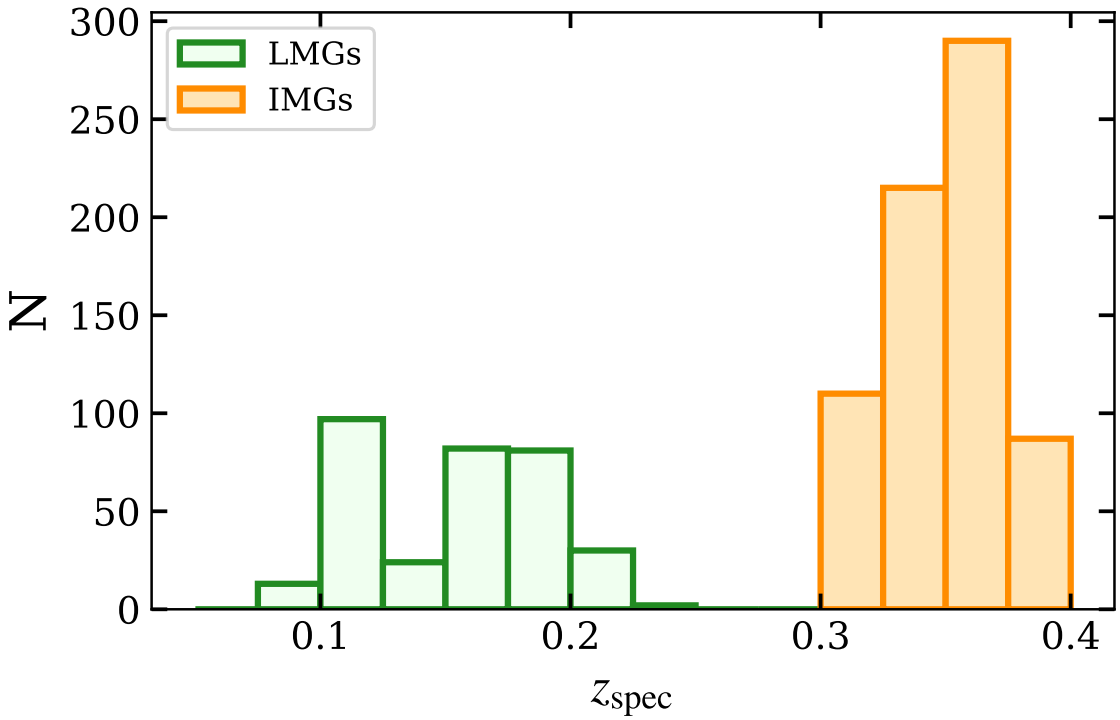


Figure 4.2: Spectroscopic redshift distribution of both LMGs and IMGs.

depicted by the orange histogram. The redshift ranges for these samples are $0.1 \lesssim z \lesssim 0.2$ for the LMGs and $0.3 \lesssim z \lesssim 0.4$ for the IMGs, respectively.

## 4.3 Analysis

### 4.3.1 SED Fitting

Utilizing the Bayesian Analysis of Galaxies for Physical Inference and Parameter ESti-mation (`Bagpipes`; Carnall et al., 2018)[2] framework, we fit the UV to mid-infrared SEDs of both LMGs and IMGs to derive their physical properties. The observed photometry for these galaxies

[2] `https://bagpipes.readthedocs.io/en/latest/`

is taken from the COSMOS2020 CLASSIC catalog (Weaver et al., 2022), which is corrected for galactic dust and rescaled to the total flux for the 3″ diameter aperture photometry.

Bagpipes employs the 2016 version of the Bruzual and Charlot (2003) stellar population synthesis (SPS) models. Additionally, the nebular emission modeling within the code utilizes the 2017 version of the Cloudy photoionization code (Ferland et al., 2017) based on the Byler et al. (2017) methodology.

In the process of SED fitting, we fix the redshifts to their spectroscopic values and adopt a delayed exponentially declining star formation history, $te^{-t/\tau}$. We set a uniform prior for the star formation e-folding time-scale ($\tau$) ranging from 0.3 to 10 Gyr. A Calzetti et al. (2000) dust model with $A_V = (0, 2)$ is applied. Additionally, we consider a metallicity range from $0 < Z/Z_\odot < 2.5$ with a logarithmic prior.

The best-fit SED model for each galaxy, along with stellar masses and other physical parameters (e.g., SFR and stellar dust attenuation), is obtained from SED fitting. The rest-frame UVJ colors are also measured for both LMGs and IMGs. In Figure 4.3, we demonstrate the position of our galaxies on the rest-frame UVJ plane. The green line in the figure separates the population of quiescent galaxies from the star-forming ones, following the definition from Muzzin et al. (2013a). The bold red (blue) data points correspond to LMGs (IMGs) with $3\sigma$ detection in their H$\alpha$ and H$\beta$ lines used in the present work. As shown in the figure, most of our LMGs and IMGs are in the star-forming region, with a few of them ($\sim$ 1% of LMGs and $\sim$ 2% of IMGs) in the quiescent region.

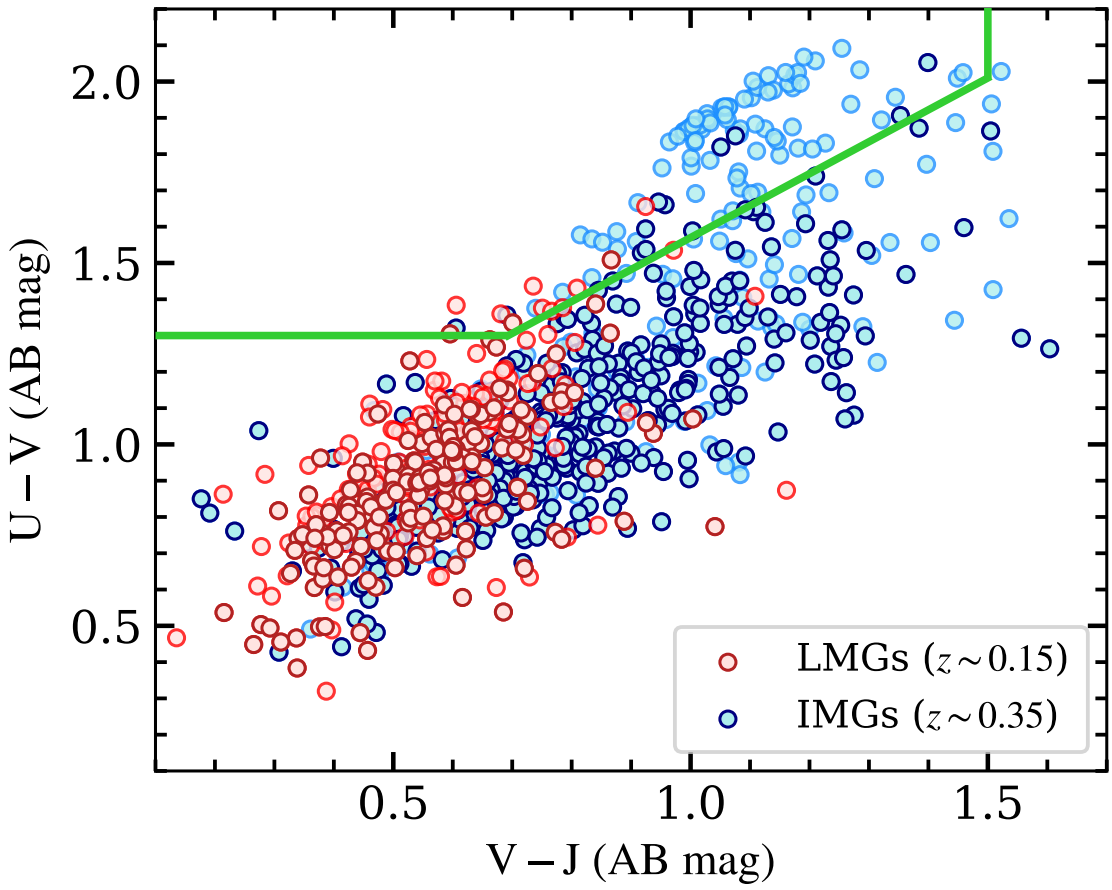


Figure 4.3: The rest-frame UVJ plane derived from SED fitting for both LMGs (red) and IMGs (blue). The bold red (blue) data points correspond to LMGs (IMGs) with $3\sigma$ detection in their H$\alpha$ and H$\beta$ lines. The green line indicates the boundary between quiescent galaxies and star-forming galaxies.

### 4.3.2 Emission Line Measurements

Given the wide wavelength coverage of IMACS, we measure the emission line fluxes in three wavelength ranges with strong emission lines:

1. [OII]$\lambda\lambda$3727, 3730;
2. H$\beta$, [OIII]$\lambda\lambda$4960, 5008;
3. H$\alpha$, [NII] $\lambda\lambda$6550, 6585.

In each wavelength range, we simultaneously fit multiple Gaussians to the 1D spectra of galaxies to extract the desired emission line fluxes. The fluxes of H$\alpha$ and H$\beta$ emission lines are corrected for underlying Balmer absorption using the best-fit SED models obtained in Section 4.3.1. We measure the line fluxes by integrating the best-fit Gaussian function over the 1D spectrum. The errors of the line fluxes are also calculated from the standard deviation of the best-fit Gaussian functions.

## 4.4 Results

### 4.4.1 SFR-$M_*$ Relation

Out of 336 (743) LMGs (IMGs) at $z \sim 0.15$ ($z \sim 0.35$), 176 (460) of them have signal-to-noise (S/N) $\geq$ 3 detection in their H$\alpha$ and H$\beta$ emission lines (these galaxies are shown with bold colors on the UVJ diagram presented in Figure 4.3). We derive the H$\alpha$-based SFRs ($SFR_{H\alpha}$) for our LMG and IMG samples using the Kennicutt (1998) calibration, assuming the

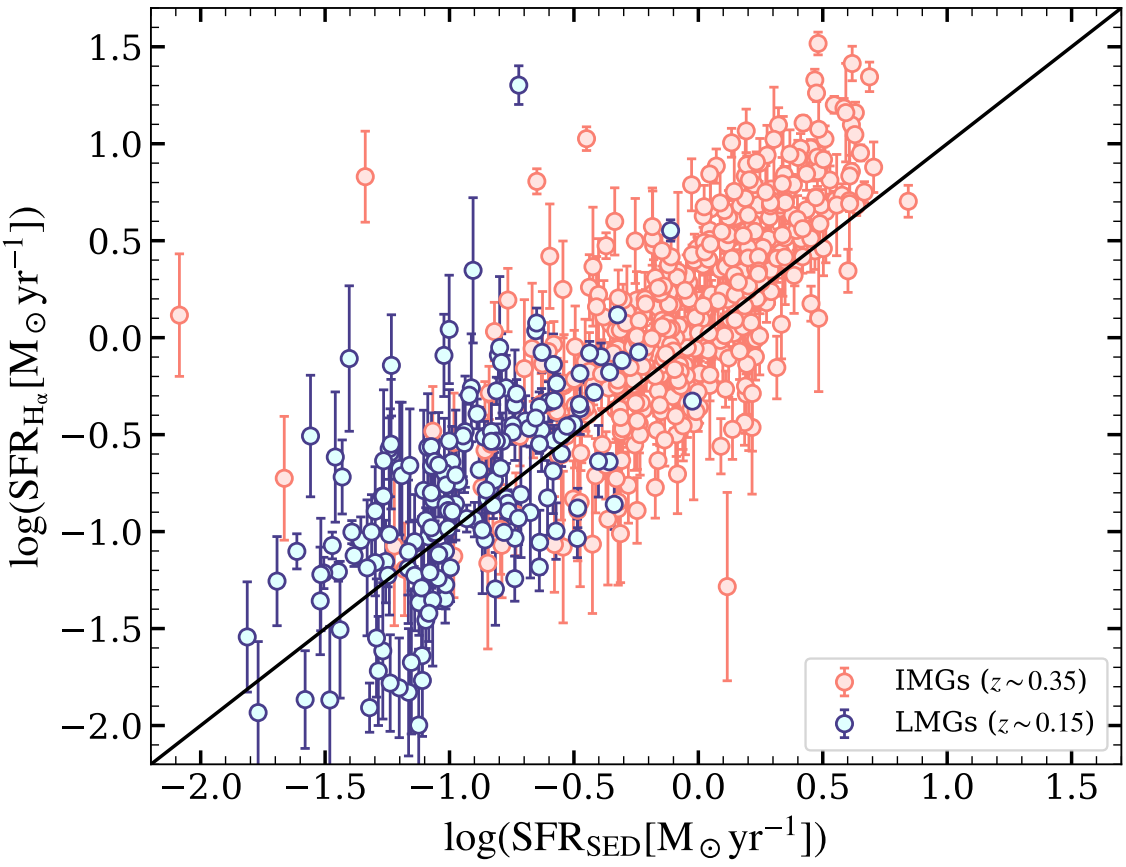


Figure 4.4: Comparison between the SFRs estimated from SED fitting ($SFR_{SED}$) with those based on the H$\alpha$ luminosity ($SFR_{H\alpha}$) for LMGs (blue circles) and IMGs (pink circles). The black line represents a unit slope, indicating equality between $SFR_{H\alpha}$ and $SFR_{SED}$.

Kroupa (2001) IMF: $SFR_{H\alpha}(M_\odot yr^{-1}) = 5.5\times10^{-42}\, L_{H\alpha}(erg/s)$. SFRs are calculated by correcting the H$\alpha$ luminosities for attenuation using the Balmer decrement (elaborated in Section 4.4.2). The uncertainties associated with $SFR_{H\alpha}$ include the $E(B-V)_{nebular}$ uncertainties as well as the measurement errors of the line fluxes.

Another measurement of SFR is also obtained from SED fitting ($SFR_{SED}$). While the SFR derived from H$\alpha$ flux measurements traces the instantaneous star formation activity within galaxies, the SED-derived SFR represents the integrated SFR of the galaxy over 100 Myrs and is

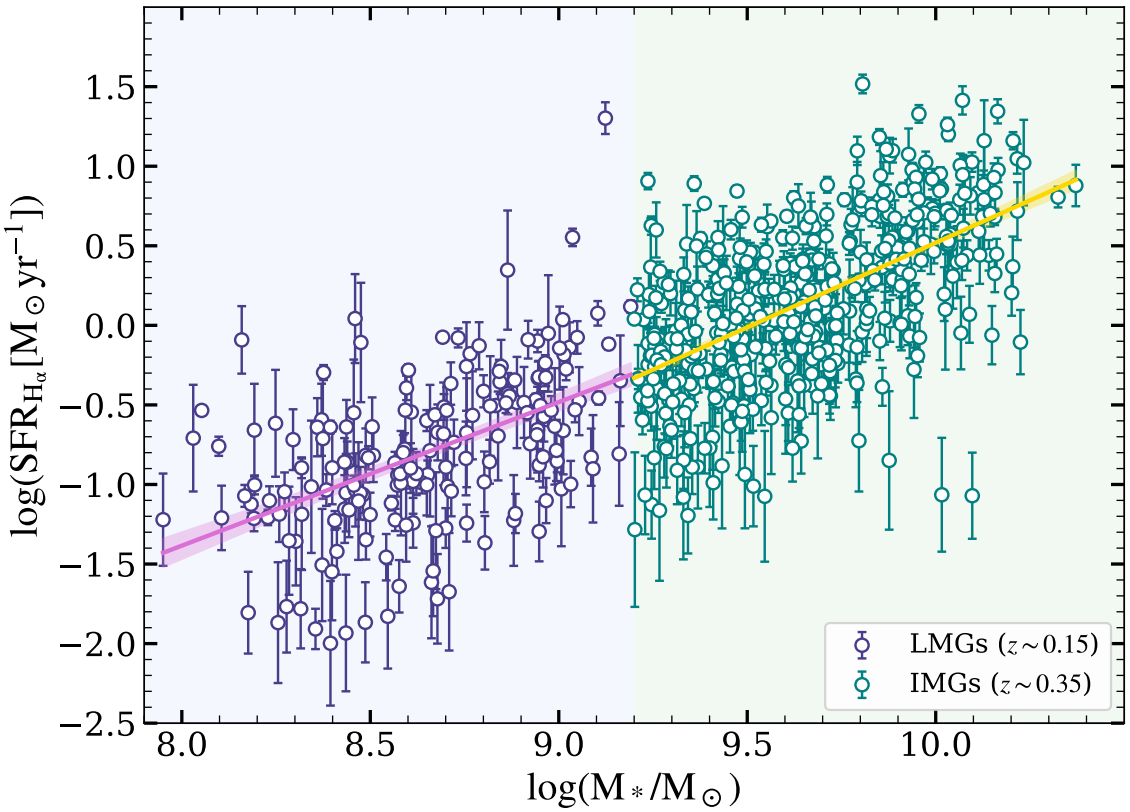


Figure 4.5: $SFR_{H\alpha}$ as a function of stellar mass for LMGs (purple circles) and IMGs (teal circles). The purple (yellow) line represents the best-fit to the data points in the LMG (IMG) sample. The shaded region around each line shows the uncertainty of the fitted line.

more susceptible to degeneracies present in SED modeling. These degeneracies can arise from factors such as age, metallicity, dust attenuation, and assumptions about the IMF, making the interpretation of $SFR_{SED}$ more complex. Nevertheless, we compare these two measurements in Figure 4.4 and find that they are relatively in agreement. The normalized median absolute deviation ($\sigma_{NMAD}$) is $\sim$ 0.3 for each sample, which is in agreement with measurements from Patel et al. (2023) for IMGs.

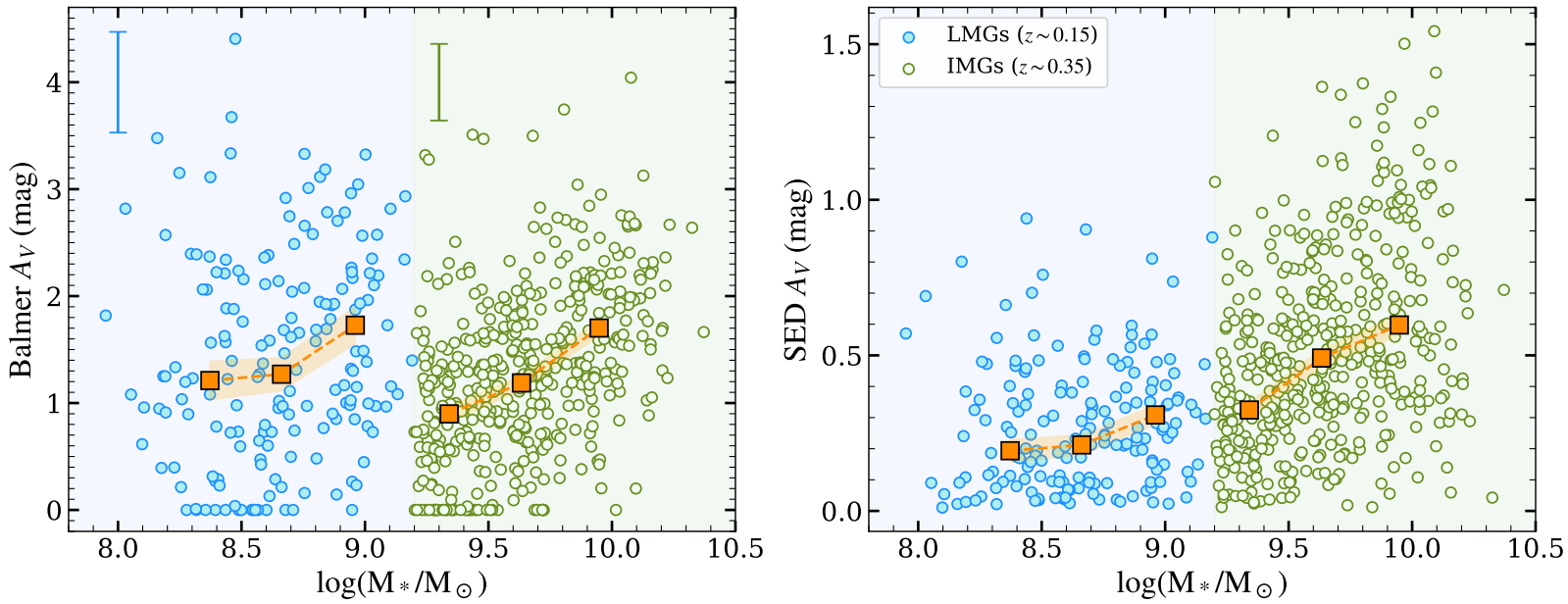


Figure 4.6: Left: Balmer $A_V$ plotted against stellar mass for LMGs (blue circles) and IMGs (green circles). Orange squares indicate the median trend within each sample. The typical error bar of each sample is displayed in the top-left corner. Right: SED-derived $A_V$ versus stellar mass for LMGs (blue circles) and IMGs (green circles), with the median trend shown as orange squares across different stellar mass bins. The shaded regions around the median values in each panel indicate the uncertainty associated with these medians.

Additionally, we present the $SFR_{H\alpha}$ as a function of stellar mass for our galaxies in Figure 4.5. As shown in the figure, the SFR increases with the increase of stellar mass in all mass ranges, indicating the common star formation main sequence trend of galaxies (e.g., Speagle et al., 2014). We estimate the intrinsic scatter in SFRs using $\sigma^2_{\rm obs} = \sigma^2_{\rm meas} + \sigma^2_{\rm int}$. For both LMGs and IMGs, $\sigma_{\rm int}$ is similar and $\sim 0.4$. We also show the best-fit line along with its uncertainty for each sample separately. The slope of the best-fit line for LMGs is $0.90 \pm 0.12$, similar to that of IMGs ($1.06 \pm 0.07$). This slope is in agreement with previous studies of SFR-$M_*$ relation (e.g., Salim et al., 2007; Peng et al., 2010; Kelson, 2014; Whitaker et al., 2014).

### 4.4.2 Dust Attenuation

We estimate the nebular dust attenuation for LMGs and IMGs using the Balmer decrement (H$\alpha$/H$\beta$ line flux ratio). The intrinsic ratio of 2.86 is considered for H$\alpha$/H$\beta$, assuming standard case B recombination at $T = 10^4$ K and an electron density of $n_e = 10^2$ cm$^{-3}$ (Osterbrock and Ferland, 2006). To convert the color excess to attenuation ($A_\lambda = k_\lambda E(B-V)$), we employ the Calzetti et al. (2000) attenuation law for estimating the reddening curve ($k_\lambda$). Attenuation uncertainty is also calculated using the H$\alpha$ and H$\beta$ flux errors and standard error propagation methods.

The left panel of Figure 4.6 shows the Balmer visual band attenuation (Balmer $A_V$) as a function of stellar mass for LMGs and IMGs. The running median of $A_V$ in bins of stellar mass is also shown with orange squares. For both LMGs and IMGs, the median nebular attenuation increases with stellar mass. This correlation has been found in previous studies for local and high redshift galaxies (e.g., Garn and Best, 2010; Cullen et al., 2018). The left panel also demonstrates that the median Balmer $A_V$ values are consistently high across all mass bins for

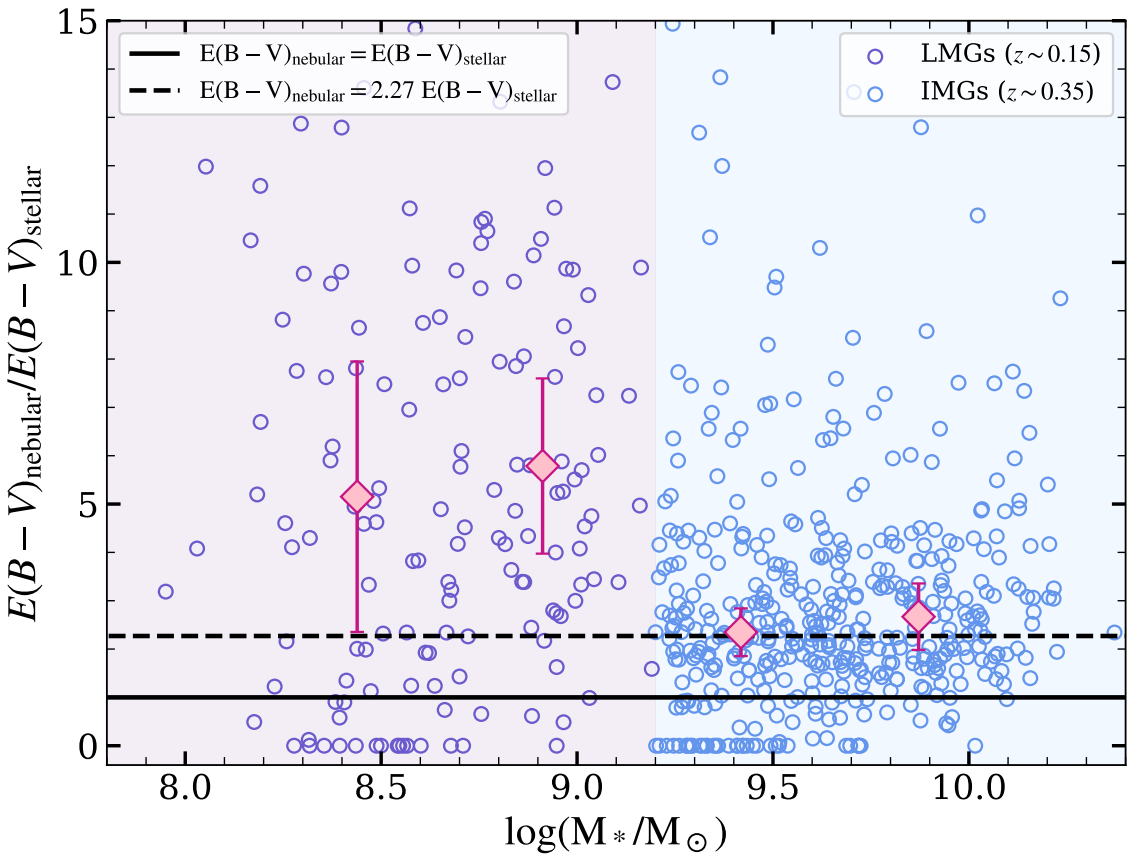


Figure 4.7: Variation of nebular to stellar color excess with stellar mass for LMGs (purple circles) and IMGs (blue circles). Median values for each sample are represented in two stellar mass bins using pink diamonds. Error bars indicate the uncertainty of these medians. The solid line denotes equal nebular and stellar color excess, while the dashed line shows the $E(B-V)_{\rm nebular} = 2.27\ E(B-V)_{\rm stellar}$ relation by Calzetti et al. (2000).

LMGs, comparable to those observed in IMGs. This may stem from the different redshift ranges probed by each sample. However, it has been demonstrated that the correlation between nebular attenuation and stellar mass remains the same across all redshift ranges, showing no evolution with redshift (Shapley et al., 2022).

In the right panel of Figure 4.6, we display the relationship between visual band stellar dust attenuation (SED $A_V$) and stellar mass for LMGs and IMGs. The median values across

different stellar mass bins are depicted using orange squares. As illustrated in this panel, SED $A_V$ increases with stellar mass in both LMGs and IMGs; however, the increase is more pronounced for IMGs, exhibiting a steeper slope. Additionally, we observe an excess of nebular attenuation compared to that of the stellar continuum for both LMGs and IMGs, as found in various previous studies (e.g., Calzetti et al., 2000; Garn and Best, 2010; Hemmati et al., 2015; Qin et al., 2019; Shivaei et al., 2020; Patel et al., 2023; Chartab et al., 2024). For our IMG sample, the results of these analyses have also been detailed in Patel et al. (2023). Our measurements align closely with those reported in their study.

To further investigate the high nebular to stellar attenuation in LMGs, we plot the nebular to stellar color excess as a function of stellar mass in Figure 4.7. The median values in two bins of stellar mass for each sample of galaxies are also shown with pink diamonds. The solid line shows the case of no extra attenuation toward nebular regions, and the dashed line shows $E(B-V)_{\rm nebular}/E(B-V)_{\rm stellar} = 2.27$ from Calzetti et al. (2000). For IMGs, the median values closely follow this dashed line, while LMGs display $E(B-V)_{\rm nebular}/E(B-V)_{\rm stellar} \sim 5$. Comparing LMGs and IMGs, it is evident that the median reddening ratio for LMGs is higher, yet the difference remains within the error margin, $\sim 1\sigma$ greater than that of IMGs. But within each sample, there is no significant correlation between the reddening ratio and stellar mass, which is consistent with previous studies for more massive galaxies (e.g., Hemmati et al., 2015; Reddy et al., 2015; Shivaei et al., 2020).

We also show the nebular to stellar color excess as a function of sSFR in Figure 4.8. The sSFR is derived from the dust-corrected H$\alpha$ SFR ($\rm SFR_{H\alpha}$), as detailed in Section 4.4.1. solid and dashed lines in the figure show a 1 : 1 ratio of nebular and stellar color excess and the relation

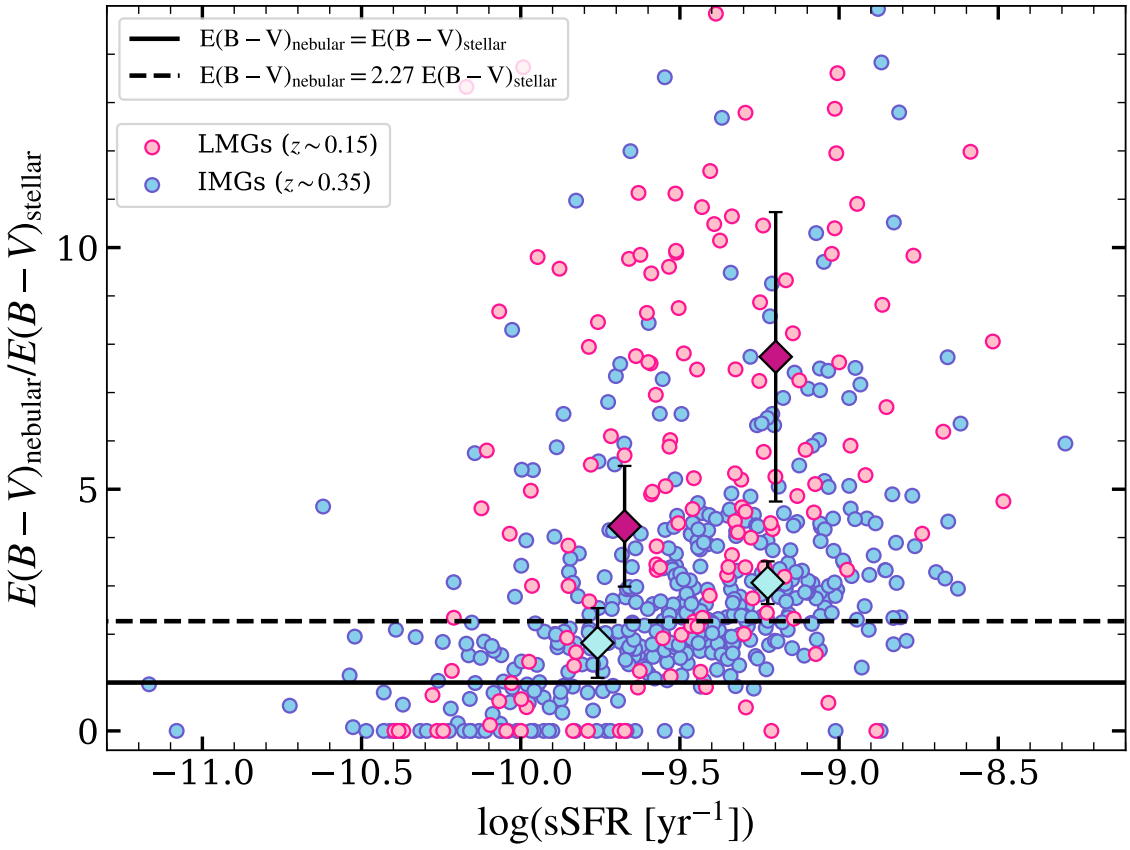


Figure 4.8: Nebular to stellar color excess as a function of sSFR for LMGs (pink circles) and IMGs (blue circles). Median values, along with their uncertainties, are depicted with magenta (blue) diamonds for the LMG (IMG) sample in two bins of sSFR. The solid line shows identical nebular and stellar color excess, and the dashed line indicates the relation between the two reddening from Calzetti et al. (2000) ($E(B-V)_{\rm nebular} = 2.27\ E(B-V)_{\rm stellar}$).

from Calzetti et al. (2000), respectively. The median values of the reddening ratio, along with the errors associated with them, are shown with magenta (blue) diamonds for LMGs (IMGs) in bins of sSFR. Despite large uncertainties, for both samples, the reddening ratio seems to increase with the increase of sSFR, in agreement with previous works for high redshift galaxies (Reddy et al., 2015). This supports the idea that the dust distribution in LMGs is not uniform, with denser dust regions corresponding to areas of intense star formation.

### 4.4.3 AGN Contamination

The presence of active galactic nuclei (AGNs) prevents the robust measurements of gas-phase metallicity from rest-optical emission lines (e.g., Chartab et al., 2022) and hence, we locate our galaxies in two diagnostic plots to see the contamination from AGNs in our samples. Figure 4.9 shows the stellar mass-excitation (MEx) diagnostic diagram (left panel) and the BPT diagram (right panel) for our LMG and IMG samples with $3\sigma$ detection in their [OIII]$\lambda$5008 emission line (in the left panel), and [OIII]$\lambda$5008 and [NII] $\lambda$6585 emission lines (in the right panel) in addition to their H$\alpha$ and H$\beta$ line detection.

Galaxies above the dashed line in the left panel of Figure 4.9 are expected to be AGNs (Juneau et al., 2014), whereas galaxies between the two curves are "composite" sources whose line ratios are influenced by both star formation and AGN activity. Below the demarcation lines is the region where star-forming galaxies are located. We note that Juneau et al. (2014) found these empirically determined demarcation lines based on a sample at $0.04 < z < 0.2$ from SDSS DR7 (Abazajian et al., 2009). For higher redshifts ($z > 0.3$), they predicted a shift in these divisions to higher stellar masses. However, LMGs and IMGs fall within a similar redshift

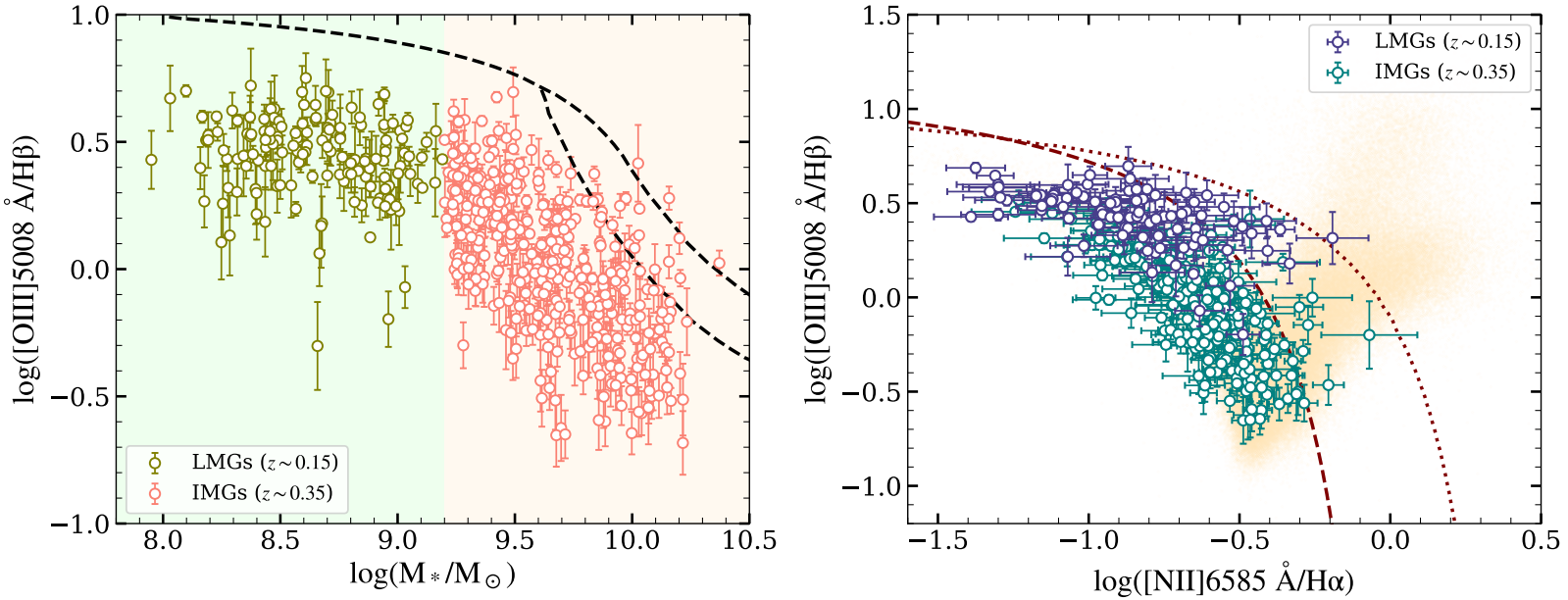


Figure 4.9: Left: The MEx diagnostic diagram for LMGs (green circles) and IMGs (pink circles) with $3\sigma$ detection in their [OIII]$\lambda$5008 line in addition to their H$\alpha$ and H$\beta$ detection. The dashed demarcation lines show the suggested divisions between star-forming galaxies, composite galaxies, and AGNs from Juneau et al. (2014) for SDSS galaxies. Right: The BPT diagram for LMGs (purple circles) and IMGs (teal circles) with $3\sigma$ detection in all four lines used in this diagnostic plot. The background beige data points indicate the BPT diagram of the SDSS sample from Kauffmann et al. (2003). The dashed and dotted maroon lines represent the $z \sim 0$ demarcations between star-forming galaxies (below the lines) and AGNs (above the lines) from Kauffmann et al. (2003) and Kewley et al. (2001), respectively.

range to the SDSS sample, allowing us to apply these boundaries in our MEx diagram. Notably, all LMGs (100%) and the majority of IMGs (approximately 93%) are located within the star-forming region, with minimal AGN contamination.

On the right panel of Figure 4.9, we locate our galaxies on the [OIII]$\lambda$5008/H$\beta$ versus [NII]$\lambda$6585/H$\alpha$ BPT diagram (Baldwin et al., 1981; Veilleux and Osterbrock, 1987). For comparison, the distribution of SDSS galaxies from Kauffmann et al. (2003) with 3$\sigma$ detection in their four lines of H$\alpha$, H$\beta$, [OIII]$\lambda$5008, and [NII] $\lambda$6585 is also shown in the background of the BPT diagram. Two maroon lines on the diagram, dashed representing Kauffmann et al. (2003) and dotted representing Kewley et al. (2001), demarcate star-forming galaxies (below the lines) and AGNs (above the lines) empirically and theoretically, respectively.

As shown in this diagnostic diagram, the majority of our LMGs and IMGs are positioned within the star-forming region. Only a small fraction ($\sim$14% of LMGs and $\sim$3% of IMGs) fall between the two curves, identifying them as composite galaxies. These galaxies are not excluded from our gas-phase metallicity measurements since they still reside within the star-forming region of the BPT diagram, based on the division by Kewley et al. (2001).

### 4.4.4 Mass-Metallicity Relation

Observations of rest-optical emission lines for our samples of LMGs and IMGs allow us to measure the gas-phase metallicity of these galaxies using different line ratios. In this section, we use N2 ($\frac{[\mathrm{NII}]\lambda6585}{\mathrm{H}\alpha}$) and O3N2 ($\frac{[\mathrm{OIII}]\lambda5008/\mathrm{H}\beta}{[\mathrm{NII}]\lambda6585/\mathrm{H}\alpha}$) line ratios to estimate the gas-phase metallicity of galaxies.

We measure the gas-phase oxygen abundance (12+log(O/H)) of LMGs and IMGs that have S/N $\geq$ 3 in their H$\alpha$ and H$\beta$ emission lines, using the empirical calibration based on local

HII regions from Pettini and Pagel (2004). For each indicator, the conversion to the oxygen abundance is given by:

$$12 + \log(\mathrm{O/H}) = 8.9 + 0.57 \log(\mathrm{N2}), \tag{4.1}$$

and

$$12 + \log(\mathrm{O/H}) = 8.73 - 0.32 \log(\mathrm{O3N2}). \tag{4.2}$$

When utilizing the N2 indicator, we require galaxies to have $3\sigma$ detection in their [NII] $\lambda$6585 line as well. To include galaxies with undetected (S/N $< 3$) [NII] $\lambda$6585 lines in the MZR of our LMGs and IMGs, we stack the spectra in bins of stellar mass. The mass bins are selected such that each bin includes approximately the same number of galaxies.

To construct the composite spectra within each stellar mass bin, we first shift each spectrum to its rest-frame and correct it for reddening by applying a dust correction based on each galaxy's Balmer decrement (Section 4.4.2). We then normalize the spectrum by its H$\alpha$ luminosity. Through normalization, galaxies with high SFR do not dominate the composite spectrum. The H$\alpha$-normalized spectra are then interpolated at a resolution of 0.5 Å. The stellar mass and gas-phase metallicity of stacks are calculated from the median stellar mass and oxygen abundance of individual galaxies within each bin.

To assess the uncertainty of the composite spectra, we employ bootstrap resampling by randomly selecting galaxies from the initial sample with replacement. This process is repeated 1000 times, and the standard deviation of these trials is calculated to determine the uncertainty of the stack.

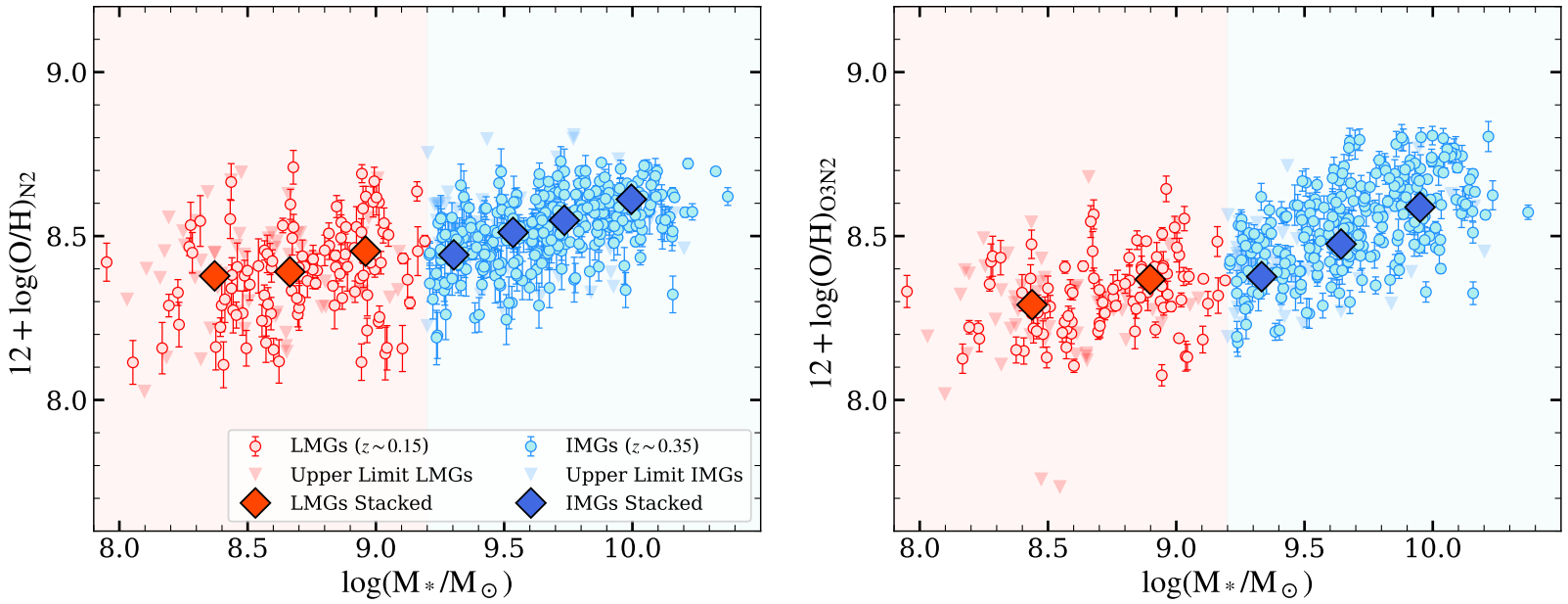


Figure 4.10: MZR for LMGs and IMGs, with metallicities derived using the N2 indicator (left panel) and O3N2 indicator (right panel). In each panel, LMGs are represented by red circles and IMGs by blue circles. $3\sigma$ upper limits for galaxies with undetected [NII] $\lambda$6585 line are indicated by inverted triangles. Diamond symbols denote gas-phase metallicity measurements from stacked spectra in bins of stellar mass. Error bars for the stacks, when not visible, are smaller than the corresponding symbols.

The left panel of Figure 4.10 presents the MZR for our samples of LMGs and IMGs, where the gas-phase oxygen abundance of galaxies is calculated using the N2 indicator. The metallicity measurement for stacked spectra is shown with red and blue diamonds in stellar mass bins for LMGs and IMGs, respectively. The equation for the best-fit line to the stacked values is given by:

$$12 + \log(\mathrm{O/H})_{\mathrm{N2}} = (0.13 \pm 0.09) \log\Big(\frac{\mathrm{M}_*}{10^8\ \mathrm{M}_\odot}\Big) + (8.32 \pm 0.07). \tag{4.3}$$

for LMGs, and

$$12 + \log(\mathrm{O/H})_{\mathrm{N2}} = (0.24 \pm 0.04) \log\Big(\frac{\mathrm{M}_*}{10^9\ \mathrm{M}_\odot}\Big) + (8.37 \pm 0.03). \tag{4.4}$$

for IMGs. The slope of the best fit to the MZR of LMGs is inconsistent with that of massive counterparts (i.e., IMGs) by $\sim 1.4\sigma$, such that the slope is steeper for IMGs.

Moreover, the intrinsic scatter for metallicity calibration based on the N2 ratio is 0.18 dex (Pettini and Pagel, 2004). A composite spectrum in each stellar mass bin consists of N galaxies (N = 58 for LMGs and N = 87 for IMGs); thus, the calibration error in the oxygen abundance of the composite spectra is $0.18/\sqrt{\mathrm{N}} \sim 0.02$ (Erb et al., 2006; Sanders et al., 2015). By adding the calibration error to the measurement uncertainties in quadrature and recalculating the best-fit lines, the inconsistency in the slope of IMGs and LMGs is reduced to $0.2\sigma$.

The intrinsic scatter for the O3N2 calibration is 0.14 dex, which is smaller than that of the N2 calibration, indicating a more precise measurement. Hence, it is useful to investigate the MZR using the O3N2 indicator as well.

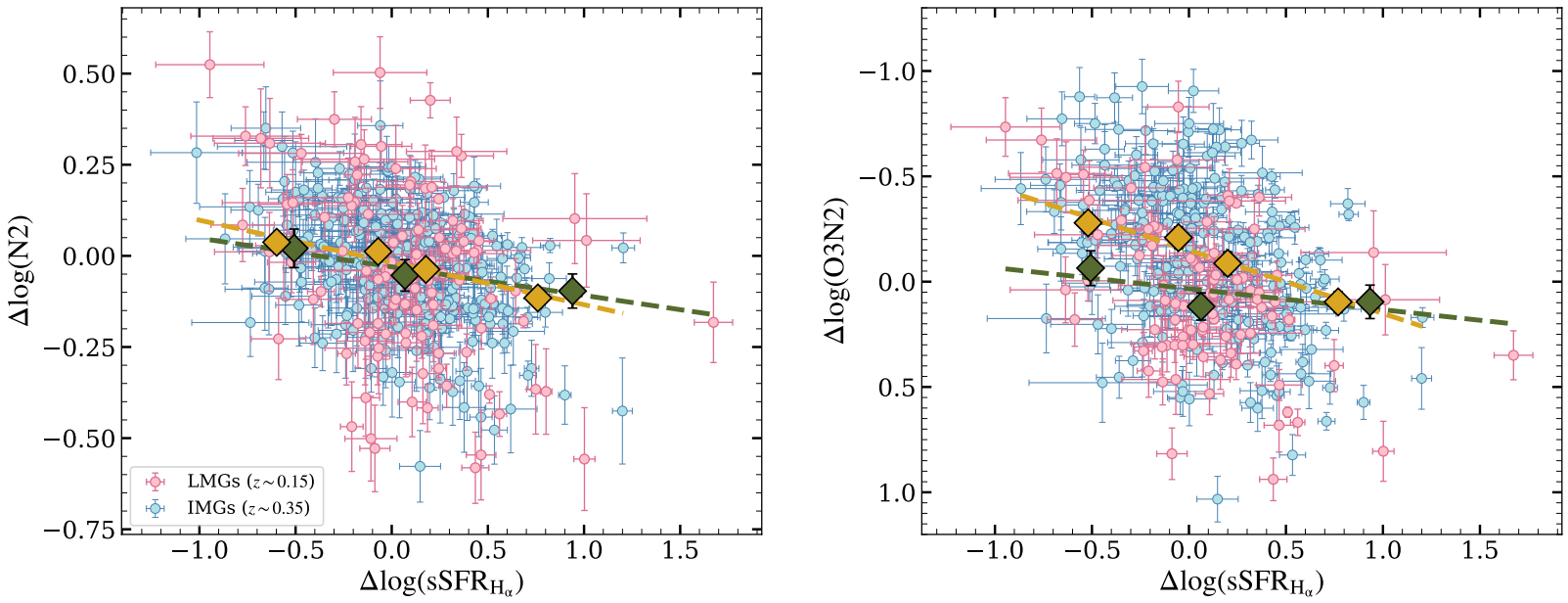


Figure 4.11: Residuals in the line ratio of galaxies (left: N2 line ratio, right: O3N2 line ratio) relative to the median line ratio, plotted against residuals in their sSFR relative to the best-fit line to the sSFR-$M_*$ relation. In each panel, pink circles represent LMGs, while the blue ones show IMGs. The green (yellow) diamonds and dashed line show the median values in $\Delta\log(sSFR_{H\alpha})$ bins and the best fit to the medians for LMGs (IMGs), respectively.

The right panel of Figure 4.10 also presents the MZR for LMGs and IMGs but with metallicities derived from the O3N2 line ratio. The symbols are the same as in the left panel, where the diamonds show the MZR of composite spectra in stellar mass bins. The best-fit line for the stacked values of LMGs is:

$$12 + \log(\mathrm{O/H})_{\mathrm{O3N2}} = (0.17 \pm 0.08) \log\Big(\frac{\mathrm{M}_*}{10^8\ \mathrm{M}_\odot}\Big) + (8.22 \pm 0.06). \tag{4.5}$$

and for that of IMGs is:

$$12 + \log(\mathrm{O/H})_{\mathrm{O3N2}} = (0.34 \pm 0.04) \log\Big(\frac{\mathrm{M}_*}{10^9\ \mathrm{M}_\odot}\Big) + (8.26 \pm 0.03). \tag{4.6}$$

As in the left panel, the slope of the best fit to the MZR in the right panel is also inconsistent between the two samples by $\sim 2.7\sigma$, and it is steeper for IMGs. Taking into account the intrinsic scatter of the O3N2 calibration for oxygen abundance and the number of galaxies in each mass bin (N = 76 for LMGs and N = 103 for IMGs), we expect the inconsistency in the slope to be reduced to $\sim 1.9\sigma$.

Consequently, we find that the LMG and IMG samples exhibit similar trends in their MZR when the metallicities are measured with the N2 indicator. However, the slope of the MZR is shallower for LMGs compared to that of IMGs when the gas-phase oxygen abundance is measured using the O3N2 indicator. The insignificant difference between the slope of the MZR for LMGs and IMGs, when relying on the N2 line ratio, can be a result of larger intrinsic uncertainty in the N2 calibration.

Utilizing our measurements of gas-phase metallicity and SFR, we investigate the existence of FMR within our sample of LMGs and IMGs. This involves examining the correlation between stellar mass, gas-phase metallicity, and SFR. Specifically, we plot deviations in galaxies' line ratio from the median line ratio (best fit to the stacked data) against deviations in their sSFR from the best-fit line to the sSFR-$M_*$ relationship in Figure 4.11. The left panel shows the N2 line ratio residuals, while the right panel illustrates the residuals of the O3N2 line ratio.

In both panels of Figure 4.11, the median values in bins of $\Delta\log(\mathrm{sSFR}_{\mathrm{H}\alpha})$ along with the best-fit lines to the medians for LMGs (shown in green diamonds and dashed lines) and IMGs (shown in yellow diamonds and dashed lines) are displayed. In the left panel, the best-fit slopes are $-0.08 \pm 0.02$ for LMGs and $-0.12 \pm 0.02$ for IMGs. In the right panel, these slopes are $0.10 \pm 0.09$ for LMGs and $0.3 \pm 0.04$ for IMGs.

Both LMGs and IMGs exhibit a similar distribution in the FMR plane, indicating a correlation between stellar mass, gas-phase metallicity, and SFR. At fixed stellar mass, galaxies with higher gas-phase metallicity have lower SFR.

Additionally, we show the deviations in line ratios of LMGs and IMGs from the median line ratio versus stellar mass in Figure 4.12. The left panel shows these residuals for the N2 line ratio, while the right panel displays that of the O3N2 line ratio. As shown in the figure, LMGs exhibit a larger scatter in the line ratio residuals compared to IMGs. This is evident from the shaded regions around the data points, with the red-shaded region representing LMGs and the green-shaded region representing IMGs. By accounting for the measurement scatter for each galaxy, we estimate the intrinsic scatter in the line ratio residuals using $\sigma^2_{\mathrm{obs}} = \sigma^2_{\mathrm{meas}} + \sigma^2_{\mathrm{int}}$.

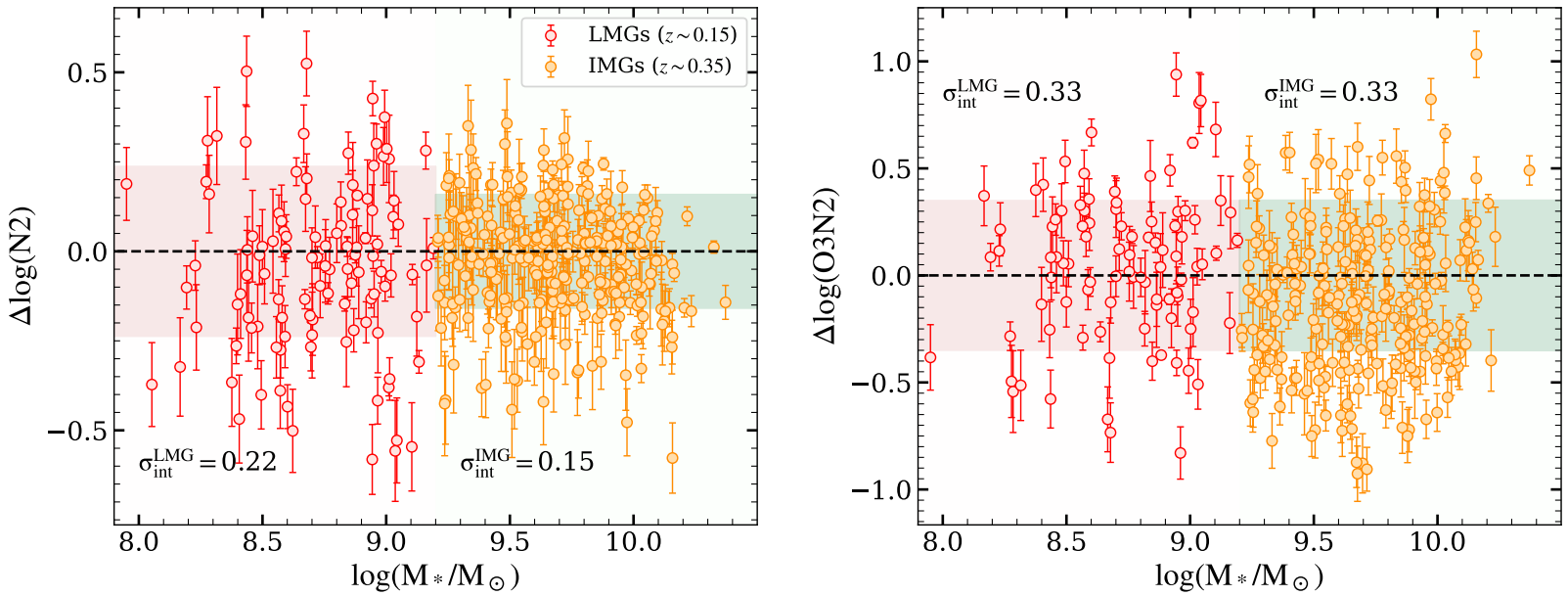


Figure 4.12: Residuals in the line ratio of galaxies relative to the median line ratio as a function of stellar mass, using the N2 line ratio (left panel) and the O3N2 line ratio (right panel). In each panel, red and orange circles represent LMGs and IMGs, respectively. Shaded areas around the data points within each stellar mass range indicate the observed scatter. The intrinsic scatter is calculated from the observed scatter and the measurement scatter for each sample ($\sigma^2_{\rm obs} = \sigma^2_{\rm meas} + \sigma^2_{\rm int}$).

For LMGs, $\sigma_{\rm int}$ is estimated 0.22 and 0.33 with the N2 and the O3N2 line ratios, respectively. These numbers for IMGs are 0.15 and 0.33. While the intrinsic scatter for LMGs and IMGs is similar with the O3N2 line ratio, it is $\sim$ 1.5 times larger for LMGs compared to IMGs with the N2 line ratios. Our results align with those of Zahid et al. (2012) and Guo et al. (2016) and can be explained by diversity in star formation histories (SFHs) and the effect of the galaxy environment on LMGs.

## 4.5 Discussion & Summary

In this paper, we conducted a comprehensive analysis of dwarf galaxies (i.e., LMGs) in the COSMOS field at $z \sim 0.15$ and compared their properties extracted from rest-frame optical emission lines with those of IMGs. The deep optical spectroscopy for our galaxies is carried out using the IMACS/Magellan telescope. The final sample of LMGs (IMGs) consists of 176 (460) galaxies with $3\sigma$ detection in their H$\alpha$ and H$\beta$ lines. Using the COSMOS2020 `CLASSIC` catalog for the photometry of galaxies and fixing their redshifts to the spectroscopic values, we performed SED fitting with `Bagpipes` and estimated the physical properties of LMGs and IMGs, such as stellar mass, SFR, and stellar dust attenuation. Our key findings are summarized below:

- We measured the dust-corrected (from Balmer decrement) SFR from the H$\alpha$ line fluxes and compared them with SED-derived SFRs and observed fairly good agreement among the two measurements. We also placed our LMGs and IMGs on the SFR-$M_*$ plane and found that the slope of the best-fit line for the SFR-$M_*$ relation of LMGs and IMGs is similar ($\Delta\log(\mathrm{SFR_{H\alpha}})/\Delta\log(M_*/M_\odot) \sim 1$).

- The attenuation toward the HII regions within galaxies and that of the stellar continuum

is compared for our samples of galaxies. We investigated the variation of nebular to stellar color excess as a function of stellar mass and sSFR for LMGs and IMGs. Our LMGs show higher nebular to stellar dust attenuation ($\sim 5$) compared to IMGs ($\sim 2$), and this ratio increases with the increase of sSFR. We speculate that the dust geometry within LMGs is different than that of IMGs, which correlates with regions of intense star formation.

- We further investigated the AGN contamination in our sample based on two diagnostic diagrams (MEx and BPT diagrams) to remove AGNs for robust gas-phase metallicity measurements. We measured the gas-phase metallicity of our galaxies with two indicators of N2 and O3N2 and found a shallower slope for the median trend of MZR for LMGs compared to IMGs.

- To explore the existence of FMR for our LMGs and IMGs, we investigated the residuals in the line ratios from the median line ratios as a function of residuals in sSFR from the best-fit line to the sSFR-$M_*$ relation. The existence of FMR for both LMGs and IMGs is confirmed, such that at a fixed stellar mass, galaxies with higher gas-phase metallicity have a lower SFR.

- We examined the deviation from the median trend of line ratios as a function of stellar mass for LMGs and IMGs and found that the intrinsic scatter in the line ratio residuals for LMGs is higher by a factor of 1.5 compared to that of IMGs when using the N2 line ratio. The large intrinsic scatter in LMGs can be attributed to their diverse SFHs or the effect of the environment on these galaxies. Further investigations on the SFHs and the environment of dwarf galaxies are needed to confirm these speculations.

# Chapter 5

# Summary and Conclusions

This thesis is focused on exploring the intricate processes that govern galaxy formation and evolution across different cosmic epochs and environments. Through a series of detailed spectroscopic and imaging studies, we investigate the metallicity, star formation characteristics, and structural properties of galaxies from the early universe to the more recent universe. This work sheds light on the underlying mechanisms that influence galaxy growth and evolution by examining galaxies within diverse contexts—from dense protoclusters to isolated field galaxies. Each chapter of this thesis contributes unique insights into these complex dynamics using observational data and analytical techniques. The following summaries encapsulate the key findings from each chapter.

## 5.1 Summary of Chapter 2

In the second chapter of this thesis, we studied the metal enrichment of galaxies residing in a protocluster at $z = 2.23$ in the COSMOS field. These galaxies, confirmed via Keck

I/MOSFIRE spectroscopy in the $K$ band, were initially narrowband-selected H$\alpha$ emitter candidates from the HiZELS survey. Using the [NII]$\lambda$6584/H$\alpha$ ratio, we measured the gas-phase metallicity of 19 protocluster members and 24 galaxies of a field sample at the same redshift. Their mass-metallicity relation (MZR) revealed that protocluster galaxies, within the stellar mass range of $10^{9.9}\mathrm{M}_{\odot} \leq \mathrm{M}_{*} \leq 10^{10.9}\mathrm{M}_{\odot}$, are metal deficient by $0.10 \pm 0.04$ dex ($2.5\sigma$ significance) relative to their field counterparts. Our study suggested that primordial cold gas, flowing through cosmic filaments, dilutes the metal content of the protocluster. Additionally, the frequent occurrence of minor and major mergers in high-redshift dense environments may also contribute to the observed metal deficiency in the CC2.2 protocluster (Sattari et al., 2021).

## 5.2 Summary of Chapter 3

In Sattari et al. (2023), we studied the nature of giant star-forming clumps, prominent features in high-redshift star-forming galaxies (SFGs). We developed a novel technique to identify clumps in the rest-frame UV 1600 Å images of 6767 galaxies at $0.5 \leq z \leq 3$, using data from CANDELS and UVCANDELS HST surveys. We employed a low-pass band filter in Fourier space to reconstruct the background of each galaxy, enabling the identification of small-scale structures, referred to as clumps, in the background-subtracted image. Our method is validated through the inclusion of synthetic clumps into galaxy images to test the detection algorithm's completeness.

We investigated the fraction of clumpy galaxies ($\mathrm{f}_{\mathrm{clumpy}}$) as a function of redshift and also the physical properties of galaxies, such as stellar mass and environment. A steep decline in the clumpiness of SFGs can be observed at late times, aligning with the trend in star forma-

tion rate density. Consequently, the universe's increasing SFR at cosmic noon might be partly attributed to the prevalence of clumpy galaxies at that time.

Moreover, for the first time, we examined the fraction of clumpy galaxies in relation to their local environment up to $z = 3$ and found that $f_{clumpy}$ remains almost consistent, irrespective of the environment. This observation was further supported by the clumpy fraction measurements in a spectroscopically-confirmed cluster at $z = 1.61$. Such findings suggest that internal processes, such as violent disk instability, are primary drivers of clump formation, challenging the role of mergers in forming clumps in dense environments. We also studied the fraction of clumpy galaxies as a function of stellar mass and found that it inversely correlates with stellar mass across all redshift bins, with low-mass galaxies hosting more clumps.

## 5.3 Summary of Chapter 4

This chapter presents a thorough spectroscopic study of low-mass galaxies (LMGs) and intermediate-mass galaxies (IMGs) in the COSMOS field, highlighting significant insights into their physical characteristics, star formation rates, dust attenuation, and metallicities. Utilizing the IMACS/Magellan telescope, the study analyzes galaxies with stellar masses between $10^8 \leq M_*/M_\odot \leq 10^9$ (for LMGs) and $10^9 \leq M_*/M_\odot \leq 10^{10}$ (for IMGs) at $z \sim 0.15$ and $z \sim 0.35$, respectively. We found a consistent star formation rate-mass relationship for both LMGs and IMGs ($\Delta\log(SFR_{H\alpha})/\Delta\log(M_*/M_\odot) \sim 1$).

A notable finding in this study is the varying degrees of dust attenuation between LMGs and IMGs, with LMGs exhibiting a higher nebular-to-stellar attenuation ratio. This suggests different dust geometries within LMGs, likely influenced by their more intense star-forming

regions. Such distinctions in dust properties could be pivotal in understanding the structure of the interstellar medium and the role of dust in galaxy evolution.

Furthermore, our examination of the mass-metallicity relation (MZR) using N2 and O3N2 indicators to calculate gas-phase metallicity shows that LMGs have a shallower slope in their MZR trend compared to that of IMGs. This observation suggests that fundamental processes influencing metal enrichment and retention might be different across different galaxy masses. Also, the analysis of the Fundamental Metallicity Relation (FMR) reveals that this relation exists for both LMGs and IMGs, indicating that galaxies with higher metallicity tend to have lower SFRs at a given stellar mass.

Moreover, our study highlights that LMGs display a larger intrinsic scatter in the MZR compared to IMGs. This variance could indicate more diverse star formation histories or a stronger influence of environmental factors on smaller galaxies. Understanding these disparities provides deeper insights into the evolutionary paths and growth mechanisms of galaxies across the mass spectrum.

# References

Abadi, M. G., Moore, B., and Bower, R. G. (1999). Ram pressure stripping of spiral galaxies in clusters. , 308(4):947–954.

Abazajian, K. N., Adelman-McCarthy, J. K., Agüeros, M. A., Allam, S. S., Allende Prieto, C., An, D., Anderson, K. S. J., Anderson, S. F., Annis, J., Bahcall, N. A., Bailer-Jones, C. A. L., Barentine, J. C., Bassett, B. A., Becker, A. C., Beers, T. C., Bell, E. F., Belokurov, V., Berlind, A. A., Berman, E. F., Bernardi, M., Bickerton, S. J., Bizyaev, D., Blakeslee, J. P., Blanton, M. R., Bochanski, J. J., Boroski, W. N., Brewington, H. J., Brinchmann, J., Brinkmann, J., Brunner, R. J., Budavári, T., Carey, L. N., Carliles, S., Carr, M. A., Castander, F. J., Cinabro, D., Connolly, A. J., Csabai, I., Cunha, C. E., Czarapata, P. C., Davenport, J. R. A., de Haas, E., Dilday, B., Doi, M., Eisenstein, D. J., Evans, M. L., Evans, N. W., Fan, X., Friedman, S. D., Frieman, J. A., Fukugita, M., Gänsicke, B. T., Gates, E., Gillespie, B., Gilmore, G., Gonzalez, B., Gonzalez, C. F., Grebel, E. K., Gunn, J. E., Györy, Z., Hall, P. B., Harding, P., Harris, F. H., Harvanek, M., Hawley, S. L., Hayes, J. J. E., Heckman, T. M., Hendry, J. S., Hennessy, G. S., Hindsley, R. B., Hoblitt, J., Hogan, C. J., Hogg, D. W., Holtzman, J. A., Hyde, J. B., Ichikawa, S.-i., Ichikawa, T., Im, M., Ivezić, Ž., Jester, S., Jiang, L., Johnson, J. A., Jorgensen, A. M., Jurić, M., Kent, S. M., Kessler, R., Kleinman, S. J., Knapp, G. R., Konishi, K., Kron, R. G.,

Krzesinski, J., Kuropatkin, N., Lampeitl, H., Lebedeva, S., Lee, M. G., Lee, Y. S., French Leger, R., Lépine, S., Li, N., Lima, M., Lin, H., Long, D. C., Loomis, C. P., Loveday, J., Lupton, R. H., Magnier, E., Malanushenko, O., Malanushenko, V., Mandelbaum, R., Margon, B., Marriner, J. P., Martínez-Delgado, D., Matsubara, T., McGehee, P. M., McKay, T. A., Meiksin, A., Morrison, H. L., Mullally, F., Munn, J. A., Murphy, T., Nash, T., Nebot, A., Neilsen, Eric H., J., Newberg, H. J., Newman, P. R., Nichol, R. C., Nicinski, T., Nieto-Santisteban, M., Nitta, A., Okamura, S., Oravetz, D. J., Ostriker, J. P., Owen, R., Padmanabhan, N., Pan, K., Park, C., Pauls, G., Peoples, John, J., Percival, W. J., Pier, J. R., Pope, A. C., Pourbaix, D., Price, P. A., Purger, N., Quinn, T., Raddick, M. J., Re Fiorentin, P., Richards, G. T., Richmond, M. W., Riess, A. G., Rix, H.-W., Rockosi, C. M., Sako, M., Schlegel, D. J., Schneider, D. P., Scholz, R.-D., Schreiber, M. R., Schwope, A. D., Seljak, U., Sesar, B., Sheldon, E., Shimasaku, K., Sibley, V. C., Simmons, A. E., Sivarani, T., Allyn Smith, J., Smith, M. C., Smolčić, V., Snedden, S. A., Stebbins, A., Steinmetz, M., Stoughton, C., Strauss, M. A., SubbaRao, M., Suto, Y., Szalay, A. S., Szapudi, I., Szkody, P., Tanaka, M., Tegmark, M., Teodoro, L. F. A., Thakar, A. R., Tremonti, C. A., Tucker, D. L., Uomoto, A., Vanden Berk, D. E., Vandenberg, J., Vidrih, S., Vogeley, M. S., Voges, W., Vogt, N. P., Wadadekar, Y., Watters, S., Weinberg, D. H., West, A. A., White, S. D. M., Wilhite, B. C., Wonders, A. C., Yanny, B., Yocum, D. R., York, D. G., Zehavi, I., Zibetti, S., and Zucker, D. B. (2009). The Seventh Data Release of the Sloan Digital Sky Survey. , 182(2):543–558.

Adamo, A., Östlin, G., Bastian, N., Zackrisson, E., Livermore, R. C., and Guaita, L. (2013). High-resolution Study of the Cluster Complexes in a Lensed Spiral at Redshift 1.5: Constraints on the Bulge Formation and Disk Evolution. , 766(2):105.

Adams, D., Mehta, V., Dickinson, H., Scarlata, C., Fortson, L., Kruk, S., Simmons, B., and Lintott, C. (2022). Galaxy Zoo: Clump Scout: Surveying the Local Universe for Giant Star-forming Clumps. , 931(1):16.

Agertz, O., Teyssier, R., and Moore, B. (2009). Disc formation and the origin of clumpy galaxies at high redshift. , 397(1):L64–L68.

Alcorn, L. Y., Gupta, A., Tran, K.-V., Kacprzak, G. G., Yuan, T., Cohn, J., Forrest, B., Glazebrook, K., Harshan, A., Kewley, L. J., Labbé, I., Nanayakkara, T., Papovich, C., Spitler, L. R., and Straatman, C. M. S. (2019). A Tale of Two Clusters: An Analysis of Gas-phase Metallicity and Nebular Gas Conditions in Proto-cluster Galaxies at z $\sim$ 2. , 883(2):153.

Ambachew, L., Fisher, D. B., Glazebrook, K., Girard, M., Obreschkow, D., Abraham, R., Bolatto, A., Lenkić, L., and Damjanov, I. (2022). Stellar masses of clumps in gas-rich, turbulent disc galaxies. , 512(2):3079–3097.

Ando, M., Shimasaku, K., and Momose, R. (2020). A systematic search for galaxy proto-cluster cores at z $\sim$ 2. , 496(3):3169–3181.

Andrews, B. H. and Martini, P. (2013). The Mass-Metallicity Relation with the Direct Method on Stacked Spectra of SDSS Galaxies. , 765(2):140.

Arnouts, S., Cristiani, S., Moscardini, L., Matarrese, S., Lucchin, F., Fontana, A., and Giallongo, E. (1999). Measuring and modelling the redshift evolution of clustering: the Hubble Deep

Field North. , 310(2):540–556.

Arnouts, S., Le Floc'h, E., Chevallard, J., Johnson, B. D., Ilbert, O., Treyer, M., Aussel, H., Capak, P., Sanders, D. B., Scoville, N., McCracken, H. J., Milliard, B., Pozzetti, L., and Salvato, M. (2013). Encoding of the infrared excess in the NUVrK color diagram for star-forming galaxies. , 558:A67.

Arnouts, S., Moscardini, L., Vanzella, E., Colombi, S., Cristiani, S., Fontana, A., Giallongo, E., Matarrese, S., and Saracco, P. (2002). Measuring the redshift evolution of clustering: the Hubble Deep Field South. , 329(2):355–366.

Atek, H., Richard, J., Kneib, J.-P., Jauzac, M., Schaerer, D., Clement, B., Limousin, M., Jullo, E., Natarajan, P., Egami, E., and Ebeling, H. (2015). New Constraints on the Faint End of the UV Luminosity Function at z $\sim$ 7-8 Using the Gravitational Lensing of the Hubble Frontier Fields Cluster A2744. , 800(1):18.

Baldry, I. K., Driver, S. P., Loveday, J., Taylor, E. N., Kelvin, L. S., Liske, J., Norberg, P., Robotham, A. S. G., Brough, S., Hopkins, A. M., Bamford, S. P., Peacock, J. A., Bland-Hawthorn, J., Conselice, C. J., Croom, S. M., Jones, D. H., Parkinson, H. R., Popescu, C. C., Prescott, M., Sharp, R. G., and Tuffs, R. J. (2012). Galaxy And Mass Assembly (GAMA): the galaxy stellar mass function at z $<$ 0.06. , 421(1):621–634.

Baldwin, J. A., Phillips, M. M., and Terlevich, R. (1981). Classification parameters for the emission-line spectra of extragalactic objects. , 93:5–19.

Balogh, M., Eke, V., Miller, C., Lewis, I., Bower, R., Couch, W., Nichol, R., Bland -Hawthorn, J., Baldry, I. K., Baugh, C., Bridges, T., Cannon, R., Cole, S., Colless, M., Collins, C., Cross, N., Dalton, G., de Propris, R., Driver, S. P., Efstathiou, G., Ellis, R. S., Frenk, C. S., Glazebrook, K., Gomez, P., Gray, A., Hawkins, E., Jackson, C., Lahav, O., Lumsden, S., Maddox, S., Madgwick, D., Norberg, P., Peacock, J. A., Percival, W., Peterson, B. A., Sutherland, W., and Taylor, K. (2004). Galaxy ecology: groups and low-density environments in the SDSS and 2dFGRS. , 348(4):1355–1372.

Balogh, M. L., McGee, S. L., Mok, A., Muzzin, A., van der Burg, R. F. J., Bower, R. G., Finoguenov, A., Hoekstra, H., Lidman, C., Mulchaey, J. S., Noble, A., Parker, L. C., Tanaka, M., Wilman, D. J., Webb, T., Wilson, G., and Yee, H. K. C. (2016). Evidence for a change in the dominant satellite galaxy quenching mechanism at z = 1. , 456(4):4364–4376.

Barro, G., Pérez-González, P. G., Cava, A., Brammer, G., Pandya, V., Eliche Moral, C., Esquej, P., Domínguez-Sánchez, H., Alcalde Pampliega, B., Guo, Y., Koekemoer, A. M., Trump, J. R., Ashby, M. L. N., Cardiel, N., Castellano, M., Conselice, C. J., Dickinson, M. E., Dolch, T., Donley, J. L., Espino Briones, N., Faber, S. M., Fazio, G. G., Ferguson, H., Finkelstein, S., Fontana, A., Galametz, A., Gardner, J. P., Gawiser, E., Giavalisco, M., Grazian, A., Grogin, N. A., Hathi, N. P., Hemmati, S., Hernán-Caballero, A., Kocevski, D., Koo, D. C., Kodra, D., Lee, K.-S., Lin, L., Lucas, R. A., Mobasher, B., McGrath, E. J., Nandra, K., Nayyeri, H., Newman, J. A., Pforr, J., Peth, M., Rafelski, M., Rodríguez-Munoz, L., Salvato, M., Stefanon, M., van der Wel, A., Willner, S. P., Wiklind, T., and Wuyts, S. (2019). The CANDELS/SHARDS Multiwavelength Catalog in GOODS-N: Photometry, Photometric Redshifts, Stellar Masses,

Emission-line Fluxes, and Star Formation Rates. , 243(2):22.

Beckwith, S. V. W., Stiavelli, M., Koekemoer, A. M., Caldwell, J. A. R., Ferguson, H. C., Hook, R., Lucas, R. A., Bergeron, L. E., Corbin, M., Jogee, S., Panagia, N., Robberto, M., Royle, P., Somerville, R. S., and Sosey, M. (2006). The Hubble Ultra Deep Field. , 132(5):1729–1755.

Behroozi, P. S., Wechsler, R. H., and Conroy, C. (2013a). On the Lack of Evolution in Galaxy Star Formation Efficiency. , 762(2):L31.

Behroozi, P. S., Wechsler, R. H., and Conroy, C. (2013b). The Average Star Formation Histories of Galaxies in Dark Matter Halos from z = 0-8. , 770(1):57.

Berg, D. A., Skillman, E. D., Marble, A. R., van Zee, L., Engelbracht, C. W., Lee, J. C., Kennicutt, Robert C., J., Calzetti, D., Dale, D. A., and Johnson, B. D. (2012). Direct Oxygen Abundances for Low-luminosity LVL Galaxies. , 754(2):98.

Bertin, E. and Arnouts, S. (1996). SExtractor: Software for source extraction. , 117:393–404.

Boquien, M., Burgarella, D., Roehlly, Y., Buat, V., Ciesla, L., Corre, D., Inoue, A. K., and Salas, H. (2019). CIGALE: a python Code Investigating GALaxy Emission. , 622:A103.

Boselli, A. and Gavazzi, G. (2006). Environmental Effects on Late-Type Galaxies in Nearby Clusters. , 118(842):517–559.

Bournaud, F., Daddi, E., Elmegreen, B. G., Elmegreen, D. M., Nesvadba, N., Vanzella, E., Di

Matteo, P., Le Tiran, L., Lehnert, M., and Elbaz, D. (2008). Observations and modeling of a clumpy galaxy at z = 1.6. Spectroscopic clues to the origin and evolution of chain galaxies. , 486(3):741–753.

Bournaud, F., Elmegreen, B. G., and Elmegreen, D. M. (2007). Rapid Formation of Exponential Disks and Bulges at High Redshift from the Dynamical Evolution of Clump-Cluster and Chain Galaxies. , 670(1):237–248.

Bournaud, F., Elmegreen, B. G., and Martig, M. (2009). The Thick Disks of Spiral Galaxies as Relics from Gas-rich, Turbulent, Clumpy Disks at High Redshift. , 707(1):L1–L5.

Bournaud, F., Perret, V., Renaud, F., Dekel, A., Elmegreen, B. G., Elmegreen, D. M., Teyssier, R., Amram, P., Daddi, E., Duc, P.-A., Elbaz, D., Epinat, B., Gabor, J. M., Juneau, S., Kraljic, K., and Le Floch', E. (2014). The Long Lives of Giant Clumps and the Birth of Outflows in Gas-rich Galaxies at High Redshift. , 780(1):57.

Bouwens, R. J., Illingworth, G. D., Oesch, P. A., Labbé, I., Trenti, M., van Dokkum, P., Franx, M., Stiavelli, M., Carollo, C. M., Magee, D., and Gonzalez, V. (2011). Ultraviolet Luminosity Functions from 132 z $\sim$ 7 and z $\sim$ 8 Lyman-break Galaxies in the Ultra-deep HUDF09 and Wide-area Early Release Science WFC3/IR Observations. , 737(2):90.

Bradley, L., Sipőcz, B., Robitaille, T., Tollerud, E., Vinícius, Z., Deil, C., Barbary, K., Wilson, T. J., Busko, I., Günther, H. M., Cara, M., Conseil, S., Bostroem, A., Droettboom, M., Bray, E. M., Bratholm, L. A., Lim, P. L., Barentsen, G., Craig, M., Pascual, S., Perren, G., Greco, J., Donath,

A., de Val-Borro, M., Kerzendorf, W., Bach, Y. P., Weaver, B. A., D'Eugenio, F., Souchereau, H., and Ferreira, L. (2020). astropy/photutils: 1.0.0.

Brammer, G. B., van Dokkum, P. G., and Coppi, P. (2008). EAZY: A Fast, Public Photometric Redshift Code. , 686(2):1503–1513.

Brooks, A. M., Governato, F., Booth, C. M., Willman, B., Gardner, J. P., Wadsley, J., Stinson, G., and Quinn, T. (2007). The Origin and Evolution of the Mass-Metallicity Relationship for Galaxies: Results from Cosmological N-Body Simulations. , 655(1):L17–L20.

Bruzual, G. and Charlot, S. (2003). Stellar population synthesis at the resolution of 2003. , 344(4):1000–1028.

Bulichi, T.-E., Fahrion, K., Mernier, F., Hilker, M., Leaman, R., Lyubenova, M., Müller, O., Neumayer, N., Martin-Navarro, I., Pinna, F., Rejkuba, M., Scholz-Diaz, L., and van de Ven, G. (2023). Expanding on the fundamental metallicity relation in dwarf galaxies with MUSE. , 679:A98.

Burgarella, D., Buat, V., and Iglesias-Páramo, J. (2005). Star formation and dust attenuation properties in galaxies from a statistical ultraviolet-to-far-infrared analysis. , 360(4):1413–1425.

Byler, N., Dalcanton, J. J., Conroy, C., and Johnson, B. D. (2017). Nebular Continuum and Line Emission in Stellar Population Synthesis Models. , 840(1):44.

Calabrò, A., Daddi, E., Fensch, J., Bournaud, F., Cibinel, A., Puglisi, A., Jin, S., Delvecchio, I., and D'Eugenio, C. (2019). Merger induced clump formation in distant infrared luminous starburst galaxies. , 632:A98.

Calzetti, D. (2013). Star Formation Rate Indicators. In Falcón-Barroso, J. and Knapen, J. H., editors, *Secular Evolution of Galaxies*, page 419.

Calzetti, D., Armus, L., Bohlin, R. C., Kinney, A. L., Koornneef, J., and Storchi-Bergmann, T. (2000). The Dust Content and Opacity of Actively Star-forming Galaxies. , 533(2):682–695.

Calzetti, D., Kinney, A. L., and Storchi-Bergmann, T. (1994). Dust Extinction of the Stellar Continua in Starburst Galaxies: The Ultraviolet and Optical Extinction Law. , 429:582.

Carnall, A. C., McLure, R. J., Dunlop, J. S., and Davé, R. (2018). Inferring the star formation histories of massive quiescent galaxies with BAGPIPES: evidence for multiple quenching mechanisms. , 480(4):4379–4401.

Cava, A., Schaerer, D., Richard, J., Pérez-González, P. G., Dessauges-Zavadsky, M., Mayer, L., and Tamburello, V. (2018). The nature of giant clumps in distant galaxies probed by the anatomy of the cosmic snake. *Nature Astronomy*, 2:76–82.

Ceverino, D., Dekel, A., and Bournaud, F. (2010). High-redshift clumpy discs and bulges in cosmological simulations. , 404(4):2151–2169.

Ceverino, D., Dekel, A., Mandelker, N., Bournaud, F., Burkert, A., Genzel, R., and Primack, J. (2012). Rotational support of giant clumps in high-z disc galaxies. , 420(4):3490–3520.

Ceverino, D., Klypin, A., Klimek, E. S., Trujillo-Gomez, S., Churchill, C. W., Primack, J., and Dekel, A. (2014). Radiative feedback and the low efficiency of galaxy formation in low-mass haloes at high redshift. , 442(2):1545–1559.

Chabrier, G. (2003). Galactic Stellar and Substellar Initial Mass Function. , 115(809):763–795.

Charlot, S. and Fall, S. M. (2000). A Simple Model for the Absorption of Starlight by Dust in Galaxies. , 539(2):718–731.

Chartab, N., Cooray, A., Ma, J., Nayyeri, H., Zilliot, P., Lopez, J., Fadda, D., Herrera-Camus, R., Malkan, M., Rigopoulou, D., Sheth, K., and Wardlow, J. (2022). Low gas-phase metallicities of ultraluminous infrared galaxies are a result of dust obscuration. *Nature Astronomy*, 6:844–849.

Chartab, N., Mobasher, B., Darvish, B., Finkelstein, S., Guo, Y., Kodra, D., Lee, K.-S., Newman, J. A., Pacifici, C., Papovich, C., Sattari, Z., Shahidi, A., Dickinson, M. E., Faber, S. M., Ferguson, H. C., Giavalisco, M., and Jafariyazani, M. (2020). Large-scale Structures in the CANDELS Fields: The Role of the Environment in Star Formation Activity. , 890(1):7.

Chartab, N., Mobasher, B., Shapley, A. E., Shivaei, I., Sanders, R. L., Coil, A. L., Kriek, M., Reddy, N. A., Siana, B., Freeman, W. R., Azadi, M., Barro, G., Fetherolf, T., Leung, G., Price,

S. H., and Zick, T. (2021). The MOSDEF Survey: Environmental dependence of the gas-phase metallicity of galaxies at $1.4 \leq z \leq 2.6$. *arXiv e-prints*, page arXiv:2101.01706.

Chartab, N., Newman, A. B., Rudie, G. C., Blanc, G. A., and Kelson, D. D. (2024). LATIS: The Stellar Mass-Metallicity Relation of Star-forming Galaxies at z 2.5. , 960(1):73.

Chisholm, J., Tremonti, C., and Leitherer, C. (2018). Metal-enriched galactic outflows shape the mass-metallicity relationship. , 481(2):1690–1706.

Claeyssens, A., Adamo, A., Richard, J., Mahler, G., Messa, M., and Dessauges-Zavadsky, M. (2023). Star formation at the smallest scales: a JWST study of the clump populations in SMACS0723. , 520(2):2180–2203.

Coe, D., Bradley, L., and Zitrin, A. (2015). Frontier Fields: High-redshift Predictions and Early Results. , 800(2):84.

Coil, A. L., Aird, J., Reddy, N., Shapley, A. E., Kriek, M., Siana, B., Mobasher, B., Freeman, W. R., Price, S. H., and Shivaei, I. (2015). The MOSDEF Survey: Optical Active Galactic Nucleus Diagnostics at z $\sim$ 2.3. , 801(1):35.

Cole, S., Lacey, C. G., Baugh, C. M., and Frenk, C. S. (2000). Hierarchical galaxy formation. , 319(1):168–204.

Conselice, C. J., Grogin, N. A., Jogee, S., Lucas, R. A., Dahlen, T., de Mello, D., Gardner, J. P.,

Mobasher, B., and Ravindranath, S. (2004). Observing the Formation of the Hubble Sequence in the Great Observatories Origins Deep Survey. , 600(2):L139–L142.

Cooper, M. C., Newman, J. A., Weiner, B. J., Yan, R., Willmer, C. N. A., Bundy, K., Coil, A. L., Conselice, C. J., Davis, M., Faber, S. M., Gerke, B. F., Guhathakurta, P., Koo, D. C., and Noeske, K. G. (2008). The DEEP2 Galaxy Redshift Survey: the role of galaxy environment in the cosmic star formation history. , 383(3):1058–1078.

Cresci, G., Mannucci, F., Sommariva, V., Maiolino, R., Marconi, A., and Brusa, M. (2012). The metallicity properties of zCOSMOS galaxies at $0.2 < z < 0.8$. , 421(1):262–269.

Cullen, F., McLure, R. J., Khochfar, S., Dunlop, J. S., Dalla Vecchia, C., Carnall, A. C., Bourne, N., Castellano, M., Cimatti, A., Cirasuolo, M., Elbaz, D., Fynbo, J. P. U., Garilli, B., Koekemoer, A., Marchi, F., Pentericci, L., Talia, M., and Zamorani, G. (2018). The VANDELS survey: dust attenuation in star-forming galaxies at $z = 3$-4. , 476(3):3218–3232.

Curti, M., Maiolino, R., Curtis-Lake, E., Chevallard, J., Carniani, S., D'Eugenio, F., Looser, T. J., Scholtz, J., Charlot, S., Cameron, A., Übler, H., Witstok, J., Boyett, K., Laseter, I., Sandles, L., Arribas, S., Bunker, A., Giardino, G., Maseda, M. V., Rawle, T., Rodríguez Del Pino, B., Smit, R., Willott, C. J., Eisenstein, D. J., Hausen, R., Johnson, B., Rieke, M., Robertson, B., Tacchella, S., Williams, C. C., Willmer, C., Baker, W. M., Bhatawdekar, R., Egami, E., Helton, J. M., Ji, Z., Kumari, N., Perna, M., Shivaei, I., and Sun, F. (2024). JADES: Insights into the low-mass end of the mass-metallicity-SFR relation at $3 < z < 10$ from deep JWST/NIRSpec

spectroscopy. , 684:A75.

Darvish, B., Mobasher, B., Martin, D. C., Sobral, D., Scoville, N., Stroe, A., Hemmati, S., and Kartaltepe, J. (2017). Cosmic Web of Galaxies in the COSMOS Field: Public Catalog and Different Quenching for Centrals and Satellites. , 837(1):16.

Darvish, B., Mobasher, B., Sobral, D., Hemmati, S., Nayyeri, H., and Shivaei, I. (2015). Spectroscopic Study of Star-forming Galaxies in Filaments and the Field at z $\sim$ 0.5: Evidence for Environmental Dependence of Electron Density. , 814(2):84.

Darvish, B., Mobasher, B., Sobral, D., Rettura, A., Scoville, N., Faisst, A., and Capak, P. (2016). The Effects of the Local Environment and Stellar Mass on Galaxy Quenching to z $\sim$ 3. , 825:113.

Darvish, B., Scoville, N. Z., Martin, C., Sobral, D., Mobasher, B., Rettura, A., Matthee, J., Capak, P., Chartab, N., Hemmati, S., Masters, D., Nayyeri, H., O'Sullivan, D., Paulino-Afonso, A., Sattari, Z., Shahidi, A., Salvato, M., Lemaux, B. C., Fèvre, O. L., and Cucciati, O. (2020). Spectroscopic Confirmation of a Coma Cluster Progenitor at z $\sim$ 2.2. , 892(1):8.

Dekel, A. and Birnboim, Y. (2006). Galaxy bimodality due to cold flows and shock heating. , 368(1):2–20.

Dekel, A., Birnboim, Y., Engel, G., Freundlich, J., Goerdt, T., Mumcuoglu, M., Neistein, E., Pichon, C., Teyssier, R., and Zinger, E. (2009a). Cold streams in early massive hot haloes as

the main mode of galaxy formation. , 457(7228):451–454.

Dekel, A. and Burkert, A. (2014). Wet disc contraction to galactic blue nuggets and quenching to red nuggets. , 438(2):1870–1879.

Dekel, A., Mandelker, N., Bournaud, F., Ceverino, D., Guo, Y., and Primack, J. (2022). Clump survival and migration in VDI galaxies: an analytical model versus simulations and observations. , 511(1):316–340.

Dekel, A., Sari, R., and Ceverino, D. (2009b). Formation of Massive Galaxies at High Redshift: Cold Streams, Clumpy Disks, and Compact Spheroids. , 703(1):785–801.

Dekel, A. and Silk, J. (1986). The Origin of Dwarf Galaxies, Cold Dark Matter, and Biased Galaxy Formation. , 303:39.

Dessauges-Zavadsky, M. and Adamo, A. (2018). First constraints on the stellar mass function of star-forming clumps at the peak of cosmic star formation. , 479(1):L118–L122.

Dessauges-Zavadsky, M., Richard, J., Combes, F., Schaerer, D., Rujopakarn, W., Mayer, L., Cava, A., Boone, F., Egami, E., Kneib, J.-P., Pérez-González, P. G., Pfenniger, D., Rawle, T. D., Teyssier, R., and van der Werf, P. P. (2019). Molecular clouds in the Cosmic Snake normal star-forming galaxy 8 billion years ago. *Nature Astronomy*, 3:1115–1121.

Dessauges-Zavadsky, M., Schaerer, D., Cava, A., Mayer, L., and Tamburello, V. (2017). On the

Stellar Masses of Giant Clumps in Distant Star-forming Galaxies. , 836(2):L22.

Domínguez, A., Siana, B., Henry, A. L., Scarlata, C., Bedregal, A. G., Malkan, M., Atek, H., Ross, N. R., Colbert, J. W., Teplitz, H. I., Rafelski, M., McCarthy, P., Bunker, A., Hathi, N. P., Dressler, A., Martin, C. L., and Masters, D. (2013). Dust Extinction from Balmer Decrements of Star-forming Galaxies at 0.75 <= z <= 1.5 with Hubble Space Telescope/Wide-Field-Camera 3 Spectroscopy from the WFC3 Infrared Spectroscopic Parallel Survey. , 763(2):145.

Donley, J. L., Koekemoer, A. M., Brusa, M., Capak, P., Cardamone, C. N., Civano, F., Ilbert, O., Impey, C. D., Kartaltepe, J. S., Miyaji, T., Salvato, M., Sanders, D. B., Trump, J. R., and Zamorani, G. (2012). Identifying Luminous Active Galactic Nuclei in Deep Surveys: Revised IRAC Selection Criteria. , 748(2):142.

Dressler, A. (1980). Galaxy morphology in rich clusters: implications for the formation and evolution of galaxies. , 236:351–365.

Dressler, A., Bigelow, B., Hare, T., Sutin, B., Thompson, I., Burley, G., Epps, H., Oemler, Augustus, J., Bagish, A., Birk, C., Clardy, K., Gunnels, S., Kelson, D., Shectman, S., and Osip, D. (2011). IMACS: The Inamori-Magellan Areal Camera and Spectrograph on Magellan-Baade. , 123(901):288.

Duncan, K., Conselice, C. J., Mundy, C., Bell, E., Donley, J., Galametz, A., Guo, Y., Grogin, N. A., Hathi, N., Kartaltepe, J., Kocevski, D., Koekemoer, A. M., Pérez-González, P. G., Mantha, K. B., Snyder, G. F., and Stefanon, M. (2019). Observational Constraints on the Merger History of

Galaxies since z ≈ 6: Probabilistic Galaxy Pair Counts in the CANDELS Fields. , 876(2):110.

Elbaz, D., Daddi, E., Le Borgne, D., Dickinson, M., Alexander, D. M., Chary, R. R., Starck, J. L., Brandt, W. N., Kitzbichler, M., MacDonald, E., Nonino, M., Popesso, P., Stern, D., and Vanzella, E. (2007). The reversal of the star formation-density relation in the distant universe. , 468(1):33–48.

Ellis, R. S., McLure, R. J., Dunlop, J. S., Robertson, B. E., Ono, Y., Schenker, M. A., Koekemoer, A., Bowler, R. A. A., Ouchi, M., Rogers, A. B., Curtis-Lake, E., Schneider, E., Charlot, S., Stark, D. P., Furlanetto, S. R., and Cirasuolo, M. (2013). The Abundance of Star-forming Galaxies in the Redshift Range 8.5-12: New Results from the 2012 Hubble Ultra Deep Field Campaign. , 763(1):L7.

Ellison, S. L., Simard, L., Cowan, N. B., Baldry, I. K., Patton, D. R., and McConnachie, A. W. (2009). The mass-metallicity relation in galaxy clusters: the relative importance of cluster membership versus local environment. , 396(3):1257–1272.

Elmegreen, B. G., Bournaud, F., and Elmegreen, D. M. (2008). Bulge Formation by the Coalescence of Giant Clumps in Primordial Disk Galaxies. , 688(1):67–77.

Elmegreen, B. G. and Elmegreen, D. M. (2005). Stellar Populations in 10 Clump-Cluster Galaxies of the Hubble Ultra Deep Field. , 627(2):632–646.

Elmegreen, B. G., Elmegreen, D. M., Fernandez, M. X., and Lemonias, J. J. (2009). Bulge and

Clump Evolution in Hubble Ultra Deep Field Clump Clusters, Chains and Spiral Galaxies. , 692(1):12–31.

Elmegreen, D. M., Elmegreen, B. G., Ravindranath, S., and Coe, D. A. (2007). Resolved Galaxies in the Hubble Ultra Deep Field: Star Formation in Disks at High Redshift. , 658(2):763–777.

Erb, D. K., Shapley, A. E., Pettini, M., Steidel, C. C., Reddy, N. A., and Adelberger, K. L. (2006). The Mass-Metallicity Relation at z $\gtrsim$2. , 644(2):813–828.

Ferland, G. J., Chatzikos, M., Guzmán, F., Lykins, M. L., van Hoof, P. A. M., Williams, R. J. R., Abel, N. P., Badnell, N. R., Keenan, F. P., Porter, R. L., and Stancil, P. C. (2017). The 2017 Release Cloudy. , 53:385–438.

Finkelstein, S. L., Hill, G. J., Gebhardt, K., Adams, J., Blanc, G. A., Papovich, C., Ciardullo, R., Drory, N., Gawiser, E., Gronwall, C., Schneider, D. P., and Tran, K.-V. (2011). The HETDEX Pilot Survey. III. The Low Metallicities of High-redshift Ly$\alpha$ Galaxies. , 729(2):140.

Fisher, D. B., Glazebrook, K., Abraham, R. G., Damjanov, I., White, H. A., Obreschkow, D., Basset, R., Bekiaris, G., Wisnioski, E., Green, A., and Bolatto, A. D. (2017). Connecting Clump Sizes in Turbulent Disk Galaxies to Instability Theory. , 839(1):L5.

Förster Schreiber, N. M., Shapley, A. E., Genzel, R., Bouché, N., Cresci, G., Davies, R., Erb, D. K., Genel, S., Lutz, D., Newman, S., Shapiro, K. L., Steidel, C. C., Sternberg, A., and Tacconi, L. J. (2011). Constraints on the Assembly and Dynamics of Galaxies. II. Properties of Kiloparsec-

scale Clumps in Rest-frame Optical Emission of z $\sim$ 2 Star-forming Galaxies. , 739(1):45.

Fossati, M., Wilman, D. J., Mendel, J. T., Saglia, R. P., Galametz, A., Beifiori, A., Bender, R., Chan, J. C. C., Fabricius, M., Bandara, K., Brammer, G. B., Davies, R., Förster Schreiber, N. M., Genzel, R., Hartley, W., Kulkarni, S. K., Lang, P., Momcheva, I. G., Nelson, E. J., Skelton, R., Tacconi, L. J., Tadaki, K., Übler, H., van Dokkum, P. G., Wisnioski, E., Whitaker, K. E., Wuyts, E., and Wuyts, S. (2017). Galaxy Environment in the 3D-HST Fields: Witnessing the Onset of Satellite Quenching at z $\sim$ 1-2. , 835(2):153.

Gallagher, J. S., I., Hunter, D. A., and Tutukov, A. V. (1984). Star formation histories of irregular galaxies. , 284:544–556.

Garn, T. and Best, P. N. (2010). Predicting dust extinction from the stellar mass of a galaxy. , 409(1):421–432.

Garnett, D. R. (2002). The Luminosity-Metallicity Relation, Effective Yields, and Metal Loss in Spiral and Irregular Galaxies. , 581(2):1019–1031.

Gburek, T., Siana, B., Alavi, A., Emami, N., Richard, J., Freeman, W. R., Stark, D. P., and Snapp-Kolas, C. (2023). The Direct-method Oxygen Abundance of Typical Dwarf Galaxies at Cosmic High Noon. , 948(2):108.

Geach, J. E., Sobral, D., Hickox, R. C., Wake, D. A., Smail, I., Best, P. N., Baugh, C. M., and Stott, J. P. (2012). The clustering of H$\alpha$ emitters at z=2.23 from HiZELS. , 426(1):679–689.

Genel, S., Naab, T., Genzel, R., Förster Schreiber, N. M., Sternberg, A., Oser, L., Johansson, P. H., Davé, R., Oppenheimer, B. D., and Burkert, A. (2012). Short-lived Star-forming Giant Clumps in Cosmological Simulations of z ≈ 2 Disks. , 745(1):11.

Genzel, R., Burkert, A., Bouché, N., Cresci, G., Förster Schreiber, N. M., Shapley, A., Shapiro, K., Tacconi, L. J., Buschkamp, P., Cimatti, A., Daddi, E., Davies, R., Eisenhauer, F., Erb, D. K., Genel, S., Gerhard, O., Hicks, E., Lutz, D., Naab, T., Ott, T., Rabien, S., Renzini, A., Steidel, C. C., Sternberg, A., and Lilly, S. J. (2008). From Rings to Bulges: Evidence for Rapid Secular Galaxy Evolution at z ∼ 2 from Integral Field Spectroscopy in the SINS Survey. , 687(1):59–77.

Genzel, R., Newman, S., Jones, T., Förster Schreiber, N. M., Shapiro, K., Genel, S., Lilly, S. J., Renzini, A., Tacconi, L. J., Bouché, N., Burkert, A., Cresci, G., Buschkamp, P., Carollo, C. M., Ceverino, D., Davies, R., Dekel, A., Eisenhauer, F., Hicks, E., Kurk, J., Lutz, D., Mancini, C., Naab, T., Peng, Y., Sternberg, A., Vergani, D., and Zamorani, G. (2011). The Sins Survey of z ∼ 2 Galaxy Kinematics: Properties of the Giant Star-forming Clumps. , 733(2):101.

Grogin, N. A., Kocevski, D. D., Faber, S. M., Ferguson, H. C., Koekemoer, A. M., Riess, A. G., Acquaviva, V., Alexander, D. M., Almaini, O., Ashby, M. L. N., Barden, M., Bell, E. F., Bournaud, F., Brown, T. M., Caputi, K. I., Casertano, S., Cassata, P., Castellano, M., Challis, P., Chary, R.-R., Cheung, E., Cirasuolo, M., Conselice, C. J., Roshan Cooray, A., Croton, D. J., Daddi, E., Dahlen, T., Davé, R., de Mello, D. F., Dekel, A., Dickinson, M., Dolch, T., Donley, J. L., Dunlop, J. S., Dutton, A. A., Elbaz, D., Fazio, G. G., Filippenko, A. V., Finkelstein, S. L., Fontana, A.,

Gardner, J. P., Garnavich, P. M., Gawiser, E., Giavalisco, M., Grazian, A., Guo, Y., Hathi, N. P., Häussler, B., Hopkins, P. F., Huang, J.-S., Huang, K.-H., Jha, S. W., Kartaltepe, J. S., Kirshner, R. P., Koo, D. C., Lai, K., Lee, K.-S., Li, W., Lotz, J. M., Lucas, R. A., Madau, P., McCarthy, P. J., McGrath, E. J., McIntosh, D. H., McLure, R. J., Mobasher, B., Moustakas, L. A., Mozena, M., Nandra, K., Newman, J. A., Niemi, S.-M., Noeske, K. G., Papovich, C. J., Pentericci, L., Pope, A., Primack, J. R., Rajan, A., Ravindranath, S., Reddy, N. A., Renzini, A., Rix, H.-W., Robaina, A. R., Rodney, S. A., Rosario, D. J., Rosati, P., Salimbeni, S., Scarlata, C., Siana, B., Simard, L., Smidt, J., Somerville, R. S., Spinrad, H., Straughn, A. N., Strolger, L.-G., Telford, O., Teplitz, H. I., Trump, J. R., van der Wel, A., Villforth, C., Wechsler, R. H., Weiner, B. J., Wiklind, T., Wild, V., Wilson, G., Wuyts, S., Yan, H.-J., and Yun, M. S. (2011). CANDELS: The Cosmic Assembly Near-infrared Deep Extragalactic Legacy Survey. , 197(2):35.

Gunn, J. E. and Gott, J. Richard, I. (1972). On the Infall of Matter Into Clusters of Galaxies and Some Effects on Their Evolution. , 176:1.

Guo, Y., Ferguson, H. C., Bell, E. F., Koo, D. C., Conselice, C. J., Giavalisco, M., Kassin, S., Lu, Y., Lucas, R., Mandelker, N., McIntosh, D. H., Primack, J. R., Ravindranath, S., Barro, G., Ceverino, D., Dekel, A., Faber, S. M., Fang, J. J., Koekemoer, A. M., Noeske, K., Rafelski, M., and Straughn, A. (2015). Clumpy Galaxies in CANDELS. I. The Definition of UV Clumps and the Fraction of Clumpy Galaxies at $0.5 < z < 3.$ , 800(1):39.

Guo, Y., Ferguson, H. C., Giavalisco, M., Barro, G., Willner, S. P., Ashby, M. L. N., Dahlen, T., Donley, J. L., Faber, S. M., Fontana, A., Galametz, A., Grazian, A., Huang, K.-H., Kocevski,

D. D., Koekemoer, A. M., Koo, D. C., McGrath, E. J., Peth, M., Salvato, M., Wuyts, S., Castellano, M., Cooray, A. R., Dickinson, M. E., Dunlop, J. S., Fazio, G. G., Gardner, J. P., Gawiser, E., Grogin, N. A., Hathi, N. P., Hsu, L.-T., Lee, K.-S., Lucas, R. A., Mobasher, B., Nandra, K., Newman, J. A., and van der Wel, A. (2013). CANDELS Multi-wavelength Catalogs: Source Detection and Photometry in the GOODS-South Field. , 207(2):24.

Guo, Y., Giavalisco, M., Ferguson, H. C., Cassata, P., and Koekemoer, A. M. (2012). Multi-wavelength View of Kiloparsec-scale Clumps in Star-forming Galaxies at z $\sim$ 2. , 757(2):120.

Guo, Y., Koo, D. C., Lu, Y., Forbes, J. C., Rafelski, M., Trump, J. R., Amorín, R., Barro, G., Davé, R., Faber, S. M., Hathi, N. P., Yesuf, H., Cooper, M. C., Dekel, A., Guhathakurta, P., Kirby, E. N., Koekemoer, A. M., Pérez-González, P. G., Lin, L., Newman, J. A., Primack, J. R., Rosario, D. J., Willmer, C. N. A., and Yan, R. (2016). Stellar Mass-Gas-phase Metallicity Relation at 0.5 $\leq$ z $\leq$ 0.7: A Power Law with Increasing Scatter toward the Low-mass Regime. , 822(2):103.

Guo, Y., Rafelski, M., Bell, E. F., Conselice, C. J., Dekel, A., Faber, S. M., Giavalisco, M., Koekemoer, A. M., Koo, D. C., Lu, Y., Mandelker, N., Primack, J. R., Ceverino, D., de Mello, D. F., Ferguson, H. C., Hathi, N., Kocevski, D., Lucas, R. A., Pérez-González, P. G., Ravindranath, S., Soto, E., Straughn, A., and Wang, W. (2018). Clumpy Galaxies in CANDELS. II. Physical Properties of UV-bright Clumps at 0.5 $\leq$ z $<$ 3. , 853(2):108.

Heckman, T. M., Armus, L., and Miley, G. K. (1990). On the Nature and Implications of Starburst-driven Galactic Superwinds. , 74:833.

Hemmati, S., Miller, S. H., Mobasher, B., Nayyeri, H., Ferguson, H. C., Guo, Y., Koekemoer, A. M., Koo, D. C., and Papovich, C. (2014). Kiloparsec-scale Properties of Emission-line Galaxies. , 797(2):108.

Hemmati, S., Mobasher, B., Darvish, B., Nayyeri, H., Sobral, D., and Miller, S. (2015). Nebular and Stellar Dust Extinction Across the Disk of Emission-line Galaxies on Kiloparsec Scales. , 814(1):46.

Hine, N. K., Geach, J. E., Alexander, D. M., Lehmer, B. D., Chapman, S. C., and Matsuda, Y. (2016). An enhanced merger fraction within the galaxy population of the SSA22 protocluster at z = 3.1. , 455(3):2363–2370.

Hinojosa-Goñi, R., Muñoz-Tuñón, C., and Méndez-Abreu, J. (2016). Starburst galaxies in the COSMOS field: clumpy star-formation at redshift $0 < z < 0.5$. , 592:A122.

Hopkins, P. F., Kereš, D., and Murray, N. (2013). Accretion does not drive the turbulence in galactic discs. , 432(4):2639–2646.

Hopkins, P. F., Kereš, D., Murray, N., Quataert, E., and Hernquist, L. (2012). Stellar feedback and bulge formation in clumpy discs. , 427(2):968–978.

Horne, K. (1986). An optimal extraction algorithm for CCD spectroscopy. , 98:609–617.

Horstman, K., Shapley, A. E., Sanders, R. L., Mobasher, B., Reddy, N. A., Kriek, M., Coil, A. L.,

Siana, B., Shivaei, I., Freeman, W. R., Azadi, M., Price, S. H., Leung, G. C. K., Fetherolf, T., de Groot, L., Zick, T., Fornasini, F. M., and Barro, G. (2020). The MOSDEF Survey: Differences in SFR and Metallicity for Morphologically-Selected Mergers at z $\sim$ 2. *arXiv e-prints*, page arXiv:2008.04327.

Huertas-Company, M., Guo, Y., Ginzburg, O., Lee, C. T., Mandelker, N., Metter, M., Primack, J. R., Dekel, A., Ceverino, D., Faber, S. M., Koo, D. C., Koekemoer, A., Snyder, G., Giavalisco, M., and Zhang, H. (2020). Stellar masses of giant clumps in CANDELS and simulated galaxies using machine learning. , 499(1):814–835.

Iani, E., Zanella, A., Vernet, J., Richard, J., Gronke, M., Harrison, C. M., Arrigoni-Battaia, F., Rodighiero, G., Burkert, A., Behrendt, M., Chen, C.-C., Emsellem, E., Fensch, J., Hibon, P., Hilker, M., Le Floc'h, E., Mainieri, V., Swinbank, A. M., Valentino, F., Vanzella, E., and Zwaan, M. A. (2021). Stellar feedback in a clumpy galaxy at z 3.4. , 507(3):3830–3848.

Ilbert, O., Arnouts, S., McCracken, H. J., Bolzonella, M., Bertin, E., Le Fèvre, O., Mellier, Y., Zamorani, G., Pellò, R., Iovino, A., Tresse, L., Le Brun, V., Bottini, D., Garilli, B., Maccagni, D., Picat, J. P., Scaramella, R., Scodeggio, M., Vettolani, G., Zanichelli, A., Adami, C., Bardelli, S., Cappi, A., Charlot, S., Ciliegi, P., Contini, T., Cucciati, O., Foucaud, S., Franzetti, P., Gavignaud, I., Guzzo, L., Marano, B., Marinoni, C., Mazure, A., Meneux, B., Merighi, R., Paltani, S., Pollo, A., Pozzetti, L., Radovich, M., Zucca, E., Bondi, M., Bongiorno, A., Busarello, G., de La Torre, S., Gregorini, L., Lamareille, F., Mathez, G., Merluzzi, P., Ripepi, V., Rizzo, D., and Vergani, D. (2006). Accurate photometric redshifts for the CFHT legacy survey calibrated using the

VIMOS VLT deep survey. , 457(3):841–856.

Ilbert, O., Capak, P., Salvato, M., Aussel, H., McCracken, H. J., Sanders, D. B., Scoville, N., Kartaltepe, J., Arnouts, S., Le Floc'h, E., Mobasher, B., Taniguchi, Y., Lamareille, F., Leauthaud, A., Sasaki, S., Thompson, D., Zamojski, M., Zamorani, G., Bardelli, S., Bolzonella, M., Bongiorno, A., Brusa, M., Caputi, K. I., Carollo, C. M., Contini, T., Cook, R., Coppa, G., Cucciati, O., de la Torre, S., de Ravel, L., Franzetti, P., Garilli, B., Hasinger, G., Iovino, A., Kampczyk, P., Kneib, J. P., Knobel, C., Kovac, K., Le Borgne, J. F., Le Brun, V., Le Fèvre, O., Lilly, S., Looper, D., Maier, C., Mainieri, V., Mellier, Y., Mignoli, M., Murayama, T., Pellò, R., Peng, Y., Pérez-Montero, E., Renzini, A., Ricciardelli, E., Schiminovich, D., Scodeggio, M., Shioya, Y., Silverman, J., Surace, J., Tanaka, M., Tasca, L., Tresse, L., Vergani, D., and Zucca, E. (2009). Cosmos Photometric Redshifts with 30-Bands for 2-deg$^2$. , 690(2):1236–1249.

Illingworth, G. D., Magee, D., Oesch, P. A., Bouwens, R. J., Labbé, I., Stiavelli, M., van Dokkum, P. G., Franx, M., Trenti, M., Carollo, C. M., and Gonzalez, V. (2013). The HST eXtreme Deep Field (XDF): Combining All ACS and WFC3/IR Data on the HUDF Region into the Deepest Field Ever. , 209(1):6.

Immeli, A., Samland, M., Gerhard, O., and Westera, P. (2004a). Gas physics, disk fragmentation, and bulge formation in young galaxies. , 413:547–561.

Immeli, A., Samland, M., Westera, P., and Gerhard, O. (2004b). Subgalactic Clumps at High Redshift: A Fragmentation Origin? , 611(1):20–25.

Inoue, S., Dekel, A., Mandelker, N., Ceverino, D., Bournaud, F., and Primack, J. (2016). Non-linear violent disc instability with high Toomre's Q in high-redshift clumpy disc galaxies. , 456(2):2052–2069.

Ishigaki, M., Kawamata, R., Ouchi, M., Oguri, M., Shimasaku, K., and Ono, Y. (2015). Hubble Frontier Fields First Complete Cluster Data: Faint Galaxies at z $\sim$ 5-10 for UV Luminosity Functions and Cosmic Reionization. , 799(1):12.

Ji, Z., Giavalisco, M., Williams, C. C., Faber, S. M., Ferguson, H. C., Guo, Y., Liu, T., and Lee, B. (2018). Evidence of Environmental Quenching at Redshift z $\approx$ 2. , 862(2):135.

Jimmy, Tran, K.-V., Saintonge, A., Accurso, G., Brough, S., and Oliva-Altamirano, P. (2015). The Gas Phase Mass Metallicity Relation for Dwarf Galaxies: Dependence on Star Formation Rate and H I Gas Mass. , 812(2):98.

Johnson, T. L., Rigby, J. R., Sharon, K., Gladders, M. D., Florian, M., Bayliss, M. B., Wuyts, E., Whitaker, K. E., Livermore, R., and Murray, K. T. (2017). Star Formation at z = 2.481 in the Lensed Galaxy SDSS J1110+6459: Star Formation Down to 30 pc Scales. , 843(2):L21.

Jones, T. A., Swinbank, A. M., Ellis, R. S., Richard, J., and Stark, D. P. (2010). Resolved spectroscopy of gravitationally lensed galaxies: recovering coherent velocity fields in subluminous z $\sim$ 2-3 galaxies. , 404(3):1247–1262.

Juneau, S., Bournaud, F., Charlot, S., Daddi, E., Elbaz, D., Trump, J. R., Brinchmann, J., Dick-

inson, M., Duc, P.-A., Gobat, R., Jean-Baptiste, I., Le Floc'h, É., Lehnert, M. D., Pacifici, C., Pannella, M., and Schreiber, C. (2014). Active Galactic Nuclei Emission Line Diagnostics and the Mass-Metallicity Relation up to Redshift z $\sim$ 2: The Impact of Selection Effects and Evolution. , 788(1):88.

Kacprzak, G. G., Yuan, T., Nanayakkara, T., Kobayashi, C., Tran, K.-V. H., Kewley, L. J., Glazebrook, K., Spitler, L., Taylor, P., Cowley, M., Labbe, I., Straatman, C., and Tomczak, A. (2015). The Absence of an Environmental Dependence in the Mass-Metallicity Relation at z = 2. , 802(2):L26.

Kado-Fong, E., Geha, M., Mao, Y.-Y., de los Reyes, M. A. C., Wechsler, R. H., Asali, Y., Kallivayalil, N., Nadler, E. O., Tollerud, E. J., and Weiner, B. (2024). SAGAbg. I. A Near-unity Mass-loading Factor in Low-mass Galaxies via Their Low-redshift Evolution in Stellar Mass, Oxygen Abundance, and Star Formation Rate. , 966(1):129.

Kashino, D., Silverman, J. D., Rodighiero, G., Renzini, A., Arimoto, N., Daddi, E., Lilly, S. J., Sanders, D. B., Kartaltepe, J., Zahid, H. J., Nagao, T., Sugiyama, N., Capak, P., Carollo, C. M., Chu, J., Hasinger, G., Ilbert, O., Kajisawa, M., Kewley, L. J., Koekemoer, A. M., Kovač, K., Le Fèvre, O., Masters, D., McCracken, H. J., Onodera, M., Scoville, N., Strazzullo, V., Symeonidis, M., and Taniguchi, Y. (2013). The FMOS-COSMOS Survey of Star-forming Galaxies at z $\sim$ 1.6. I. H$\alpha$-based Star Formation Rates and Dust Extinction. , 777(1):L8.

Kauffmann, G., Heckman, T. M., Tremonti, C., Brinchmann, J., Charlot, S., White, S. D. M., Ridg-

way, S. E., Brinkmann, J., Fukugita, M., Hall, P. B., Ivezić, Ž., Richards, G. T., and Schneider, D. P. (2003). The host galaxies of active galactic nuclei. , 346(4):1055–1077.

Kauffmann, G., White, S. D. M., Heckman, T. M., Ménard, B., Brinchmann, J., Charlot, S., Tremonti, C., and Brinkmann, J. (2004). The environmental dependence of the relations between stellar mass, structure, star formation and nuclear activity in galaxies. , 353(3):713–731.

Kawinwanichakij, L., Papovich, C., Quadri, R. F., Glazebrook, K., Kacprzak, G. G., Allen, R. J., Bell, E. F., Croton, D. J., Dekel, A., Ferguson, H. C., Forrest, B., Grogin, N. A., Guo, Y., Kocevski, D. D., Koekemoer, A. M., Labbé, I., Lucas, R. A., Nanayakkara, T., Spitler, L. R., Straatman, C. M. S., Tran, K.-V. H., Tomczak, A., and van Dokkum, P. (2017). Effect of Local Environment and Stellar Mass on Galaxy Quenching and Morphology at $0.5 < z < 2.0$. , 847(2):134.

Kelson, D. D. (2003). Optimal Techniques in Two-dimensional Spectroscopy: Background Subtraction for the 21st Century. , 115(808):688–699.

Kelson, D. D. (2014). Decoding the Star-Forming Main Sequence or: How I Learned to Stop Worrying and Love the Central Limit Theorem. *arXiv e-prints*, page arXiv:1406.5191.

Kelson, D. D., Abramson, L. E., Benson, A. J., Patel, S. G., Shectman, S. A., Dressler, A., McCarthy, P. J., Mulchaey, J. S., and Williams, R. J. (2020). Gravity and the non-linear growth of structure in the Carnegie-Spitzer-IMACS Redshift Survey. , 494(2):2628–2640.

Kelson, D. D., Illingworth, G. D., van Dokkum, P. G., and Franx, M. (2000). The Evolution of Early-Type Galaxies in Distant Clusters. II. Internal Kinematics of 55 Galaxies in the z=0.33 Cluster CL 1358+62. , 531(1):159–183.

Kennicutt, Robert C., J. (1998). Star Formation in Galaxies Along the Hubble Sequence. , 36:189–232.

Kereš, D., Katz, N., Weinberg, D. H., and Davé, R. (2005). How do galaxies get their gas? , 363(1):2–28.

Kewley, L. J., Dopita, M. A., Sutherland, R. S., Heisler, C. A., and Trevena, J. (2001). Theoretical Modeling of Starburst Galaxies. , 556(1):121–140.

Kewley, L. J. and Ellison, S. L. (2008). Metallicity Calibrations and the Mass-Metallicity Relation for Star-forming Galaxies. , 681(2):1183–1204.

Kodra, D. (2019). *The Galaxy Morphology-Density Relation at High Redshift with Candels*. PhD thesis, University of Pittsburgh.

Kodra, D., Andrews, B. H., Newman, J. A., Finkelstein, S. L., Fontana, A., Hathi, N., Salvato, M., Wiklind, T., Wuyts, S., Broussard, A., Chartab, N., Conselice, C., Cooper, M. C., Dekel, A., Dickinson, M., Ferguson, H., Gawiser, E., Grogin, N. A., Iyer, K., Kartaltepe, J., Kassin, S., Koekemoer, A. M., Koo, D. C., Lucas, R. A., Mantha, K. B., McIntosh, D. H., Mobasher, B., Pacifici, C., Pérez-González, P. G., and Santini, P. (2022). Optimized Photometric Redshifts

for the Cosmic Assembly Near-Infrared Deep Extragalactic Legacy Survey (CANDELS). *arXiv e-prints*, page arXiv:2210.01140.

Koekemoer, A. M., Ellis, R. S., McLure, R. J., Dunlop, J. S., Robertson, B. E., Ono, Y., Schenker, M. A., Ouchi, M., Bowler, R. A. A., Rogers, A. B., Curtis-Lake, E., Schneider, E., Charlot, S., Stark, D. P., Furlanetto, S. R., Cirasuolo, M., Wild, V., and Targett, T. (2013). The 2012 Hubble Ultra Deep Field (UDF12): Observational Overview. , 209(1):3.

Koekemoer, A. M., Faber, S. M., Ferguson, H. C., Grogin, N. A., Kocevski, D. D., Koo, D. C., Lai, K., Lotz, J. M., Lucas, R. A., McGrath, E. J., Ogaz, S., Rajan, A., Riess, A. G., Rodney, S. A., Strolger, L., Casertano, S., Castellano, M., Dahlen, T., Dickinson, M., Dolch, T., Fontana, A., Giavalisco, M., Grazian, A., Guo, Y., Hathi, N. P., Huang, K.-H., van der Wel, A., Yan, H.-J., Acquaviva, V., Alexander, D. M., Almaini, O., Ashby, M. L. N., Barden, M., Bell, E. F., Bournaud, F., Brown, T. M., Caputi, K. I., Cassata, P., Challis, P. J., Chary, R.-R., Cheung, E., Cirasuolo, M., Conselice, C. J., Roshan Cooray, A., Croton, D. J., Daddi, E., Davé, R., de Mello, D. F., de Ravel, L., Dekel, A., Donley, J. L., Dunlop, J. S., Dutton, A. A., Elbaz, D., Fazio, G. G., Filippenko, A. V., Finkelstein, S. L., Frazer, C., Gardner, J. P., Garnavich, P. M., Gawiser, E., Gruetzbauch, R., Hartley, W. G., Häussler, B., Herrington, J., Hopkins, P. F., Huang, J.-S., Jha, S. W., Johnson, A., Kartaltepe, J. S., Khostovan, A. A., Kirshner, R. P., Lani, C., Lee, K.-S., Li, W., Madau, P., McCarthy, P. J., McIntosh, D. H., McLure, R. J., McPartland, C., Mobasher, B., Moreira, H., Mortlock, A., Moustakas, L. A., Mozena, M., Nandra, K., Newman, J. A., Nielsen, J. L., Niemi, S., Noeske, K. G., Papovich, C. J., Pentericci, L., Pope, A., Primack, J. R., Ravindranath, S., Reddy, N. A., Renzini, A., Rix, H.-W., Robaina, A. R., Rosario, D. J., Rosati, P., Salimbeni,

S., Scarlata, C., Siana, B., Simard, L., Smidt, J., Snyder, D., Somerville, R. S., Spinrad, H., Straughn, A. N., Telford, O., Teplitz, H. I., Trump, J. R., Vargas, C., Villforth, C., Wagner, C. R., Wandro, P., Wechsler, R. H., Weiner, B. J., Wiklind, T., Wild, V., Wilson, G., Wuyts, S., and Yun, M. S. (2011). CANDELS: The Cosmic Assembly Near-infrared Deep Extragalactic Legacy Survey—The Hubble Space Telescope Observations, Imaging Data Products, and Mosaics. , 197(2):36.

Koyama, Y., Smail, I., Kurk, J., Geach, J. E., Sobral, D., Kodama, T., Nakata, F., Swinbank, A. M., Best, P. N., Hayashi, M., and Tadaki, K.-i. (2013). On the evolution and environmental dependence of the star formation rate versus stellar mass relation since z $\sim$ 2. , 434(1):423–436.

Kreckel, K., Groves, B., Schinnerer, E., Johnson, B. D., Aniano, G., Calzetti, D., Croxall, K. V., Draine, B. T., Gordon, K. D., Crocker, A. F., Dale, D. A., Hunt, L. K., Kennicutt, R. C., Meidt, S. E., Smith, J. D. T., and Tabatabaei, F. S. (2013). Mapping Dust through Emission and Absorption in Nearby Galaxies. , 771(1):62.

Kriek, M., Shapley, A. E., Reddy, N. A., Siana, B., Coil, A. L., Mobasher, B., Freeman, W. R., de Groot, L., Price, S. H., Sanders, R., Shivaei, I., Brammer, G. B., Momcheva, I. G., Skelton, R. E., van Dokkum, P. G., Whitaker, K. E., Aird, J., Azadi, M., Kassis, M., Bullock, J. S., Conroy, C., Davé, R., Kereš, D., and Krumholz, M. (2015). The MOSFIRE Deep Evolution Field (MOSDEF) Survey: Rest-frame Optical Spectroscopy for $\sim$1500 H-selected Galaxies at 1.37 $<$ z $<$ 3.8. , 218(2):15.

Kriek, M., van Dokkum, P. G., Labbé, I., Franx, M., Illingworth, G. D., Marchesini, D., and Quadri, R. F. (2009). An Ultra-Deep Near-Infrared Spectrum of a Compact Quiescent Galaxy at z = 2.2. , 700(1):221–231.

Kroupa, P. (2001). On the variation of the initial mass function. , 322(2):231–246.

Kulas, K. R., McLean, I. S., Shapley, A. E., Steidel, C. C., Konidaris, N. P., Matthews, K., Mace, G. N., Rudie, G. C., Trainor, R. F., and Reddy, N. A. (2013). The Mass-Metallicity Relation of a z $\sim$ 2 Protocluster with MOSFIRE. , 774(2):130.

Kurk, J., Cimatti, A., Zamorani, G., Halliday, C., Mignoli, M., Pozzetti, L., Daddi, E., Rosati, P., Dickinson, M., Bolzonella, M., Cassata, P., Renzini, A., Franceschini, A., Rodighiero, G., and Berta, S. (2009). GMASS ultradeep spectroscopy of galaxies at z $\sim$ 2 . V. Witnessing the assembly at z = 1.6 of a galaxy cluster. , 504(2):331–346.

Laigle, C., McCracken, H. J., Ilbert, O., Hsieh, B. C., Davidzon, I., Capak, P., Hasinger, G., Silverman, J. D., Pichon, C., Coupon, J., Aussel, H., Le Borgne, D., Caputi, K., Cassata, P., Chang, Y. Y., Civano, F., Dunlop, J., Fynbo, J., Kartaltepe, J. S., Koekemoer, A., Le Fèvre, O., Le Floc'h, E., Leauthaud, A., Lilly, S., Lin, L., Marchesi, S., Milvang-Jensen, B., Salvato, M., Sanders, D. B., Scoville, N., Smolcic, V., Stockmann, M., Taniguchi, Y., Tasca, L., Toft, S., Vaccari, M., and Zabl, J. (2016). The COSMOS2015 Catalog: Exploring the 1 $<$ z $<$ 6 Universe with Half a Million Galaxies. , 224(2):24.

Lara-López, M. A., Cepa, J., Bongiovanni, A., Pérez García, A. M., Ederoclite, A., Castañeda, H.,

Fernández Lorenzo, M., Pović, M., and Sánchez-Portal, M. (2010a). A fundamental plane for field star-forming galaxies. , 521:L53.

Lara-López, M. A., Cepa, J., Bongiovanni, A., Pérez García, A. M., Ederoclite, A., Castañeda, H., Fernández Lorenzo, M., Pović, M., and Sánchez-Portal, M. (2010b). A fundamental plane for field star-forming galaxies. , 521:L53.

Lee, H., Skillman, E. D., and Venn, K. A. (2006). The Spatial Homogeneity of Nebular and Stellar Oxygen Abundances in the Local Group Dwarf Irregular Galaxy NGC 6822. , 642(2):813–833.

Lemaux, B. C., Cucciati, O., Le Fèvre, O., Zamorani, G., Lubin, L. M., Hathi, N., Ilbert, O., Pelliccia, D., Amorín, R., Bardelli, S., Cassata, P., Gal, R. R., Garilli, B., Guaita, L., Giavalisco, M., Hung, D., Koekemoer, A., Maccagni, D., Pentericci, L., Ribeiro, B., Schaerer, D., Shah, E., Shen, L., Staab, P., Talia, M., Thomas, R., Tomczak, A. R., Tresse, L., Vanzella, E., Vergani, D., and Zucca, E. (2022). The VIMOS Ultra Deep Survey: The reversal of the star-formation rate − density relation at $2 < z < 5$. , 662:A33.

Lequeux, J., Peimbert, M., Rayo, J. F., Serrano, A., and Torres-Peimbert, S. (1979). Chemical Composition and Evolution of Irregular and Blue Compact Galaxies. , 80:155.

Li, M., Cai, Z., Bian, F., Lin, X., Li, Z., Wu, Y., Sun, F., Zhang, S., Golden-Marx, E., Sun, Z., Zou, S., Fan, X., Egami, E., Charlot, S., Bruzual, G., and Chevallard, J. (2023). The Mass-Metallicity Relation of Dwarf Galaxies at Cosmic Noon from JWST Observations. , 955(1):L18.

Lilly, S. J., Carollo, C. M., Pipino, A., Renzini, A., and Peng, Y. (2013). Gas Regulation of Galaxies: The Evolution of the Cosmic Specific Star Formation Rate, the Metallicity-Mass-Star-formation Rate Relation, and the Stellar Content of Halos. , 772(2):119.

Lin, X., Cai, Z., Zou, S., Li, Z., Chen, Z., Bian, F., Sun, F., Shu, Y., Wu, Y., Li, M., Li, J., Fan, X., Prochaska, J. X., Schaerer, D., Charlot, S., Espada, D., Dessauges-Zavadsky, M., Egami, E., Stark, D., Knudsen, K. K., Bruzual, G., and Chevallard, J. (2023). Metal-enriched Neutral Gas Reservoir around a Strongly Lensed Low-mass Galaxy at z = 4 Identified by JWST/NIRISS and VLT/MUSE. , 944(2):L59.

Livermore, R. C., Jones, T., Richard, J., Bower, R. G., Ellis, R. S., Swinbank, A. M., Rigby, J. R., Smail, I., Arribas, S., Rodriguez Zaurin, J., Colina, L., Ebeling, H., and Crain, R. A. (2012). Hubble Space Telescope H$\alpha$ imaging of star-forming galaxies at z = 1-1.5: evolution in the size and luminosity of giant H II regions. , 427(1):688–702.

Livermore, R. C., Jones, T. A., Richard, J., Bower, R. G., Swinbank, A. M., Yuan, T. T., Edge, A. C., Ellis, R. S., Kewley, L. J., Smail, I., Coppin, K. E. K., and Ebeling, H. (2015). Resolved spectroscopy of gravitationally lensed galaxies: global dynamics and star-forming clumps on $\sim$100 pc scales at $1 < z < 4$. , 450(2):1812–1835.

Mac Low, M.-M. and Ferrara, A. (1999). Starburst-driven Mass Loss from Dwarf Galaxies: Efficiency and Metal Ejection. , 513(1):142–155.

Madau, P. and Dickinson, M. (2014). Cosmic Star-Formation History. , 52:415–486.

Mager, V. A., Conselice, C. J., Seibert, M., Gusbar, C., Katona, A. P., Villari, J. M., Madore, B. F., and Windhorst, R. A. (2018). Galaxy Structure in the Ultraviolet: The Dependence of Morphological Parameters on Rest-frame Wavelength. , 864(2):123.

Maiolino, R. and Mannucci, F. (2019). De re metallica: the cosmic chemical evolution of galaxies. , 27(1):3.

Mandelker, N., Dekel, A., Ceverino, D., DeGraf, C., Guo, Y., and Primack, J. (2017). Giant clumps in simulated high- z Galaxies: properties, evolution and dependence on feedback. , 464(1):635–665.

Mandelker, N., Dekel, A., Ceverino, D., Tweed, D., Moody, C. E., and Primack, J. (2014). The population of giant clumps in simulated high-z galaxies: in situ and ex situ migration and survival. , 443(4):3675–3702.

Mannucci, F., Cresci, G., Maiolino, R., Marconi, A., and Gnerucci, A. (2010). A fundamental relation between mass, star formation rate and metallicity in local and high-redshift galaxies. , 408(4):2115–2127.

Mannucci, F., Cresci, G., Maiolino, R., Marconi, A., Pastorini, G., Pozzetti, L., Gnerucci, A., Risaliti, G., Schneider, R., Lehnert, M., and Salvati, M. (2009). LSD: Lyman-break galaxies Stellar populations and Dynamics - I. Mass, metallicity and gas at z $\sim$ 3.1. , 398(4):1915–1931.

Martin, C. L., Shapley, A. E., Coil, A. L., Kornei, K. A., Bundy, K., Weiner, B. J., Noeske, K. G., and Schiminovich, D. (2012). Demographics and Physical Properties of Gas Outflows/Inflows at $0.4 < z < 1.4$. , 760(2):127.

McLean, I. S., Steidel, C. C., Epps, H. W., Konidaris, N., Matthews, K. Y., Adkins, S., Aliado, T., Brims, G., Canfield, J. M., Cromer, J. L., Fucik, J., Kulas, K., Mace, G., Magnone, K., Rodriguez, H., Rudie, G., Trainor, R., Wang, E., Weber, B., and Weiss, J. (2012). MOSFIRE, the multi-object spectrometer for infra-red exploration at the Keck Observatory. In *Ground-based and Airborne Instrumentation for Astronomy IV*, volume 8446 of *Society of Photo-Optical Instrumentation Engineers (SPIE) Conference Series*, page 84460J.

Mehta, V., Scarlata, C., Capak, P., Davidzon, I., Faisst, A., Hsieh, B. C., Ilbert, O., Jarvis, M., Laigle, C., Phillips, J., Silverman, J., Strauss, M. A., Tanaka, M., Bowler, R., Coupon, J., Foucaud, S., Hemmati, S., Masters, D., McCracken, H. J., Mobasher, B., Ouchi, M., Shibuya, T., and Wang, W.-H. (2018). SPLASH-SXDF Multi-wavelength Photometric Catalog. , 235(2):36.

Mehta, V., Scarlata, C., Fortson, L., Dickinson, H., Adams, D., Chevallard, J., Charlot, S., Beck, M., Kruk, S., and Simmons, B. (2021). Investigating Clumpy Galaxies in the Sloan Digital Sky Survey Stripe 82 Using the Galaxy Zoo. , 912(1):49.

Messa, M., Adamo, A., Östlin, G., Melinder, J., Hayes, M., Bridge, J. S., and Cannon, J. (2019). Star-forming clumps in the Lyman Alpha Reference Sample of galaxies - I. Photometric analysis and clumpiness. , 487(3):4238–4260.

Messa, M., Dessauges-Zavadsky, M., Richard, J., Adamo, A., Nagy, D., Combes, F., Mayer, L., and Ebeling, H. (2022). Multiply lensed star forming clumps in the A521-sys1 galaxy at redshift 1. , 516(2):2420–2443.

Meštrić, U., Vanzella, E., Zanella, A., Castellano, M., Calura, F., Rosati, P., Bergamini, P., Mercurio, A., Meneghetti, M., Grillo, C., Caminha, G. B., Nonino, M., Merlin, E., Cupani, G., and Sani, E. (2022). Exploring the physical properties of lensed star-forming clumps at $2 \lesssim z \lesssim 6$. , 516(3):3532–3555.

Mieda, E., Wright, S. A., Larkin, J. E., Armus, L., Juneau, S., Salim, S., and Murray, N. (2016). IROCKS: Spatially Resolved Kinematics of $z \sim 1$ Star-forming Galaxies. , 831(1):78.

Moody, C. E., Guo, Y., Mandelker, N., Ceverino, D., Mozena, M., Koo, D. C., Dekel, A., and Primack, J. (2014). Star formation and clumps in cosmological galaxy simulations with radiation pressure feedback. , 444(2):1389–1399.

Moore, B., Katz, N., Lake, G., Dressler, A., and Oemler, A. (1996). Galaxy harassment and the evolution of clusters of galaxies. , 379(6566):613–616.

Mulchaey, J. S. and Zabludoff, A. I. (1998). The Properties of Poor Groups of Galaxies. II. X-Ray and Optical Comparisons. , 496(1):73–92.

Murata, K. L., Kajisawa, M., Taniguchi, Y., Kobayashi, M. A. R., Shioya, Y., Capak, P., Ilbert, O., Koekemoer, A. M., Salvato, M., and Scoville, N. Z. (2014). Evolution of the Fraction of

Clumpy Galaxies at $0.2 < z < 1.0$ in the COSMOS Field. , 786(1):15.

Murray, N., Quataert, E., and Thompson, T. A. (2010). The Disruption of Giant Molecular Clouds by Radiation Pressure & the Efficiency of Star Formation in Galaxies. , 709(1):191–209.

Muzzin, A., Marchesini, D., Stefanon, M., Franx, M., McCracken, H. J., Milvang-Jensen, B., Dunlop, J. S., Fynbo, J. P. U., Brammer, G., Labbé, I., and van Dokkum, P. G. (2013a). The Evolution of the Stellar Mass Functions of Star-forming and Quiescent Galaxies to $z = 4$ from the COSMOS/UltraVISTA Survey. , 777(1):18.

Muzzin, A., Marchesini, D., Stefanon, M., Franx, M., McCracken, H. J., Milvang-Jensen, B., Dunlop, J. S., Fynbo, J. P. U., Brammer, G., Labbé, I., and van Dokkum, P. G. (2013b). The Evolution of the Stellar Mass Functions of Star-forming and Quiescent Galaxies to $z = 4$ from the COSMOS/UltraVISTA Survey. , 777(1):18.

Muzzin, A., Marchesini, D., Stefanon, M., Franx, M., Milvang-Jensen, B., Dunlop, J. S., Fynbo, J. P. U., Brammer, G., Labbé, I., and van Dokkum, P. (2013c). A Public $K_s$ -selected Catalog in the COSMOS/ULTRAVISTA Field: Photometry, Photometric Redshifts, and Stellar Population Parameters. , 206(1):8.

Nantais, J. B., Muzzin, A., van der Burg, R. F. J., Wilson, G., Lidman, C., Foltz, R., DeGroot, A., Noble, A., Cooper, M. C., and Demarco, R. (2017). Evidence for strong evolution in galaxy environmental quenching efficiency between $z = 1.6$ and $z = 0.9$. , 465(1):L104–L108.

Nayyeri, H., Hemmati, S., Mobasher, B., Ferguson, H. C., Cooray, A., Barro, G., Faber, S. M., Dickinson, M., Koekemoer, A. M., Peth, M., Salvato, M., Ashby, M. L. N., Darvish, B., Donley, J., Durbin, M., Finkelstein, S., Fontana, A., Grogin, N. A., Gruetzbauch, R., Huang, K., Khostovan, A. A., Kocevski, D., Kodra, D., Lee, B., Newman, J., Pacifici, C., Pforr, J., Stefanon, M., Wiklind, T., Willner, S. P., Wuyts, S., Castellano, M., Conselice, C., Dolch, T., Dunlop, J. S., Galametz, A., Hathi, N. P., Lucas, R. A., and Yan, H. (2017). CANDELS Multi-wavelength Catalogs: Source Identification and Photometry in the CANDELS COSMOS Survey Field. , 228(1):7.

Noguchi, M. (1999). Early Evolution of Disk Galaxies: Formation of Bulges in Clumpy Young Galactic Disks. , 514(1):77–95.

Noll, S., Burgarella, D., Giovannoli, E., Buat, V., Marcillac, D., and Muñoz-Mateos, J. C. (2009). Analysis of galaxy spectral energy distributions from far-UV to far-IR with CIGALE: studying a SINGS test sample. , 507(3):1793–1813.

Oesch, P. A., Bouwens, R. J., Illingworth, G. D., Franx, M., Ammons, S. M., van Dokkum, P. G., Trenti, M., and Labbé, I. (2015). First Frontier Field Constraints on the Cosmic Star Formation Rate Density at z $\sim$ 10—The Impact of Lensing Shear on Completeness of High-redshift Galaxy Samples. , 808(1):104.

Old, L. J., Balogh, M. L., van der Burg, R. F. J., Biviano, A., Yee, H. K. C., Pintos-Castro, I., Webb, K., Muzzin, A., Rudnick, G., Vulcani, B., Poggianti, B., Cooper, M., Zaritsky, D., Cerulo,

P., Wilson, G., Chan, J. C. C., Lidman, C., McGee, S., Demarco, R., Forrest, B., De Lucia, G., Gilbank, D., Kukstas, E., McCarthy, I. G., Jablonka, P., Nantais, J., Noble, A., Reeves, A. M. M., and Shipley, H. (2020). The GOGREEN survey: the environmental dependence of the star-forming galaxy main sequence at 1.0 < z < 1.5. , 493(4):5987–6000.

Osterbrock, D. E. and Ferland, G. J. (2006). *Astrophysics of gaseous nebulae and active galactic nuclei*.

Overzier, R. A. (2016). The realm of the galaxy protoclusters. A review. , 24(1):14.

Overzier, R. A., Heckman, T. M., Tremonti, C., Armus, L., Basu-Zych, A., Gonçalves, T., Rich, R. M., Martin, D. C., Ptak, A., Schiminovich, D., Ford, H. C., Madore, B., and Seibert, M. (2009). Local Lyman Break Galaxy Analogs: The Impact of Massive Star-Forming Clumps on the Interstellar Medium and the Global Structure of Young, Forming Galaxies. , 706(1):203–222.

Pacifici, C., Kassin, S. A., Weiner, B. J., Holden, B., Gardner, J. P., Faber, S. M., Ferguson, H. C., Koo, D. C., Primack, J. R., Bell, E. F., Dekel, A., Gawiser, E., Giavalisco, M., Rafelski, M., Simons, R. C., Barro, G., Croton, D. J., Davé, R., Fontana, A., Grogin, N. A., Koekemoer, A. M., Lee, S.-K., Salmon, B., Somerville, R., and Behroozi, P. (2016). The Evolution of Star Formation Histories of Quiescent Galaxies. , 832(1):79.

Patel, S. G., Holden, B. P., Kelson, D. D., Illingworth, G. D., and Franx, M. (2009a). The Dependence of Star Formation Rates on Stellar Mass and Environment at z $\sim$ 0.8. , 705(1):L67–L70.

Patel, S. G., Kelson, D. D., Abramson, L. E., Sattari, Z., and Lorenz, B. (2023). Constraints on Fluctuating Star Formation Rates for Intermediate-mass Galaxies with H$\alpha$ and UV Luminosities. , 945(2):93.

Patel, S. G., Kelson, D. D., Diao, N., Tonnesen, S., and Abramson, L. E. (2018). Testing the Breathing Mode in Intermediate-mass Galaxies and Its Predicted Star Formation Rate-size Anti-correlation. , 866(2):L21.

Patel, S. G., Kelson, D. D., Holden, B. P., Franx, M., and Illingworth, G. D. (2011). The Star-formation-rate-Density Relation at $0.6 < z < 0.9$ and the Role of Star-forming Galaxies. , 735(1):53.

Patel, S. G., Kelson, D. D., Holden, B. P., Illingworth, G. D., Franx, M., van der Wel, A., and Ford, H. (2009b). A Wide-Field Study of the z $\sim$0.8 Cluster RX J0152.7-1357: The Role of Environment in the Formation of the Red Sequence. , 694(2):1349–1363.

Peeples, M. S. and Shankar, F. (2011). Constraints on star formation driven galaxy winds from the mass-metallicity relation at z= 0. , 417(4):2962–2981.

Peng, Y.-j., Lilly, S. J., Kovač, K., Bolzonella, M., Pozzetti, L., Renzini, A., Zamorani, G., Ilbert, O., Knobel, C., Iovino, A., Maier, C., Cucciati, O., Tasca, L., Carollo, C. M., Silverman, J., Kampczyk, P., de Ravel, L., Sanders, D., Scoville, N., Contini, T., Mainieri, V., Scodeggio, M., Kneib, J.-P., Le Fèvre, O., Bardelli, S., Bongiorno, A., Caputi, K., Coppa, G., de la Torre, S., Franzetti, P., Garilli, B., Lamareille, F., Le Borgne, J.-F., Le Brun, V., Mignoli, M., Perez Montero,

E., Pello, R., Ricciardelli, E., Tanaka, M., Tresse, L., Vergani, D., Welikala, N., Zucca, E., Oesch, P., Abbas, U., Barnes, L., Bordoloi, R., Bottini, D., Cappi, A., Cassata, P., Cimatti, A., Fumana, M., Hasinger, G., Koekemoer, A., Leauthaud, A., Maccagni, D., Marinoni, C., McCracken, H., Memeo, P., Meneux, B., Nair, P., Porciani, C., Presotto, V., and Scaramella, R. (2010). Mass and Environment as Drivers of Galaxy Evolution in SDSS and zCOSMOS and the Origin of the Schechter Function. , 721:193–221.

Peng, Y.-j. and Maiolino, R. (2014). The dependence of the galaxy mass-metallicity relation on environment and the implied metallicity of the IGM. , 438(1):262–270.

Pettini, M. and Pagel, B. E. J. (2004). [OIII]/[NII] as an abundance indicator at high redshift. , 348(3):L59–L63.

Pintos-Castro, I., Yee, H. K. C., Muzzin, A., Old, L., and Wilson, G. (2019). The Evolution of the Quenching of Star Formation in Cluster Galaxies since z $\sim$ 1. , 876(1):40.

Prevot, M. L., Lequeux, J., Maurice, E., Prevot, L., and Rocca-Volmerange, B. (1984). The typical interstellar extinction in the Small Magellanic Cloud. , 132:389–392.

Puech, M. (2010). Clumpy galaxies at z $\sim$ 0.6: kinematics, stability and comparison with analogues at other redshifts. , 406(1):535–547.

Qin, J., Zheng, X. Z., Wuyts, S., Pan, Z., and Ren, J. (2019). Understanding the Discrepancy between IRX and Balmer Decrement in Tracing Galaxy Dust Attenuation. , 886(1):28.

Quadri, R., van Dokkum, P., Gawiser, E., Franx, M., Marchesini, D., Lira, P., Rudnick, G., Herrera, D., Maza, J., Kriek, M., Labbé, I., and Francke, H. (2007). Clustering of K-selected Galaxies at $2 < z < 3.5$: Evidence for a Color-Density Relation. , 654(1):138–152.

Quadri, R. F., Williams, R. J., Franx, M., and Hildebrandt, H. (2012). Tracing the Star-formation-Density Relation to z $\sim$2. , 744(2):88.

Reddy, N. A., Kriek, M., Shapley, A. E., Freeman, W. R., Siana, B., Coil, A. L., Mobasher, B., Price, S. H., Sanders, R. L., and Shivaei, I. (2015). The MOSDEF Survey: Measurements of Balmer Decrements and the Dust Attenuation Curve at Redshifts z $\sim$ 1.4-2.6. , 806(2):259.

Rigby, J. R., Johnson, T. L., Sharon, K., Whitaker, K., Gladders, M. D., Florian, M., Lotz, J., Bayliss, M., and Wuyts, E. (2017). Star Formation at $z = 2.481$ in the Lensed Galaxy SDSS J1110+6459. II. What is Missed at the Normal Resolution of the Hubble Space Telescope? , 843(2):79.

Robertson, B. E. and Bullock, J. S. (2008). High-Redshift Galaxy Kinematics: Constraints on Models of Disk Formation. , 685(1):L27.

Robertson, B. E., Ellis, R. S., Dunlop, J. S., McLure, R. J., and Stark, D. P. (2010). Early star-forming galaxies and the reionization of the Universe. , 468(7320):49–55.

Sales, L. V., Wetzel, A., and Fattahi, A. (2022). Baryonic solutions and challenges for cosmological models of dwarf galaxies. *Nature Astronomy*, 6:897–910.

Salim, S., Rich, R. M., Charlot, S., Brinchmann, J., Johnson, B. D., Schiminovich, D., Seibert, M., Mallery, R., Heckman, T. M., Forster, K., Friedman, P. G., Martin, D. C., Morrissey, P., Neff, S. G., Small, T., Wyder, T. K., Bianchi, L., Donas, J., Lee, Y.-W., Madore, B. F., Milliard, B., Szalay, A. S., Welsh, B. Y., and Yi, S. K. (2007). UV Star Formation Rates in the Local Universe. , 173(2):267–292.

Sanders, R. L., Shapley, A. E., Kriek, M., Freeman, W. R., Reddy, N. A., Siana, B., Coil, A. L., Mobasher, B., Davé, R., Shivaei, I., Azadi, M., Price, S. H., Leung, G., Fetherolf, T., de Groot, L., Zick, T., Fornasini, F. M., and Barro, G. (2018). The MOSDEF Survey: A Stellar Mass-SFR-Metallicity Relation Exists at z $\sim$ 2.3. , 858(2):99.

Sanders, R. L., Shapley, A. E., Kriek, M., Reddy, N. A., Freeman, W. R., Coil, A. L., Siana, B., Mobasher, B., Shivaei, I., Price, S. H., and de Groot, L. (2015). The MOSDEF Survey: Mass, Metallicity, and Star-formation Rate at z $\sim$ 2.3. , 799(2):138.

Sanders, R. L., Shapley, A. E., Reddy, N. A., Kriek, M., Siana, B., Coil, A. L., Mobasher, B., Shivaei, I., Freeman, W. R., Azadi, M., Price, S. H., Leung, G., Fetherolf, T., de Groot, L., Zick, T., Fornasini, F. M., and Barro, G. (2020). The MOSDEF survey: direct-method metallicities and ISM conditions at z $\sim$ 1.5-3.5. , 491(1):1427–1455.

Sattari, Z., Mobasher, B., Chartab, N., Darvish, B., Shivaei, I., Scoville, N., and Sobral, D. (2021). Evidence for Gas-phase Metal Deficiency in Massive Protocluster Galaxies at z $\sim$2.2. , 910(1):57.

Sattari, Z., Mobasher, B., Chartab, N., Kelson, D. D., Teplitz, H. I., Rafelski, M., Grogin, N. A., Koekemoer, A. M., Wang, X., Windhorst, R. A., Alavi, A., Prichard, L., Sunnquist, B., Gardner, J. P., Gawiser, E., Hathi, N. P., Hayes, M. J., Ji, Z., Mehta, V., Robertson, B. E., Scarlata, C., Yung, L. Y. A., Conselice, C. J., Dai, Y. S., Guo, Y., Lucas, R. A., Martin, A., and Ravindranath, S. (2023). Fraction of Clumpy Star-forming Galaxies at $0.5 \leq z \leq 3$ in UVCANDELS: Dependence on Stellar Mass and Environment. , 951(2):147.

Scoville, N., Aussel, H., Brusa, M., Capak, P., Carollo, C. M., Elvis, M., Giavalisco, M., Guzzo, L., Hasinger, G., Impey, C., Kneib, J. P., LeFevre, O., Lilly, S. J., Mobasher, B., Renzini, A., Rich, R. M., Sanders, D. B., Schinnerer, E., Schminovich, D., Shopbell, P., Taniguchi, Y., and Tyson, N. D. (2007). The Cosmic Evolution Survey (COSMOS): Overview. , 172(1):1–8.

Shapley, A. E., Sanders, R. L., Salim, S., Reddy, N. A., Kriek, M., Mobasher, B., Coil, A. L., Siana, B., Price, S. H., Shivaei, I., Dunlop, J. S., McLure, R. J., and Cullen, F. (2022). The MOSFIRE Deep Evolution Field Survey: Implications of the Lack of Evolution in the Dust Attenuation-Mass Relation to z 2. , 926(2):145.

Shapley, A. E., Sanders, R. L., Shao, P., Reddy, N. A., Kriek, M., Coil, A. L., Mobasher, B., Siana, B., Shivaei, I., Freeman, W. R., Azadi, M., Price, S. H., Leung, G. C. K., Fetherolf, T., de Groot, L., Zick, T., Fornasini, F. M., and Barro, G. (2019). The MOSDEF Survey: Sulfur Emission-line Ratios Provide New Insights into Evolving Interstellar Medium Conditions at High Redshift. , 881(2):L35.

Sharma, S., Richard, J., Yuan, T., Patrício, V., Kewley, L., Rigby, J. R., Gupta, A., and Leethochawalit, N. (2021). Resolving star-forming clumps in a z $\sim$ 2 lensed galaxy: a pixelated Bayesian approach. , 505(1):L1–L5.

Shibuya, T., Ouchi, M., Kubo, M., and Harikane, Y. (2016). Morphologies of $\sim$ 190,000 Galaxies at z = 0-10 Revealed with HST Legacy Data. II. Evolution of Clumpy Galaxies. , 821(2):72.

Shimakawa, R., Kodama, T., Tadaki, K.-i., Hayashi, M., Koyama, Y., and Tanaka, I. (2015). An early phase of environmental effects on galaxy properties unveiled by near-infrared spectroscopy of protocluster galaxies at z $>$ 2. , 448(1):666–680.

Shivaei, I., Darvish, B., Sattari, Z., Chartab, N., Mobasher, B., Scoville, N., and Rieke, G. (2020). Dependence of the IRX-$\beta$ Dust Attenuation Relation on Metallicity and Environment. , 903(2):L28.

Silk, J. (2003). A new prescription for protogalactic feedback and outflows: where have all the baryons gone? , 343(1):249–254.

Sobral, D., Best, P. N., Matsuda, Y., Smail, I., Geach, J. E., and Cirasuolo, M. (2012). Star formation at z=1.47 from HiZELS: an H$>\alpha$+[O II] double-blind study. , 420(3):1926–1945.

Sobral, D., Best, P. N., Smail, I., Mobasher, B., Stott, J., and Nisbet, D. (2014). The stellar mass function of star-forming galaxies and the mass-dependent SFR function since z = 2.23 from HiZELS. , 437(4):3516–3528.

Sobral, D., Smail, I., Best, P. N., Geach, J. E., Matsuda, Y., Stott, J. P., Cirasuolo, M., and Kurk, J. (2013). A large H$\alpha$ survey at z = 2.23, 1.47, 0.84 and 0.40: the 11 Gyr evolution of star-forming galaxies from HiZELS. , 428(2):1128–1146.

Sobral, D., Stroe, A., Dawson, W. A., Wittman, D., Jee, M. J., Röttgering, H., van Weeren, R. J., and Brüggen, M. (2015). $MC^2$: boosted AGN and star formation activity in CIZA J2242.8+5301, a massive post-merger cluster at z = 0.19. , 450(1):630–645.

Sok, V., Muzzin, A., Jablonka, P., Marsan, Z. C., Tan, V. Y. Y., Alcorn, L., Marchesini, D., and Stefanon, M. (2022). Finite-resolution Deconvolution of Multiwavelength Imaging of 20,000 Galaxies in the COSMOS Field: The Evolution of Clumpy Galaxies over Cosmic Time. , 924(1):7.

Somerville, R. S. and Davé, R. (2015). Physical Models of Galaxy Formation in a Cosmological Framework. , 53:51–113.

Soto, E., de Mello, D. F., Rafelski, M., Gardner, J. P., Teplitz, H. I., Koekemoer, A. M., Ravindranath, S., Grogin, N. A., Scarlata, C., Kurczynski, P., and Gawiser, E. (2017). Physical Properties of Sub-galactic Clumps at $0.5 \leq Z \leq 1.5$ in the UVUDF. , 837(1):6.

Speagle, J. S., Steinhardt, C. L., Capak, P. L., and Silverman, J. D. (2014). A Highly Consistent Framework for the Evolution of the Star-Forming "Main Sequence" from z $\sim$0-6. , 214(2):15.

Stefanon, M., Yan, H., Mobasher, B., Barro, G., Donley, J. L., Fontana, A., Hemmati, S., Koeke-

moer, A. M., Lee, B., Lee, S.-K., Nayyeri, H., Peth, M., Pforr, J., Salvato, M., Wiklind, T., Wuyts, S., Ashby, M. L. N., Castellano, M., Conselice, C. J., Cooper, M. C., Cooray, A. R., Dolch, T., Ferguson, H., Galametz, A., Giavalisco, M., Guo, Y., Willner, S. P., Dickinson, M. E., Faber, S. M., Fazio, G. G., Gardner, J. P., Gawiser, E., Grazian, A., Grogin, N. A., Kocevski, D., Koo, D. C., Lee, K.-S., Lucas, R. A., McGrath, E. J., Nandra, K., Newman, J. A., and van der Wel, A. (2017). CANDELS Multi-wavelength Catalogs: Source Identification and Photometry in the CANDELS Extended Groth Strip. , 229(2):32.

Steidel, C. C., Erb, D. K., Shapley, A. E., Pettini, M., Reddy, N., Bogosavljević, M., Rudie, G. C., and Rakic, O. (2010). The Structure and Kinematics of the Circumgalactic Medium from Far-ultraviolet Spectra of z $\sim=$ 2-3 Galaxies. , 717(1):289–322.

Steidel, C. C., Rudie, G. C., Strom, A. L., Pettini, M., Reddy, N. A., Shapley, A. E., Trainor, R. F., Erb, D. K., Turner, M. L., Konidaris, N. P., Kulas, K. R., Mace, G., Matthews, K., and McLean, I. S. (2014). Strong Nebular Line Ratios in the Spectra of z $\sim$ 2-3 Star Forming Galaxies: First Results from KBSS-MOSFIRE. , 795(2):165.

Stott, J. P., Sobral, D., Bower, R., Smail, I., Best, P. N., Matsuda, Y., Hayashi, M., Geach, J. E., and Kodama, T. (2013). A fundamental metallicity relation for galaxies at z = 0.84-1.47 from HiZELS. , 436(2):1130–1141.

Straughn, A. N., Voyer, E. N., Eufrasio, R. T., de Mello, D., Petty, S., Kassin, S., Gardner, J. P., Ravindranath, S., and Soto, E. (2015). A Multiwavelength Study of Tadpole Galaxies in the

Hubble Ultra Deep Field. , 814(2):97.

Swinbank, A. M., Smail, I., Longmore, S., Harris, A. I., Baker, A. J., De Breuck, C., Richard, J., Edge, A. C., Ivison, R. J., Blundell, R., Coppin, K. E. K., Cox, P., Gurwell, M., Hainline, L. J., Krips, M., Lundgren, A., Neri, R., Siana, B., Siringo, G., Stark, D. P., Wilner, D., and Younger, J. D. (2010). Intense star formation within resolved compact regions in a galaxy at z = 2.3. , 464(7289):733–736.

Tadaki, K.-i., Kodama, T., Tanaka, I., Hayashi, M., Koyama, Y., and Shimakawa, R. (2014). The Nature of H$\alpha$-selected Galaxies at z > 2. II. Clumpy Galaxies and Compact Star-forming Galaxies. , 780(1):77.

Taylor-Mager, V. A., Conselice, C. J., Windhorst, R. A., and Jansen, R. A. (2007). Dependence of Galaxy Structure on Rest-Frame Wavelength and Galaxy Type. , 659(1):162–187.

Tremonti, C. A., Heckman, T. M., Kauffmann, G., Brinchmann, J., Charlot, S., White, S. D. M., Seibert, M., Peng, E. W., Schlegel, D. J., Uomoto, A., Fukugita, M., and Brinkmann, J. (2004). The Origin of the Mass-Metallicity Relation: Insights from 53,000 Star-forming Galaxies in the Sloan Digital Sky Survey. , 613(2):898–913.

Tumlinson, J., Peeples, M. S., and Werk, J. K. (2017). The Circumgalactic Medium. , 55(1):389–432.

Valentino, F., Daddi, E., Strazzullo, V., Gobat, R., Onodera, M., Bournaud, F., Juneau, S., Renzini,

A., Arimoto, N., Carollo, M., and Zanella, A. (2015). Metal Deficiency in Cluster Star-Forming Galaxies At Z = 2. , 801(2):132.

Vanzella, E., Calura, F., Meneghetti, M., Castellano, M., Caminha, G. B., Mercurio, A., Cupani, G., Rosati, P., Grillo, C., Gilli, R., Mignoli, M., Fiorentino, G., Arcidiacono, C., Lombini, M., and Cortecchia, F. (2019). Massive star cluster formation under the microscope at z = 6. , 483(3):3618–3635.

Vanzella, E., Caminha, G. B., Rosati, P., Mercurio, A., Castellano, M., Meneghetti, M., Grillo, C., Sani, E., Bergamini, P., Calura, F., Caputi, K., Cristiani, S., Cupani, G., Fontana, A., Gilli, R., Grazian, A., Gronke, M., Mignoli, M., Nonino, M., Pentericci, L., Tozzi, P., Treu, T., Balestra, I., and Dijkstra, M. (2021). The MUSE Deep Lensed Field on the Hubble Frontier Field MACS J0416. Star-forming complexes at cosmological distances. , 646:A57.

Vanzella, E., Castellano, M., Bergamini, P., Meneghetti, M., Zanella, A., Calura, F., Caminha, G. B., Rosati, P., Cupani, G., Meštrić, U., Brammer, G., Tozzi, P., Mercurio, A., Grillo, C., Sani, E., Cristiani, S., Nonino, M., Merlin, E., and Pignataro, G. V. (2022). High star cluster formation efficiency in the strongly lensed Sunburst Lyman-continuum galaxy at z = 2.37. , 659:A2.

Veilleux, S. and Osterbrock, D. E. (1987). Spectral Classification of Emission-Line Galaxies. , 63:295.

Virtanen, P., Gommers, R., Oliphant, T. E., Haberland, M., Reddy, T., Cournapeau, D., Burovski,

E., Peterson, P., Weckesser, W., Bright, J., van der Walt, S. J., Brett, M., Wilson, J., Millman, K. J., Mayorov, N., Nelson, A. R. J., Jones, E., Kern, R., Larson, E., Carey, C. J., Polat, İ., Feng, Y., Moore, E. W., VanderPlas, J., Laxalde, D., Perktold, J., Cimrman, R., Henriksen, I., Quintero, E. A., Harris, C. R., Archibald, A. M., Ribeiro, A. H., Pedregosa, F., van Mulbregt, P., and SciPy 1.0 Contributors (2020). SciPy 1.0: Fundamental Algorithms for Scientific Computing in Python. *Nature Methods*, 17:261–272.

Wang, K., Testi, L., Ginsburg, A., Walmsley, C. M., Molinari, S., and Schisano, E. (2015). Large-scale filaments associated with Milky Way spiral arms. , 450(4):4043–4049.

Watson, C., Tran, K.-V., Tomczak, A., Alcorn, L., Salazar, I. V., Gupta, A., Momcheva, I., Papovich, C., van Dokkum, P., Brammer, G., Lotz, J., and Willmer, C. N. A. (2019). Galaxy Merger Fractions in Two Clusters at z $\sim$ 2 Using the Hubble Space Telescope. , 874(1):63.

Weaver, J. R., Kauffmann, O. B., Ilbert, O., McCracken, H. J., Moneti, A., Toft, S., Brammer, G., Shuntov, M., Davidzon, I., Hsieh, B. C., Laigle, C., Anastasiou, A., Jespersen, C. K., Vinther, J., Capak, P., Casey, C. M., McPartland, C. J. R., Milvang-Jensen, B., Mobasher, B., Sanders, D. B., Zalesky, L., Arnouts, S., Aussel, H., Dunlop, J. S., Faisst, A., Franx, M., Furtak, L. J., Fynbo, J. P. U., Gould, K. M. L., Greve, T. R., Gwyn, S., Kartaltepe, J. S., Kashino, D., Koekemoer, A. M., Kokorev, V., Le Fèvre, O., Lilly, S., Masters, D., Magdis, G., Mehta, V., Peng, Y., Riechers, D. A., Salvato, M., Sawicki, M., Scarlata, C., Scoville, N., Shirley, R., Silverman, J. D., Sneppen, A., Smolčić, V., Steinhardt, C., Stern, D., Tanaka, M., Taniguchi, Y., Teplitz, H. I., Vaccari, M., Wang, W. H., and Zamorani, G. (2022). COSMOS2020: A Panchromatic View of the Universe

to z∼10 from Two Complementary Catalogs. , 258(1):11.

Welch, B., Coe, D., Zitrin, A., Diego, J. M., Windhorst, R., Mandelker, N., Vanzella, E., Ravindranath, S., Zackrisson, E., Florian, M., Bradley, L., Sharon, K., Bradač, M., Rigby, J., Frye, B., and Fujimoto, S. (2023). RELICS: Small-scale Star Formation in Lensed Galaxies at z = 6-10. , 943(1):2.

Whitaker, K. E., Franx, M., Leja, J., van Dokkum, P. G., Henry, A., Skelton, R. E., Fumagalli, M., Momcheva, I. G., Brammer, G. B., Labbé, I., Nelson, E. J., and Rigby, J. R. (2014). Constraining the Low-mass Slope of the Star Formation Sequence at 0.5 < z < 2.5. , 795(2):104.

White, S. D. M. and Frenk, C. S. (1991). Galaxy Formation through Hierarchical Clustering. , 379:52.

White, S. D. M. and Rees, M. J. (1978). Core condensation in heavy halos: a two-stage theory for galaxy formation and clustering. , 183:341–358.

Wisnioski, E., Förster Schreiber, N. M., Wuyts, S., Wuyts, E., Bandara, K., Wilman, D., Genzel, R., Bender, R., Davies, R., Fossati, M., Lang, P., Mendel, J. T., Beifiori, A., Brammer, G., Chan, J., Fabricius, M., Fudamoto, Y., Kulkarni, S., Kurk, J., Lutz, D., Nelson, E. J., Momcheva, I., Rosario, D., Saglia, R., Seitz, S., Tacconi, L. J., and van Dokkum, P. G. (2015). The KMOS$^{3D}$ Survey: Design, First Results, and the Evolution of Galaxy Kinematics from 0.7 <= z <= 2.7. , 799(2):209.

Woo, J., Dekel, A., Faber, S. M., Noeske, K., Koo, D. C., Gerke, B. F., Cooper, M. C., Salim, S., Dutton, A. A., Newman, J., Weiner, B. J., Bundy, K., Willmer, C. N. A., Davis, M., and Yan, R. (2013). Dependence of galaxy quenching on halo mass and distance from its centre. , 428(4):3306–3326.

Wu, P.-F., Zahid, H. J., Hwang, H. S., and Geller, M. J. (2017). The dependence of the mass-metallicity relation on large-scale environment. , 468(2):1881–1892.

Wuyts, S., Förster Schreiber, N. M., Genzel, R., Guo, Y., Barro, G., Bell, E. F., Dekel, A., Faber, S. M., Ferguson, H. C., Giavalisco, M., Grogin, N. A., Hathi, N. P., Huang, K.-H., Kocevski, D. D., Koekemoer, A. M., Koo, D. C., Lotz, J., Lutz, D., McGrath, E., Newman, J. A., Rosario, D., Saintonge, A., Tacconi, L. J., Weiner, B. J., and van der Wel, A. (2012). Smooth(er) Stellar Mass Maps in CANDELS: Constraints on the Longevity of Clumps in High-redshift Star-forming Galaxies. , 753(2):114.

Yates, R. M., Kauffmann, G., and Guo, Q. (2012). The relation between metallicity, stellar mass and star formation in galaxies: an analysis of observational and model data. , 422(1):215–231.

Zahid, H. J., Bresolin, F., Kewley, L. J., Coil, A. L., and Davé, R. (2012). The Metallicities of Low Stellar Mass Galaxies and the Scatter in the Mass-Metallicity Relation. , 750(2):120.

Zahid, H. J., Kashino, D., Silverman, J. D., Kewley, L. J., Daddi, E., Renzini, A., Rodighiero, G., Nagao, T., Arimoto, N., Sanders, D. B., Kartaltepe, J., Lilly, S. J., Maier, C., Geller, M. J.,

Capak, P., Carollo, C. M., Chu, J., Hasinger, G., Ilbert, O., Kajisawa, M., Koekemoer, A. M., Kovacs, K., Le Fèvre, O., Masters, D., McCracken, H. J., Onodera, M., Scoville, N., Strazzullo, V., Sugiyama, N., Taniguchi, Y., and COSMOS Team (2014). The FMOS-COSMOS Survey of Star-forming Galaxies at z $\sim$ 1.6. II. The Mass-Metallicity Relation and the Dependence on Star Formation Rate and Dust Extinction. , 792(1):75.

Zanella, A., Le Floc'h, E., Harrison, C. M., Daddi, E., Bernhard, E., Gobat, R., Strazzullo, V., Valentino, F., Cibinel, A., Sánchez Almeida, J., Kohandel, M., Fensch, J., Behrendt, M., Burkert, A., Onodera, M., Bournaud, F., and Scholtz, J. (2019). A contribution of star-forming clumps and accreting satellites to the mass assembly of z $\sim$ 2 galaxies. , 489(2):2792–2818.

Zavala, J. A., Casey, C. M., Scoville, N., Champagne, J. B., Chiang, Y., Dannerbauer, H., Drew, P., Fu, H., Spilker, J., Spitler, L., Tran, K. V., Treister, E., and Toft, S. (2019). On the Gas Content, Star Formation Efficiency, and Environmental Quenching of Massive Galaxies in Protoclusters at z $\approx$ 2.02.5. , 887(2):183.

Zick, T. O., Weisz, D. R., Ribeiro, B., Kriek, M. T., Johnson, B. D., Ma, X., and Bouwens, R. (2020). Towards studying hierarchical assembly in real time: a Milky Way progenitor galaxy at z = 2.36 under the microscope. , 493(4):5653–5661.